

---

# Reduced - complexity experiment for validating Fluid-Structure Interaction in ComFLOW

---

Lampros Rizos





TECHNICAL UNIVERSITY OF DELFT

MASTER THESIS

---

# Reduced - complexity experiment for validating Fluid-Structure Interaction in ComFLOW

---

*Author:*

Lampros RIZOS

S.N.: 4422392

*Thesis committee:*

Prof.dr.ir. R.H.M. HUIJSMANS

Dr.ir. P.R. Wellens

Matin Hosseini Zahraei

Dr. R.R. Negenborn

*A thesis submitted in fulfillment of the requirements  
for the degree of Master of Science*

*in*

Offshore & Dredging Engineering  
Mechanical, Maritime and Materials Engineering

*To be defended publicly on Wednesday October 26, 2016 at 11:00 am*

*An electronic version of this thesis is available at: <http://repository.tudelft.nl/>*

October 18, 2016







TECHNICAL UNIVERSITY OF DELFT

# *Abstract*

Mechanical, Maritime and Materials Engineering  
Ship Hydromechanics and Structures

Master of Science

## **Reduced - complexity experiment for validating Fluid-Structure Interaction in ComFLOW**

by Lampros RIZOS

Human activities in marine environment are expanding to more remote locations, exposing offshore structures and commercial vessels to more adverse environmental conditions. On the other hand, market has a continuous demand for more cost efficient designs. Therefore, the need for more sophisticated computational tools arises. In these tools, the inherent flexibility of the structure is involved in the calculation of its loading and response, introducing the aspect of *fluid-structure interaction*.

The objective of the current study is to produce validation data for computational tools capable of modelling fluid-structure interaction (e.g. ComFLOW). To achieve that, an experiment is designed, conducted and its results are processed to assess their reliability.

The designed arrangement includes a cylindrical flexible plate made of PTFE, placed horizontally inside a fully transparent container partly filled with water, while being attached to the bottom of a rigid cylindrical structure. The assembly is imposed to sinusoidal vertical oscillation using an electromagnetic linear drive. Due to the small scale of the arrangement and the small weight of PTFE plate, only optical instruments are used to measure structure's response. Specifically, the response of the flexible plate is measured using two instruments: a single-point laser Doppler vibrometer, that measures the velocity at a specific point of the plate and a stereoscopic set of cameras that can measure the displacements of the plate with high spatial resolution using 3D digital image correlation method. The rigid body motion of the assembly is monitored by a laser distance measurer and the imposed force is measured using a load cell. The investigated parameters include characteristics of oscillation (amplitude and frequency), the thickness of PTFE plate and its submergence depth.

The results are analysed and additional tests, required for identifying noise components, are described. Using the results of these tests, a low-pass filter was applied to the measurements of the vibrometer. Having these measurements filtered and numerically integrated, cross-checking between the displacements coming from the vibrometer and digital image correlation is carried out. The results reveal that the effect of noise coming from the linear drive can not be eliminated at the full extent.

Once the whole process is completed, conclusions are drawn and possible actions to improve the current set-up for a next series of experiments are recommended.



## *Acknowledgements*

First of all, I would like to thank my supervisor Professor Rene Huijsmans for trusting me with this challenging project. I would, also, like to express my sincere gratitude to Dr.ir. Peter Wellens for his guidance and continuous support. Moreover, I would like to thank Martin Hosseini Zahraei and Dr.ir. Ido Akkerman for their insightful comments offered during my MSc thesis.

Besides my advisors, I would like to thank the staff working on the Towing Tank laboratory of TU Delft and especially Mr. Peter Poot and Dr.ing. C.H. Thill who facilitated the experimental part of this study. Special thanks need to be dispensed to Jennifer Rodrigues Monteiro for her selfless contribution to the post-processing of videos for water elevation measurements.

With respect to the facilities used during the experimental phase, I would like to thank the people who borrowed me equipment initially purposed for their own studies. Those are Dr.ir. Henk den Besten who let me use his stereoscopic set of cameras for digital image correlation, Assistant Prof. Farbod Alijani and Rob Luttjeboer who trusted me with the single-point laser Doppler vibrometer and Dr.ir. Ton Riemslag for letting me use facilities of Material Science and Engineering Dept. for material testing.

Finally, I would like to thank my family, Dimitris, Spyridoula and Magda for their immense support during my post-graduate studies in TU Delft.



# Contents

<b>Abstract</b>	<b>iii</b>
<b>Acknowledgements</b>	<b>v</b>
<b>1 Introduction</b>	<b>1</b>
1.1 General introduction . . . . .	1
1.2 FSI in marine applications - Trends . . . . .	1
<b>2 Problem Statement</b>	<b>3</b>
2.1 Objective . . . . .	3
2.2 Designing considerations . . . . .	3
2.3 Required measurements . . . . .	4
<b>3 Literature Review</b>	<b>5</b>
3.1 Introduction . . . . .	5
3.2 Numerical methods for FSI problems . . . . .	5
3.2.1 The monolithic approach . . . . .	5
3.2.2 The partitioned approach . . . . .	6
3.2.3 Monolithic vs Partitioned methods . . . . .	9
3.2.4 Conforming and non-conforming mesh methods . . . . .	9
3.3 Experimental methods for FSI problems . . . . .	9
3.3.1 Vibrations of fluid-coupled plates . . . . .	10
3.3.2 Vibrations of submerged plates . . . . .	11
3.4 FSI in marine and offshore structures - Hydroelasticity . . . . .	14
3.4.1 Slamming . . . . .	14
3.4.2 Green Water . . . . .	17
3.4.3 Ringing . . . . .	17
<b>4 Methodology</b>	<b>19</b>
4.1 Introduction . . . . .	19
4.2 Objectives of the experiments . . . . .	19
4.3 Investigation on the experimental set-up . . . . .	19
4.3.1 1st approach: excitation through a moving object . . . . .	20
4.3.2 2nd approach: base excitation of the flexible plate . . . . .	26
4.4 Detailed design of the experimental set-up . . . . .	28
4.4.1 Measuring instruments . . . . .	28
4.4.2 Fabricated structures . . . . .	37
4.4.3 Additional equipment . . . . .	40
4.5 Experiments plan . . . . .	42
4.6 Summary . . . . .	43

<b>5</b>	<b>Preparation of the experimental arrangement</b>	<b>45</b>
5.1	Introduction . . . . .	45
5.2	Set-up fabrication . . . . .	45
5.2.1	Support structure assembly . . . . .	45
5.2.2	Alignment . . . . .	45
5.2.3	Positioning the LDV head . . . . .	46
5.2.4	Plunger preparation for image correlation . . . . .	47
5.2.5	Configuring DIC set-up . . . . .	48
5.3	Setting up the control instruments . . . . .	50
5.3.1	Data acquisition, triggering and synchronization . . . . .	50
5.3.2	Filtering and amplification . . . . .	51
5.3.3	Oscillation enforcement . . . . .	51
5.4	Calibration . . . . .	52
5.4.1	DIC cameras . . . . .	52
5.4.2	Force transducer . . . . .	55
5.4.3	Triangulation laser displacement measurer . . . . .	56
5.4.4	Laser Doppler vibrometer . . . . .	56
5.5	Setting up a video camera for water elevation measurements . . . . .	57
5.6	Summary . . . . .	58
<b>6</b>	<b>Execution of experiments - Results</b>	<b>61</b>
6.1	Introduction . . . . .	61
6.2	Cases investigated . . . . .	61
6.3	Digital Image Correlation . . . . .	63
6.3.1	Evaluation . . . . .	64
6.3.2	Results . . . . .	66
6.4	Laser Doppler Vibrometer results . . . . .	70
6.4.1	Noise identification . . . . .	72
6.4.2	Filtering . . . . .	77
6.4.3	Cross-checking between DIC and LDV measurements . . . . .	78
6.5	Water elevation measurements . . . . .	80
6.6	Summary . . . . .	83
<b>7</b>	<b>Conclusions &amp; Recommendations</b>	<b>85</b>
7.1	Conclusions . . . . .	85
7.2	Recommendations for future research . . . . .	86
	<b>Bibliography</b>	<b>89</b>
	<b>A Pre-estimation of required oscillating force</b>	<b>91</b>
	<b>B Definition of material properties</b>	<b>95</b>
	<b>C Calculation of dry natural frequencies</b>	<b>97</b>
	<b>D Detailed designs of fabricated structures</b>	<b>99</b>

# List of Figures

3.1	Schematic presentation of the monolithic approach . . . . .	6
3.2	Schematic presentation of the partitioned approach. . . . .	6
3.3	Schematic presentation of weakly coupled systems. . . . .	7
3.4	Schematic presentation of strongly coupled systems. . . . .	8
3.5	Schematic presentation of conforming and non-conforming mesh methods (Gene H., 2012) . . . . .	10
4.1	Preliminary sketch of the 1st approach . . . . .	21
4.2	Illustration of fluid velocity in a fully rigid water tank, partly filled with water with a periodically moving object represented by moving boundaries, using <i>foam-extend 3.1</i> (Rizos, 2016) . . . . .	22
4.3	Qualitative graph of dynamic amplification factor for a multi-degrees of freedom system . . . . .	23
4.4	The height of the water column $h_f$ refers to the empty tank . . . . .	24
4.5	Preliminary sketch of the 2nd approach . . . . .	27
4.6	3D digital image correlation configuration . . . . .	29
4.7	Reference and deformed facet . . . . .	29
4.8	DIC cameras FOV width versus working distance . . . . .	30
4.9	Schematic presentation of a heterodyne interferometer's configuration (reproduction from PolytecGmbH, 2003) . . . . .	32
4.10	Laser spot size vs. stand-off distance for OFV-505 with mid-range lens . . . . .	33
4.11	Schematic presentation of optical triangulation operating principle . . . . .	35
4.12	Schematic presentation of Wheatstone bridge . . . . .	37
4.13	Graph with the pre-estimated range of forces applied to the plunger for $A_{osc} = 0.5, 1 \text{ cm}$ and $f_{osc} \in [0, 6]$ , case: "Deep" . . . . .	38
4.14	Cross section of the water container . . . . .	38
4.15	Clamped boundaries of the PTFE bottom plate in enlarged view . . . . .	39
4.16	3D drawing of the plunger assembly with parts list . . . . .	39
4.17	3D drawing of the wooden base . . . . .	40
4.18	3D drawing of the support structure . . . . .	40
4.19	Force vs Position graph of LinMot P01-37x120/80x160 motor . . . . .	41
4.20	Position vs Time graph of LinMot P01-37x120/80x160 motor . . . . .	41
4.21	Experimental matrix for each case of plate's thickness . . . . .	42
4.22	Schematic presentation of the experimental arrangement . . . . .	44
5.1	Aluminium columns before and after assembling . . . . .	46
5.2	Mode shapes of circular plates . . . . .	47
5.3	Application of black speckle pattern on the flexible PTFE plate . . . . .	48
5.4	View of plunger's bottom from the position of DIC cameras . . . . .	48
5.5	Two LED lamps placed around the water container for targeted illumination to the plunger . . . . .	49
5.6	Control panel of signal generator used for image acquisition triggering . . . . .	50
5.7	Triggering TTL signal for DIC image acquisition . . . . .	51
5.8	Example of a motion curve for target frequency of $3\text{Hz}$ . . . . .	52



5.9	DIC calibration target plate attached to its adapter plate . . . . .	53
5.10	DIC target plate rotated, during calibration for "dry" experiments . .	54
5.11	Force transducer loaded with test weights for calibration . . . . .	55
5.12	Results of force transducer calibration . . . . .	56
5.13	Results of triangulation laser displacement measurer calibration . . .	56
5.14	Achieved contrast between water and ambient air . . . . .	58
5.15	Schematic diagram of signal flow . . . . .	59
6.1	Sloshing inside the plunger . . . . .	61
6.2	Bubble travelling beneath plunger's bottom captured by DIC cameras	62
6.3	Final version of the experimental matrix for each case of plate thickness	62
6.4	External clock setting for image acquisition in DIC processing software	63
6.5	Selection of the region of interest . . . . .	64
6.6	Definition of mask including rigid parts . . . . .	64
6.7	Start-point search for reference measurement step . . . . .	65
6.8	Presentation of the evaluated facets and the achieved uncertainty . .	65
6.9	Indicative snapshots with results of a central FOV for Case Nr.2 . .	66
6.10	Deflections along the centre line of the FOV pictured in Figure 6.9 .	67
6.11	Gauge point at rigid part of the surface and exported temporal plot of $z$ - displacements . . . . .	68
6.12	Comparison of rigid body motion measurements between laser mea- surer and DIC cameras . . . . .	69
6.13	Velocity measurement by LDV keeping the plunger standstill . . . .	70
6.14	Result of FFT of LDV signal for standstill period of imported motion curve . . . . .	71
6.15	Response of the plate due to the imposed motion in frequency domain	71
6.16	Zoomed graph of rigid body motion response in frequency domain .	72
6.17	Graphs of rigid body motion, force and bottom plate's velocity in frequency domain . . . . .	73
6.18	Comparison between the bottom plate's response in frequency domain between "wet" and "dry" experiments . . . . .	74
6.19	Comparison of the plate's responses between different PID controller modes . . . . .	75
6.20	Comparison between the response of PTFE (flexible) and PMMA (rigid) plates in frequency domain . . . . .	76
6.21	RBM and velocity measurements for free-vibration test . . . . .	77
6.22	Response to free vibration test with and without noise included . . .	77
6.23	Raw and filtered LDV measurement . . . . .	78
6.24	Displacement comparison between DIC and LDV outputs . . . . .	79
6.25	Video camera placed next to water container and the achieved con- trast between water and ambient air . . . . .	80
6.26	Sketch indicating the coordinates of video camera . . . . .	81
6.27	Snapshots of recorded videos capturing water elevation . . . . .	81
6.28	Measured water elevation for Case Nr. 2 . . . . .	82
6.29	Measured peaks of water elevation at container's side walls . . . . .	83
A.1	Presentation of plunger's section geometry (reproduced from Koo W. (2015)) . . . . .	91
A.2	Dimensionless coefficients for added mass and damping . . . . .	92
A.3	Envelopes of required oscillation force . . . . .	93

B.1	PTFE specimen clamped with a digital extensometer attached . . .	95
B.2	Time series of strain during cyclic loading tests . . . . .	96
B.3	Calculated Young's Modulus for three specimens per load cycle . . .	96



# List of Tables

3.1	Natural frequency reduction compared to dry natural frequencies, in percentage. (Rodriguez et al., 2010)	13
4.1	Mechanical properties of tested materials (source: Idemat 2003, available at <a href="https://www.matbase.com">https://www.matbase.com</a> )	23
4.2	Values of $\lambda$ obtained by Iguchi (Leissa, 1969)	24
4.3	Values of $\lambda_{nk}^2$ for different combinations of modes (Leissa, 1969)	25
4.4	LDV sensor head OFV-505 technical data	34
4.5	LDV controller OFV-2200 technical data	34
4.6	Triangulation laser displacement measurer Micro-Epsilon ILD 1401-200 technical data	36
4.7	Load Cell technical data	37
5.1	List of parameters calculated during a calibration of DIC cameras	53
5.2	Achieved uncertainties for each calibration case	55
5.3	Velocity decoder of OFV-2200 measurement ranges	57
6.1	Investigated cases	63
6.2	Maximum deflections measured by DIC for all cases investigated	67
6.3	P, I and D parameter values for different controller modes	75
6.4	Characteristics of designed low-pass filters	78
6.5	NRMSD between DIC and LDV measurements of total displacements	79
6.6	NRMSD between DIC and LDV measurements of deflections	80
B.1	Properties of specimen used to determine the density	95
C.1	Values of $\lambda_{kn}^2$ for different modes (Leissa, 1969)	97
C.2	Dry natural frequencies fully clamped PTFE plates	97



# List of Abbreviations

<b>CCD</b>	<b>C</b> harge- <b>C</b> oupled <b>D</b> evice
<b>DAQ</b>	<b>D</b> ata <b>A</b> cquisition
<b>DIC</b>	<b>D</b> igital <b>I</b> mage <b>C</b> orrelation
<b>FOV</b>	<b>F</b> ield <b>O</b> f <b>V</b> iew
<b>FSI</b>	<b>F</b> luid <b>S</b> tructure <b>I</b> nteraction
<b>HDPE</b>	<b>H</b> igh <b>D</b> ensity <b>P</b> oly- <b>E</b> thylene
<b>LDPE</b>	<b>L</b> ow <b>D</b> ensity <b>P</b> oly- <b>E</b> thylene
<b>LDV</b>	<b>L</b> aser <b>D</b> oppler <b>V</b> ibrometer
<b>LED</b>	<b>L</b> ight <b>E</b> mitting <b>D</b> iode
<b>PID</b>	<b>P</b> roportional, <b>I</b> ntegral, <b>D</b> erivative
<b>PIV</b>	<b>P</b> article <b>I</b> mage <b>V</b> elocimetry
<b>PMMA</b>	<b>P</b> oly <b>M</b> ethyl <b>M</b> etha <b>A</b> crylate
<b>PTFE</b>	<b>P</b> oly <b>T</b> etra <b>F</b> luoro <b>E</b> thylene
<b>PVC</b>	<b>P</b> oly <b>V</b> inyl <b>C</b> hloride
<b>RBM</b>	<b>R</b> igid <b>B</b> ody <b>M</b> otion
<b>RGB</b>	<b>R</b> ed <b>G</b> reen <b>B</b> lue
<b>TTL</b>	<b>T</b> ransistor- <b>T</b> ransistor <b>L</b> ogic





# Chapter 1

## Introduction

### 1.1 General introduction

Fluid - structure interaction (FSI) refers to the coupled process of a fluid or fluids that share an interface with a non-rigid solid structure. Generally, the interaction can not only be described by means of the kinematic and dynamic properties of both domains, but also to thermal ones. This two- or multi- way coupled process finds applications to several scientific and engineering fields. Some characteristic examples are listed below:

- Biomedical engineering - blood flow in arteries, artificial heart valves
- Aerospace engineering - aero-elastic modelling of aircraft wings and wind turbine blades
- Civil engineering - galloping wind on bridges, seismic design methods for dams
- Mechanical engineering - pressure waves in flexible tubes
- Marine engineering - hydro-elastic modelling of vessels' hull under whipping due to slamming loads
- Offshore engineering - hydro-elastic modelling of vertical columns under ring-ing loads

### 1.2 FSI in marine applications - Trends

The current study is focused on applications of FSI in the marine environment. The main reason for dynamic responses of a floating structure is the hydrodynamic loading due to waves. The severity of loading and, therefore, the levels of structural response depends on the sea-state, the loading condition of the structure, its geometry (platforms, single-hull or multi-hull vessels), its service speed, etc. Traditionally, for the prediction of response due to environmental loading, floating structures are treated as rigid bodies. However, this practice can be followed up to a certain level of structural response. Beyond that level, the dynamic response and, also, the loading of a structure is affected by its flexibility. Moreover, aspects like resonance, dynamic response of certain structural components and their fatigue life-time can not be assessed using the rigid body assumption.

From the market's perspective, there is the need for more slender and faster vessels keeping their transportation capacity high. The expansion of human activities in the marine environment introduces the production of unconventional vessels. These, also, determine the strategy of other participants of the industry, such as the classification societies. Advanced designs require alternative, more sophisticated

computational tools for the formulation of up-to-date rules and guidelines (Hirdaris S.E., 2005).

The development of FSI computational tools has attracted a lot of interest the last decade. As stated above, there is a wide range of problems where FSI need to be taken into account. The physical processes met, can show great deviations among different fields of application. For the field of marine and offshore engineering, the physics that take place around the region of free surface are of utmost importance. It is, therefore, essential for a computational tool to handle the coupling process at the interface between a two-phase fluid flow and a structure. From the numerics point of view, a wide range of methods that can be employed, is available. Each of them would lead to a different level of accuracy and efficiency (Gene H., 2012). Then, the need to assess the applied methods arise. Physical experiments, designed to reproduce the investigated processes, can give validation data, that would evaluate the success of numerical simulations.

## Chapter 2

# Problem Statement

### 2.1 Objective

The non-linear, multi-physics characteristics of FSI problems and their wide range of applications, even within the marine/offshore engineering field, make analytical solutions hard to obtain and impractical to apply. Therefore, numerical methods are prevailing. The most common approaches involve the partitioning of structure and fluid domains. Usually, legacy algorithms are used for the solution of the inner part of the domains, but stable numerical schemes need to be developed for dealing with the two- or multi-way coupling at the interfaces. The coupling algorithms involve the exchange of kinematic (velocity, displacements, etc.) and dynamic (pressure) properties at each time step. Additionally, inner loops at each time step are needed to correct the solutions for both domains. Consequently, the development of a coupling algorithm is not a trivial task and due to lack of analytical models, there is a need of experimental data for validation. The purpose of this study is to create validation data for FSI computational tools. To achieve this goal, a physical experiment needs to be designed from scratch. Firstly, the required characteristics of the experiments and, subsequently, their design guidelines need to be clarified. This will determine the most suitable approach that needs to be followed. Finally, apart from designing and conducting the experiments, the results should be processed in order to ensure that the requirements were fulfilled and that the measurements are reliable enough, to be used as validation data for an FSI computational tool.

### 2.2 Designing considerations

The designing considerations for such an experiment derive from two facts. On one hand there are the physics that need to take place. On the other hand, there is the fact that the physical experiment should be feasible to be reproduced as a numerical experiment using a specific computational tool (i.e. ComFLOW). Contrariwise, any correspondence of the physical experiment to any problem encountered in real - life (e.g. slamming), is of minor importance in this case.

As far as the physics are concerned, apparently coupling between a fluid (water) and a structure should be present. One of the prerequisites to achieve coupling is that the structure involved should be of a relatively high inherent flexibility. The flexible structure should be excited and its response should be affected by the surrounding fluid (one-way coupling). Also, it would be ideal, if the response of the flexible structure, affects significantly the kinematic properties of the fluid (two-way coupling). The presence of free surface is not only necessary, but it should contribute to the resulting interaction between structure and fluid domains.

With respect to the latter source of designing considerations, some basic aspects of numerical simulations should be taken into account. One of the most significant

is the computational cost. The coupling algorithms that need to be employed are computationally expensive, making FSI simulations time consuming. It is important that the replica of the physical experiment using a computational tool should not add extra cost. One should have in mind, that the main reason of very costly simulations is a very fine spatial and temporal discretization, in order to keep the Courant number condition satisfied. Complicated geometries for both domains induce the need of finer, unstructured grids for accurate solution at the boundary layer regions and, therefore, need to be avoided. Additionally, it is preferable for the size scale to be retained to a reasonable level. Finally, the aspect of symmetry can, also, contribute to the containment of computational time.

### 2.3 Required measurements

The most crucial aspect when designing an experiment is the definition of the quantities to be measured and the instruments to be used for measuring these quantities. Apparently, measuring the deflection of the structure can offer data to assess the accuracy of the FSI solver. However, using conventional instruments to measure the deflection of an immersed flexible structure can distort both its mechanical properties and the velocity field of the surrounding fluid. Using optical measuring methods, such as *digital image correlation* (DIC) and *laser doppler vibrometer* (LDV), are the obvious solution to this problem. Another quantity that can offer validation data should come from the fluid domain, but the use of conventional measurers, such as pitot tubes or wave gauges would create the same unfavourable effects as in the case of the structure. The complexity arises from the fact that the use of many optical instruments may induce interference effects among the outputs. For example, the structure's deflections using DIC or LDV cannot be measured simultaneously with fluid velocity using a *particle image velocimetry* (PIV) setup. Consequently, at the initial designing phase, priorities should be settled and that resulted to the choice of deflection measurements.

## Chapter 3

# Literature Review

### 3.1 Introduction

This chapter contains a brief but comprehensive description of approaches used for the investigation of FSI problems. To begin with, the two prevailing numerical approaches are presented: the monolithic and the partitioned approach. Also, a comparison between those two is made by means of accuracy, stability and computational cost. Then, some experimental studies investigating the fluid-coupled vibrations of structures are presented. Greater focus was given on the description of studies related to the vibrations of submerged plates, since this topic is strongly related to the present thesis. Finally, there is a brief description on how FSI appears on marine and offshore structures and related studies are described.

### 3.2 Numerical methods for FSI problems

The FSI phenomenon is characterized by its complexity and multidisciplinary nature. Although FSI takes place in many scientific and engineering problems, its study has wide margins for development. In most cases, analytical solutions can not be employed (Gene H., 2012). This deficiency derives from the fact that basic aspects of fluid and solid domains are treated differently. One of this aspects is the system of coordinates: in solid mechanics, the displacements are expressed in Lagrangian coordinates, while in fluid mechanics the moving Eulerian coordinates are preferable. This inconsistency play a prominent role at the interface between the two domains, since a direct coupling is infeasible (Frei S., 2015). On the other hand, most of the data obtained from experiments refer to very specific applications. All these facts raise the need to utilize numerical simulations for the solution of FSI problems (Gene H., 2012).

The approaches followed for the employment of these simulations can be classified into two groups: the monolithic and the partitioned. The differences between these two approaches refer to the mathematical framework employed and will be discussed in the following paragraphs.

#### 3.2.1 The monolithic approach

In the monolithic approach both the fluid and structure domains are modelled by a single non-linear, discrete system of equations. A unified algorithm is employed to solve the entire system, using implicit temporal schemes for the inter-facial conditions (Gene H., 2012). Such schemes can preserve conservation properties. In other words, this approach offers unconditionally stable solutions. This means, that the size of the imposed time-step is restricted only by means of accuracy (Ryzhakov P.B., 2010)

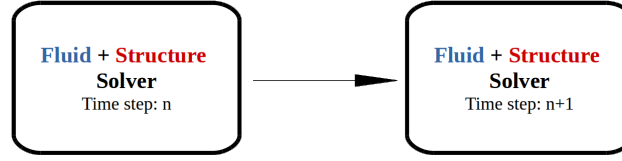


FIGURE 3.1: Schematic presentation of the monolithic approach

On the downside, the non-linearity imposes the use of iterative solvers. This makes the computational cost to be rather high, since multiple iterations for a single time-step are necessary. Moreover, The resulting system of equations tends to be large and complex with a great number of fields involved like the fluid velocity and pressure and the structure's deflection. Apparently, the scaling and the choice of the reference system used for these variables make the formulation of this unified system a very demanding task.

### 3.2.2 The partitioned approach

In the partitioned approach the sub-domains are treated separately. The algorithms built for the solution of the two separate systems are based on the legacy solvers from the fields of computational fluid and structural dynamics. As a consequence, the code development focuses on the coupling between those two sub-systems, in a way that the separate solvers are not modified significantly (Gene H., 2012). The steps typically followed in partitioned methods, are well described by Michler C. (Mar. 2003):

1. Displacement and velocity data of the structural domain are transferred to the fluid domain
2. The position (or/and topology) of fluid domain's computational mesh is updated.
3. Solve fluid domain's system at the new time point
4. Compute the new structural load based on the fluid's pressure
5. Solve structural domain's system at the new time point

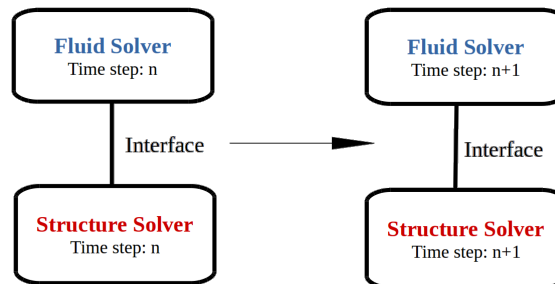


FIGURE 3.2: Schematic presentation of the partitioned approach.

It is clear that in partitioned methods, the solution per time step requires only one iteration between the two sub-domains, but this does not mean that the coupling procedure is a trivial task. Contrariwise, it is rather possible that the two separate solvers use different discretization techniques. Most of the structural solvers are based on finite elements while computational fluid dynamics use the finite volume method. It is, therefore, necessary that the quantities at the interface should be interpolated at the appropriate positions before they are exchanged (Gatzhammer, 2008). The complexity of this method comes from the fact that the interface location and the quantities of the separate fields are unknown functions of time. The tracking of those quantities appears to be most challenging objective when coding an algorithm that uses this approach (Gene H., 2012). In this part, a coupling error is, inevitably, introduced. In partitioned systems there are two possible approaches for the coupling procedure: weak and strong coupling.

Another crucial fact, is that the two domains are solved asynchronously. The conservation properties at the interface become questionable and instability may be induced. Apparently, the time step should be the same for both domains. However, the stability requirements and, therefore, the maximum required time step for the two sub-systems are different.

### Weak coupling

In a weak coupled system, no iterative procedure is required to obtain the solution. Apparently, this may lead to questionable accuracy and stability, especially for large time steps in the temporal discretization scheme. Only for rigid structures, the error may not be significant. A weak coupled system can be either one-way or two-way coupled. In the latter approach, data are transferred from and to both sub-domains (Richter, 2010). (Fig. 3.3).

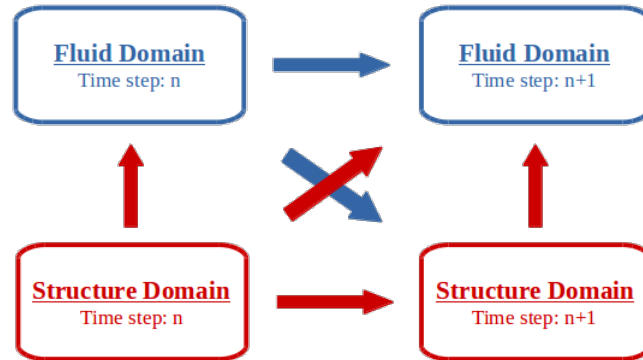


FIGURE 3.3: Schematic presentation of weakly coupled systems.

### Strong coupling

In strongly coupled systems, an iterative procedure is executed between the solutions obtained, following the aforementioned steps, of adjacent time steps. These outer iterations have a significantly adverse impact to the efficiency of the algorithm. The computational cost can be increased in such extent, so that a strongly coupled partitioned algorithm is less efficient than a corresponding monolithic. On



the contrary, any amplification of the solution (i.e. instability) can be restricted in some extent (Richter, 2010) (Fig. 3.4).

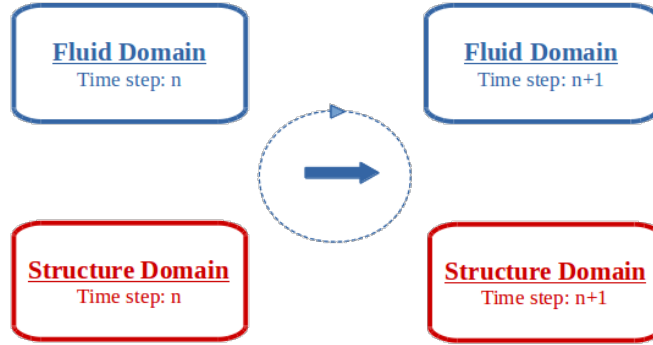


FIGURE 3.4: Schematic presentation of strongly coupled systems.

### Prediction and under-relaxation

As already discussed, in partitioned methods the domain-splitting error can be significant. Moreover, they are prone to instability. For those reasons, the execution of the aforementioned procedure is modified with the tricks of prediction and under-relaxation.

Using prediction, in the solution of the fluid domain (steps 2 and 3) the motion of the structure is not the one obtained from step 1 which refer to the current time point. Instead, the quantities obtained from step 1 are extrapolated to next time point. The scheme of extrapolation that is applied, depends on the temporal discretization scheme used for the structural domain and the physics of the structure's motion (e.g. degrees of freedom, modes, etc.) The concept of prediction can be used, also, in monolithic methods in order to reduce the number of iterations (Michler C., 2003).

Predicting the quantities of structure's motion can lead to better accuracy, but then the **under-relaxation** technique is applied in order to enhance stability. Let  $q^l$  be a quantity of the fluid or structure domain at iteration step  $l$ . If  $\tilde{q}^{l+1}$  is the first estimate of the quantity at the next time point, the new input of the quantity is a linear combination of the previous solution and the first estimate:

$$q^{l+1} = \theta \tilde{q}^{l+1} + (\theta + 1) q^l \quad (3.1)$$

Where  $\theta$  is the so called under-relaxation factor and its value ranges from 0 to 1.

The under-relaxation factor can remain constant (*fixed under-relaxation*) during all iterations or can change during the process accordingly.

When the fixed under-relaxation iteration scheme is used, the value of  $\theta$  must be chosen carefully. For  $\theta$  close to 1 the algorithm can still be unstable and for  $\theta$  close to 0 the iteration process may require large number of loops to converge, sacrificing efficiency.

In adaptive under-relaxation (Yigit S., 2007) schemes  $\theta$  is only chosen at the first iteration. Then, the residual  $r^l$  determines the value of  $\theta^{l+1}$ . For example, in *Aitken's* method which is the most common the under-relaxation factor is determined by the

following formula:

$$\theta^{l+1} = \theta^l \left( -\frac{(r^l - r^{l-1})^T r^{l-1}}{(r^l - r^{l-1})^T (r^l - r^{l-1})} \right) \quad (3.2)$$

With,

$$r^l = \tilde{q}^{l+1} - q^l \quad (3.3)$$

In this way, stability is secured and the efficiency of the algorithm is better comparing to a fixed under-relaxation scheme with low values of  $\theta$ .

### 3.2.3 Monolithic vs Partitioned methods

Concluding the description of the prevailing numerical methods, a brief comparison between their basic aspects follows. Using partitioned methods, the computational cost is limited to lower levels, since only one iteration between the two sub-systems per time step is required. However, during the coupling of fluid and structure domains the tracking of the interface conditions is an error-prone procedure. It is inevitable that at this point, artificial energy is produced which may lead to instability. To enhance the efficiency and stability of partitioned algorithms, prediction and under-relaxation techniques are employed.

On the other hand, the computational cost of monolithic schemes is generally larger and the resulting accuracy is of high level. This comes from the fact that multiple iterations per time step are required. However, the monolithic algorithms are unconditionally stable due to the implicit schemes applied at the interface conditions. As a consequence, the time step size can take larger values than in partitioned algorithms and obtain similarly accurate solutions. But this does not refute the fact that monolithic algorithms are, most of the times, less efficient than the partitioned.

### 3.2.4 Conforming and non-conforming mesh methods

Apart from the mathematical framework, another criterion used to classify the FSI solvers is the treatment of the computational mesh. There are two methods used to build computational meshes in FSI problems, namely the conforming and non-conforming mesh methods.

In **conforming** mesh methods, the interface between fluid and structure is treated as a physical boundary. During the simulation, the location of grid nodes are updated according to the motion of the structure in a way that the solution incorporates the interface conditions.

In **non-conforming** mesh methods the grid nodes are not required to move, as the solution advances. The equations of both domains are solved independently and the interface conditions are applied as constraints imposed in different location within the computational domain as the simulation evolves.

An illustrative graphical example of those methods is presented in the study of Gene H., 2012 and, also, shown at Figure 3.5. The structure is a sphere that moves through the fluid domain.

## 3.3 Experimental methods for FSI problems

The dynamic characteristics of fluid-coupled plates have been studied extensively the last two decades. The researchers investigated this fluid-structure interaction

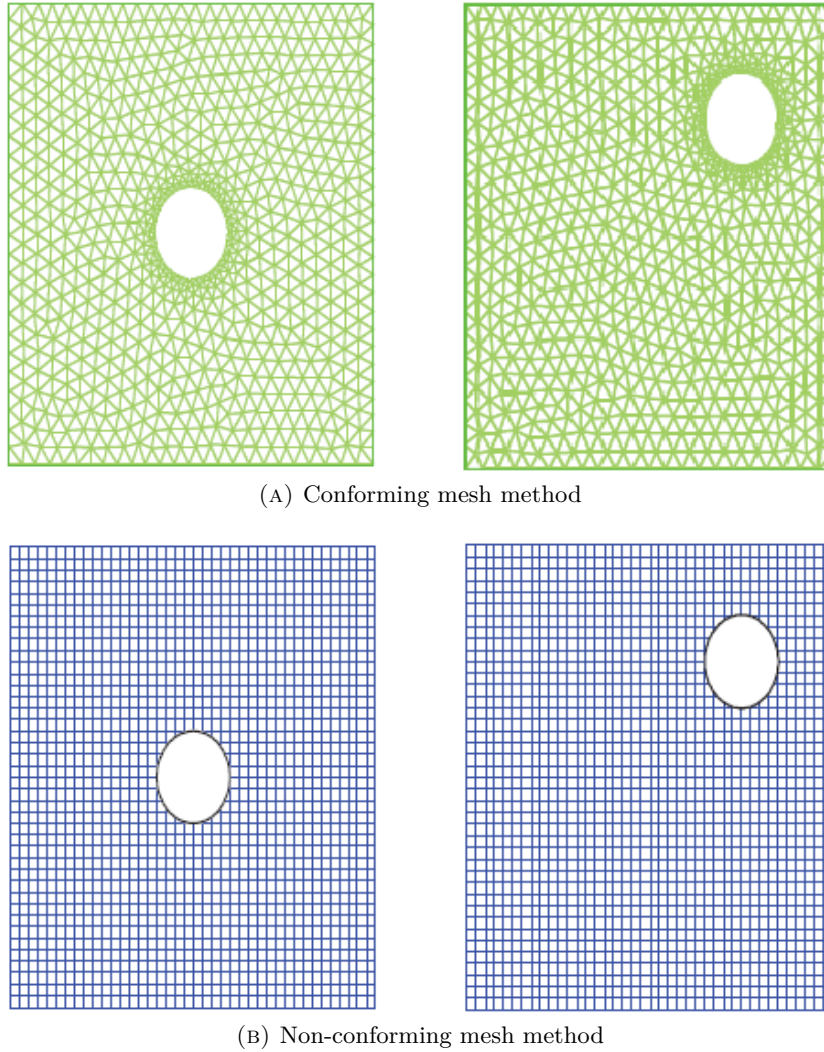


FIGURE 3.5: Schematic presentation of conforming and non-conforming mesh methods (Gene H., 2012)

problem from different perspectives. Beside their theoretical or analytical models, researchers needed to conduct experiments for validation. Most of the case studies refer to the vibration of plates that are in contact with water: floating plates on infinite, semi-infinite or bounded fluid, bottom plates of water containers and cantilever plates that are partially submerged in fluid. However, in the present literature review greater attention is given to the studies that investigate the vibrations of fully immersed plates. Therefore, experimental studies that investigated the vibrations of submerged plates, are described in more detail.

### 3.3.1 Vibrations of fluid-coupled plates

Experimental and empirical study was conducted by Brugo T. (2012) for the investigation of the vibration of vertical cantilever rectangular plates for various depths of submergence. Plates of different widths and thickness were tested. With respect to the materials, aluminium and fiberglass epoxy plate were used. The oscillation was an impulsive load and a sealed strain gauge mounted on the plate, was used to measure the vibrations. The output signal was cut into segment each of which correspond to a specific time point. Then, the Fast Fourier Transform was applied

to each segment. In this way, the natural frequencies of the first three mode shapes were determined. For an aluminium plate of  $2 \times 50 \times 275\text{mm}$  with submergence depth equal to 54.5% of the free length, the reduce of the natural frequencies for the first three mode shapes were 61.4%, 48.5% and 32.7% respectively, compared to those in vacuum. For a fiberglass plate of  $2 \times 150 \times 275\text{mm}$  with submergence depth equal to 72.7% of the free length, the reduce of the natural frequencies for the first three mode shapes were 72.9%, 69.5% and 60.9%, respectively.

The vibrations of the flexible bottom in annular cylindrical tank has been investigated theoretically and experimentally by Amabili M. (1998). Great focus was given at the bulging modes of the annular plate. For the experimental phase, two test specimens were constructed. The first consisted of two coaxial PVC pipes rigidly connected to each other with a Plexiglas annular lid bearing two holes so that that water can be filled in. The bottom was made of low carbon steel and had annular shape. The outer edge was set to be simply supported and the inner edge was free, as a very thin film connected the inner cylinder to the plate's edge. The second boundary condition This whole arrangement was glued to a stiff steel support. The second specimen did not include an inner cylinder and the bottom was of circular shape. The excitation was imposed using an impact hammer at 18 different points and the response was measured at two points with light accelerometers. Tests were conducted with the tanks empty and partly filled with water at five different water levels. The frequency response functions and the experimental modal parameters were determined using specialized software. The results involved the fundamental mode (zero nodal circles and diameters) and the first asymmetric mode (zero nodal circles and one nodal diameter). The impact of the water level inside the tank to the natural frequencies of the aforementioned mode shapes was investigated. For both cases, increasing the water level caused a decrease to the natural frequencies but when the water level approached the value of the plate's radius, the frequencies showed an asymptotic behaviour to a constant value.

Chiba (1992) investigated the non-linear vibrations of a flexible plate used as the bottom of an otherwise rigid cylindrical tank partly filled with water. Great attention was given, also, to the sloshing modes of the free surface and the coupling characteristics between the plate, imposed to harmonic excitation, and free surface response for various water heights. The flexible plates were made of polyester and their edges were clamped. The excitation was imposed by an aluminium rod. Optical sensors were used to measure the plate's deflections and the free surface motion. With respect to the plate's vibrations, the natural frequencies decreased up to a certain level of water height. Beyond this level, all natural frequencies but the fundamental one, increase due to the in-plane tension caused by the heigh water's weight. As far as the coupling between plate's and free surface's response is concerned, the interaction appeared to be greatly influenced by the water height. For low heights, the free surface exhibits a parametric response to the plate's vibrations, since its frequency response curves have a peak at the half of the plate's oscillation frequency. Moreover, the amplitude of the plate's vibration is lower, suggesting that the free surface suppresses the plate's response. On the contrary, for higher water heights the frequency components of the plate's and free surface's response coincide showing a forced vibration behaviour.

### 3.3.2 Vibrations of submerged plates

The vibration of submerged rectangular, horizontal plates was studied analytically and experimentally by Haddara M.R. (1996). The type of boundary conditions and

the submergence depth were the investigated parameters. Both types of boundary conditions tested involved mixed conditions with the longer edges to remain free. At the shorter edges, clamped (CFCF plate) and simply supported (SFSF) conditions were applied. The theoretical analysis involved the first three bending mode shapes but the experimental study involved, also, the first two torsional mode shapes. The formulation of the theoretical model was based on the assumption that the plate undergoes free bending vibrations of small amplitude, so that the membrane stresses were not taken into account. The external load derives from the difference between the dynamic fluid pressures at the upper and lower sides of the plates. The small-amplitude vibration induce small fluid motions and, therefore, the fluid flow was assumed to be incompressible, irrotational and inviscid. The pressures were obtained by the Laplace equation of the velocity potential and the non-stationary Bernoulli's equation. The conditions applied at the boundaries consisted of a linearised free surface condition, homogeneous von Neumann conditions for the velocity potential in the normal to the walls direction. At the fluid-structure interface, compatibility kinematic and dynamic conditions were applied. The solution of the resulting system was simplified by using the separation of variables technique. For the determination of the added masses and, subsequently, the natural frequencies the contributions of the fluid beneath and above the plate were calculated separately. With respect to the experimental set up, the plates ( $655 \times 201.65 \text{ mm}^2$ ) were placed inside a cubic tank ( $1,3 \times 0,55 \times 0,8 \text{ m}$ ). The imposed excitation was of fast sine sweep type and was transmitted to the plate through a single connecting rod. The excitation force was measured by a force transducer installed between the connecting rod and the plate. The plate's vibrations were captured using 15 accelerometers of 3gr. The clamped boundary condition was applied by placing the plate's short edges between steel blocks. The simply supported boundary condition was obtained by a more complicated configuration. The plate had to be notched at specific locations near the short edges. The dimensions of the notches were determined by simulating the problem in a finite element software. The plate's responses were analysed by a modal analysis software in order to obtain the mode shapes, damping ratios and natural frequencies. The results revealed that the differences between the dry and wet mode shapes were negligible. As far as the wet modal damping ratios are concerned, the values for the torsional modes of the clamped plate were from 20% up to 140% larger than the dry ones. The corresponding values for the simply supported plate were from 20% up to 90% larger than the dry modal damping ratios. The increase was steady up to depths of 10% of the plate length and then the damping was stabilized to a certain value. For the bending mode shapes, the magnification of the damping ratios due to the surrounding water was greater. The increase for the CFCF plate was of 180% up to 300% and from 120% up to 310% for the simply supported plate. The increase of damping versus the depth of submergence showed more or less the same behaviour as in the case of the torsional mode shapes. Referring to the added masses, their values ranged from 50% up to 80% of the structural mass for the torsional modes and from 75% up to 200% for the bending modes. The increase with respect to submergence depth had the same characteristics for both types of mode shapes as in the case the case of modal damping ratios. For both boundary conditions the added mass of the first bending mode is equal to about two times the structural mass. Therefore, the wet natural frequencies were measured to be 31 and 32% smaller than the dry ones for CFCF and SFSF plates respectively. Comparing the results of the analytical and experimental studies, the deviations between calculated values of added masses were negligible for the clamped plate. For the SFSF plate the deviation reached the value of 8% which is larger but

not significant. The larger deviation was attributed to the level of success in the application of the simply supported boundary condition at the experiments.

A comprehensive experimental study on the vibrations of submerged plates was presented by Vu V.H. (2007). Five steel rectangular plates of different dimensions and different boundary conditions were tested both in vacuum and inside a water container. Three of the plates had only one of their boundaries clamped (CFFF) and two of them had two clamped edges (CFCF). For each type of boundary conditions one of the plates tested had equal length and width. Eight accelerometers were attached on each plate to measure the vibrations. The excitation was imposed by an impact hammer. The effect of submergence depth to the natural frequencies, damping ratios, added masses and mode shapes was investigated. The results showed that the decrease of natural frequency was more significant for the first bending mode. This decrease of frequencies reached the value of 69% for a rectangular CFCF plate. The frequency changes were sharp in depths smaller than 10 to 20% of the plate's length. The same applied for the added mass which was stabilised for depths larger 30 – 40% for rectangular and 40 – 50% for square plates. The effect of added mass, which took values up to 10 times the structural one, was more intense for the first bending mode shape. For the damping ratios the results were much different among the banding modes. More specifically, the submergence of the plate can cause either increase or decrease of damping.

The effect of a nearby wall to the vibration of a submerged cantilever horizontal plate was investigated by Rodriguez et al. (2010). A series of experiments were conducted, during which the cantilever plate was subjected to free vibrations using an impact hammer. The experimental set up was designed in a way that the vertical distance between plate and bottom (rigid wall) was controlled. The vibration of the plate was measured by a single point displacement sensor and, therefore, the mode shapes were not investigated. Impact excitations were imposed at fifteen different positions, but the measuring point remained the same. Then, the averaged frequency response function was calculated and the natural frequencies were approximated using the complex exponential method. The results consisted of the natural frequencies of three bending and two torsional mode shapes for 5 cases of vibration: plate in vacuum, infinitely submerged plate and three additional cases which by means of the vertical distance between the plate and the bottom. The reduction of natural frequencies compared to those found in vacuum test are summarized in the following table. The distance ( $h$ ) between the plate and the bottom was normalized with the plate thickness ( $t$ ). It is shown that as the plate is placed closer to the wall there is a drastic reduce of the natural frequencies, especially for the bending mode shapes. That conclusion agrees with the results of previously described studies, where it was observed that the added masses show a great increase as the plate is placed closer to the bottom.

Mode Shape	Infinitely submerged	$h/t=9.03$	$h/t=0.87$	$h/t=0.33$
$B_1$	55.1	57.5	71.4	76.7
$B_2$	53.9	56.0	72.7	76.4
$B_2$	53.4	53.8	69.1	75.6
$T_1$	42.0	42.8	57.1	61.0
$T_2$	40.8	41.7	54.8	59.8

TABLE 3.1: Natural frequency reduction compared to dry natural frequencies, in percentage. (Rodriguez et al., 2010)



The hydroelastic vibration of circular horizontal plates fully immersed in a liquid container was investigated theoretically, numerically and experimentally by Askari et al. (2013). The container is, also, circular and the immersed plate is placed concentrically to the container. With respect to the boundary conditions, the cases of clamped and free edges were studied. The effects of free surface and sloshing at the container's walls were taken into account. From theoretical point of view, the plate's wet mode shapes were formulated as a finite series of linearly independent basis functions, which correspond to the modal functions of the dry plate that satisfy the applied boundary conditions. With respect to the fluid domain, potential flow was assumed. The domain was divided to the parts above and beneath the plate's horizontal plane. The velocity potential was decomposed to the potential derived from sloshing and the one derived by the plate's deflection. The former part of potential was calculated assuming that the plate is rigid. With respect to the boundary conditions, kinetic and kinematic boundary conditions were applied at the free surface, continuity condition was applied at the interface between the upper and the lower part of the fluid domain. Finally, compatibility condition was applied at the fluid-plate interface. Having the fluid potential and the plates wet modes fully defined, the wet natural frequencies were calculated using the Rayleigh-Ritz method. In the experimental phase of the study, two types of steel plates with different dimensions were tested, both with clamped and free edges. Apart from submerged plates, the test were executed for plates surrounded by air. The excitation was imposed by an electro-dynamic exciter at a single point away from the plate's centre. The response of the plate was captured by a laser Doppler vibrometer placed beneath the transparent bottom of the liquid container. The deflections were measured at multiple points. These point were nodes of a grid created by equally spaced diameters and circles. The wet natural frequencies obtained by the experiments showed great agreement with the results of the theoretical model. The wet natural frequencies were from 28% to 55% smaller than the corresponding dry ones. The natural frequencies were obtained for different values of the plate's vertical position inside the container with fixed total water height. The results revealed that the natural frequencies decrease as the plate's position moves from the surface to the bottom. However, within regions near the surface and the bottom, the decrease is drastic. The size of these regions depends on the plate's vibration mode shape. For lower modes, where the effect of added mass is dominant, these regions are larger. For the rest of the water domain (i.e. region near the centre) the natural frequencies showed negligible decrease as the plate's position moves downwards to the container's bottom. The wet damping ratios calculated from the experimental results were greater than the corresponding dry ones. However, they still had very small values (0.04% - 0.95%) and, therefore, the assumption of an inviscid fluid is not unfounded. Conclusively, it can be mentioned that the study's theoretical and experimental results showed good agreement for all the investigated aspects.

### 3.4 FSI in marine and offshore structures - Hydroelasticity

#### 3.4.1 Slamming

One of the most notorious water-impact problems faced in marine and offshore engineering is slamming. Slamming phenomena are categorized by means of the areas where they occur along a vessel's hull. These areas are the bow stem and flare, the bottom (keel) and even the aftship zone. For multi-hull vessels, slamming



typically occurs at the structural part that connect the hulls, named wetdeck. The area of the hull that can suffer from slamming depends on the type of the vessel (i.e. hull's shape), the environmental conditions and, also, the service speed. The effects of slamming can be pronounced locally, as vibrations and strain peaks at certain structural parts of the hull (Faltinsen, 1997) or globally, as severe accelerations along the hull. In both occasions, the typical approach that models the hull as a rigid girder is not accurate and, therefore hydroelastic approaches must be applied.

### Bow-flare and keel slamming

A fully hydro-elastic method for the calculation of local and global responses to seakeeping loads (bow-flare and keel slamming incorporated) was formulated by Tuitman (2010). In a small part of his study, he determined the effect of hydro-elasticity by separating the ship's hull vibration modes to elastic and rigid. Also, the ship's response and internal loads were decomposed into quasi-static and dynamic. Only the former ones are taken into account in traditional rigid-body analysis. The case-study used was an ultra large container ship of 360 m length. The results revealed that at the fundamental wet natural frequency the bending moment at midship is significantly underestimated. Moreover, at lower than resonant frequencies the quasi-static solution fails to calculate dynamic amplifications of the bending moments and, therefore, the hydro-elastic analysis is considered to be very important in the prediction of a ship's response to seakeeping loads.

### Wetdeck slamming

Faltinsen (1997) investigated the case of *wetdeck slamming*. His study aimed to determine the maximum strains in the longitudinal stiffeners of the wetdeck due to slamming. Therefore, corresponding theoretical and experimental models were created to investigate the wave impact at the structural part between two transverse frames (one-beam model) and four serial transverse frames (three beam model). In both cases, pressures and strains along a horizontal plate that falls at the water surface of propagating waves, were approximated. Multiple drop velocities and wave steepness cases were tested. For the one-beam model, Faltinsen used the results of the experiments executed by Aarsnes (1994) for validation of his theory. The analysis was divided into two phases: the structural inertia phase and the free-vibration phase. During the former one, which has time scale much smaller than the first natural period of the plate, the maximum pressures occur. These maxima are very concentrated in space and time and, therefore, they do not induce maxima of stresses and strains. In this phase, the plate's elasticity is not important. The end of this phase comes when the space-averaged vibration velocity equals the drop velocity of the specific time point. Then, the free-vibration phase starts. At this phase, the maximum strains occur. The first vibrational mode is dominant. At the second half of the first oscillation cycle, large underpressures were observed. This means that ventilation and cavitation take place and, therefore, the plate's wetted length is reduced. As a consequence, the added mass and the wet natural period are reduced. Also, the strain amplitude is reduced. The effects of ventilation and cavitation were not taken into account in the theoretical model. Therefore, significant differences between the theoretical and experimental results were observed from the second half of the first oscillation cycle and beyond. Conclusively, the experiments revealed that the relation between the maximum strain amplitude and the drop velocity is proportional. In the three beam model, the initial phase, when the impact of the plate occurs, lasts a bit longer. The air cushion created between the plate and the

wave during this phase has more significant effects than in the one beam model. In the free vibration phase, besides the first one, other modes are dominant. With respect to the maximum strains, these showed similar behaviour as with one beam model, although their amplitude appeared to be a slightly higher. As in the one beam model, the maximum strain amplitude is proportional to the drop velocity. The effect of the initial wave impact region to the maximum strains, was, also, investigated. This was done by changing the relative angle between the plate and the water surface. The results showed that the maximum strains are large for relative angles smaller than  $2^\circ$ . For angles larger than  $2^\circ$ , the maximum strains decrease as the angle gets larger.

### Aftship slamming

*Aftship slamming* is a non-favourable phenomenon that appears mostly at passenger ships, like cruise liners. It can cause severe accelerations along ship's hull, increase of global bending moments and high stresses at the region of impact (stern). The role of hydroelastic analysis of aftship slamming to the assessment of its effects on ship's performance was investigated by Bereznitski A. (2002). The case study was a cruise liner of 42000t,  $L_{OA} = 290m$  and  $B = 32m$ . The model consisted of a beam representing the hull girder and a sequence of shell elements attached to the beam that represent the ship's transverse frame at the slamming region. Air and water were modelled using solid elements. In order to quantify the effect of hydroelastic analysis in comparison with the traditional approaches, five models had been considered:

1. Fully hydroelastic approach. The hull girder and the transverse frame were flexible.
2. Traditional global approach. For the water simulations, both the hull girder and the transverse frame were assumed to be rigid. However, for the structural analysis the girder was assumed to be flexible
3. Traditional local approach. As in the traditional global approach, both structural members were considered rigid, but for the structural analysis, the girder is rigid and the frame flexible.
4. Local hydroelastic approach. For both simulations the girder was considered to be rigid and the transverse frame flexible.
5. Global hydroelastic approach. For both simulations the girder was considered to be flexible and the transverse frame rigid.

The simulations involved the free fall of the structure with initial velocity. During aftship slamming, the transverse frame at the stern penetrates the water and its vertical velocity decreases due to the hydrodynamic loads. This impact excitation induces vibrations locally (frame) and globally (girder), but the global ship motion is not affected severely. The results obtained by the simulations of the first model were compared to the results of the other models. It has been revealed that traditional models (2 and 3) overestimate the global bending moment due to the hydrodynamic load by 33% in comparison to the results of fully hydroelastic model. With respect to the local stresses and displacements, hydroelastic analysis gave reduced values of up to 30%. However, the girder's acceleration due to slamming, which induces passenger's discomfort, were not found be reduced in such extend.

### 3.4.2 Green Water

Offshore floating structures and ships in transit can find themselves before adverse weather conditions. During these severe conditions, the combination of very high waves and the structure's response can lead to significant amount of water to surpass the level of the structure's main deck. The water that flows to the structure's deck, typically, consists of drops of water and foam (spray) and solid seawater. The latter part can induce severe loading to superstructures and machinery placed at the bow area of the deck, generally known as *green water loading*.

The effect of green water loading on a Floating Productions Storage and Offloading (FPSO) vessel have been studied extensively by Faltinsen, Greco, and M. (2002). Although the study was not based on hydroelastic models, the cases at which hydroelasticity has a dominant role were determined. Since there is no forward velocity, the water flow on the deck was simulated using dam-breaking and shallow water approximations. According to the researchers, hydroelastic analysis is required for the structural components that have wet natural period larger than the duration of the green water loading. Therefore, it was concluded that for high impact velocities hydroelasticity becomes significant.

### 3.4.3 Ringing

In the last few decades it has been ascertained that large floating and bottom founded offshore structures can be severely oscillated at frequencies much higher compared to dominant wave frequencies. Single and multi-column offshore structures (semi-submersibles, gravity based structures (GBS), tension-leg platforms (TLPs), offshore wind turbines, etc.) are more prone to experience this transient phenomenon, known as 'ringing'. During ringing response, the deflections are relatively small and, therefore, environmental loads can be calculated at the initial position. However, the stresses appear when the structure vibrates and contribute to the structure's fatigue damage. Ringing has been correlated to sea states of steep waves with high peak frequencies and it is influenced by the fluid's motion around the vertical columns at the level of free surface. Moreover, studies that investigate the effect of other parameters such as the water depth (Bredmose et al., 2013) and the column's cross-section geometry (Faltinsen, 1999) have been presented. The prevailing theories for wave diffraction can not predict the high frequency loads, especially for slender columns. The required models should incorporate the non-linear components of the flow (Faltinsen, Newman, and Vinje, 1995), wave directionality and the fluid-structure coupling (Tromans, Swan, and Masterton, 2006). The importance of coupling between the structure's motion and the hydrodynamic loading has been experimentally determined (Chaplin, Rainey, and Yemm, 1997).



## Chapter 4

# Methodology

### 4.1 Introduction

Having reviewed the different approaches being followed for the investigation of FSI, the experiments that refer to this study need to be designed. The designing process has the following steps. First, a preliminary design of the experimental set-up has to be created. For this reason, two alternative set-ups are described and compared. These alternatives differ not only by means of the arrangement itself but, also, by mean of strategy that the forthcoming experiments can follow. After making the comparison and the decision of which of the examined alternatives is the most preferable, all aspects of the experiments were determined. These aspects refer to the detailed design of the set-up, the required measuring instruments and the strategy of tests that will be conducted.

### 4.2 Objectives of the experiments

Before starting the designing process, the goals of the experiments have to be clarified.

1. Beginning with the obvious, the experiments have to simulate a coupled fluid-structure system. This means that the fluid's flow field should influence the motion of a structure which then, ideally, have to distort the flow field.
2. Another primary goal is to offer validation data for any FSI solver that is under development. For this reason, the geometry of the set-up and any imposed motion or excitation should be easily reproduced by the solver's user. This may restrict the possibility for the experiment to model any of the FSI applications appeared in the marine environment.
3. The results of the forthcoming experiments will offer validation data, also, to the FSI solver that is currently developed in TU Delft, named ComFLOW. For this reason, the physical processes that will take place in the experiments must cover the capabilities of ComFLOW solver:
  - Fluid-structure coupling
  - Free surface effects

### 4.3 Investigation on the experimental set-up

In this section, two alternative designs of the experimental arrangement are presented. Since FSI is the field of interest, the arrangement should consist of a deformable structure that is in contact or surrounded by fluid. As already mentioned,

one of the most significant aspects of the arrangement is that it must be easily replicated in any FSI solver. Consequently, the geometries of both fluid and structure domains should not be complicated.

With respect to the latter, a plate has the shape that can be easily used in both physical and numerical experiments. A crucial aspect in the modelling of the structure is the boundary condition. For reasons of convenience, one of the typical boundary conditions (free, simply supported or clamped) should be uniformly applied at the edges.

As far as the fluid domain is concerned, it should include both phases (water and air) so that the effect of free surface can be taken into account. Moreover, it is preferable, that no complicated structure intrudes the water domain. This means (among others) that the oscillation can not be imposed to the structure with common ways used in the study of vibrations, like an impact hammer. Also, the use of wave gauges for the measurement of any free surface elevation that may occur, has to be avoided.

The aforementioned points refer to basic characteristics that the experimental arrangement should feature. According to these points some alternative designs were created. The major difference between them lies on the way the oscillation is imposed to the structure. Apparently, this is expected to lead to significant differentiations to other features of the design, which are extensively described in the following paragraphs.

### 4.3.1 1st approach: excitation through a moving object

#### Description

This approach is based on the premise that a flexible structure, in contact with non stationary fluid, can deform and this deformation can disrupt the water velocity and pressure fields, considerably. The velocity field that causes the structure's deformation, can be produced by an object which starts to move inside initially calm water. Using this rationale, preliminary designs of an experimental arrangement were created. In these designs, there is water container with flexible bottom, no lid and an object of cylindrical shape placed inside water. The cylinder is attached to a linear motor placed above the water container that imposes a periodic motion in the vertical direction. The quantity that gains most of the interest is the deformation of the flexible bottom plate.

#### Design aspects

##### 1. Arrangement of bottom plates

As already mentioned, the application of the boundary conditions at the flexible plate, is one of the most crucial parts of the design. Generally, simply supported boundaries on a plate are difficult to be implemented in physical experiments. On the contrary, it is easier to obtain fully clamped edges successfully. To achieve fully clamped boundary conditions, uniformly distributed load should be applied at the plate edges. Therefore, glued, direct bolted or any other type of connection, that would create non uniform loading must be avoided. Alternatively, the flexible plate can be placed between two rigid plates that have identical slots. The slot shape can be either rectangular or circular. Both plates bear a perforated flange so that they can be attached to the container's side walls through screwed connection, as shown in Figure 4.1. The region of rigid plate's slot, where the bottom consists only of the

membrane, has the role of a deformable structure that will vibrate due to an imposed excitation.

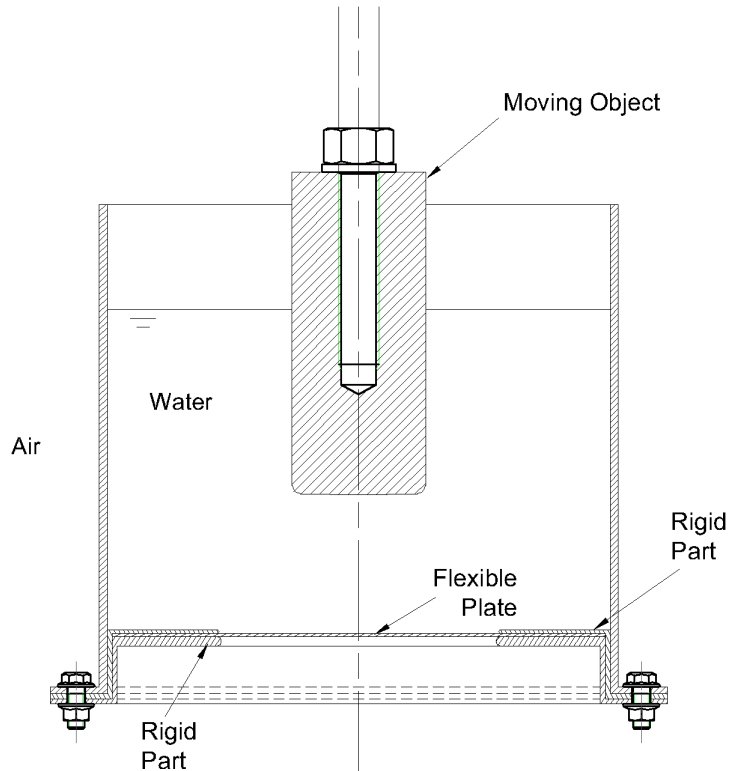


FIGURE 4.1: Preliminary sketch of the 1st approach

Since FSI is the field of interest, the goal is to achieve considerable deflections that can lead to significant disruptions to the fluid field. In an arrangement like the one described above, it is not probable to fulfil this goal if the bottom's plate is made of a metallic material. On the other hand, elastomer (rubber) materials are prone to get permanently deformed (creep) and, therefore, should be avoided, as well. Consequently, the investigation for the bottom's plate material was limited to plastic materials of medium stiffness. The final cases examined and the basic mechanical properties are shown at Table 4.1.

## 2. Moving object

The shape of the moving object is another aspect of the general arrangement that requires attention. First, the objective of designing an experimental arrangement that can be easily replicated for numerical experiments must be kept in mind. With respect to the moving object, this is not limited to the geometry, but, also, refers to its motion. It must be ensured that the object moves only in the vertical direction, due to force imposed by the linear motor. In other words, the object should not be susceptible to lateral hydrodynamic loading that can make it vibrate as a pendulum. It must be kept in mind, that the object moves in limited water and both radiated and reflected waves are expected to coexist. Edges, that would create additional vortices, and flat surfaces perpendicular to the horizontal plane should be avoided. On the other hand, the purpose of this component is to create a disturbance in the fluid field and drive it towards the flexible structure. Therefore, it should not have hydrodynamic shape at its tip. Using all the aforementioned points, the moving

object is designed to have a cylindrical shape with smaller (but comparable) radius with respect to characteristic dimensions of the flexible bottom (Fig. 4.1).

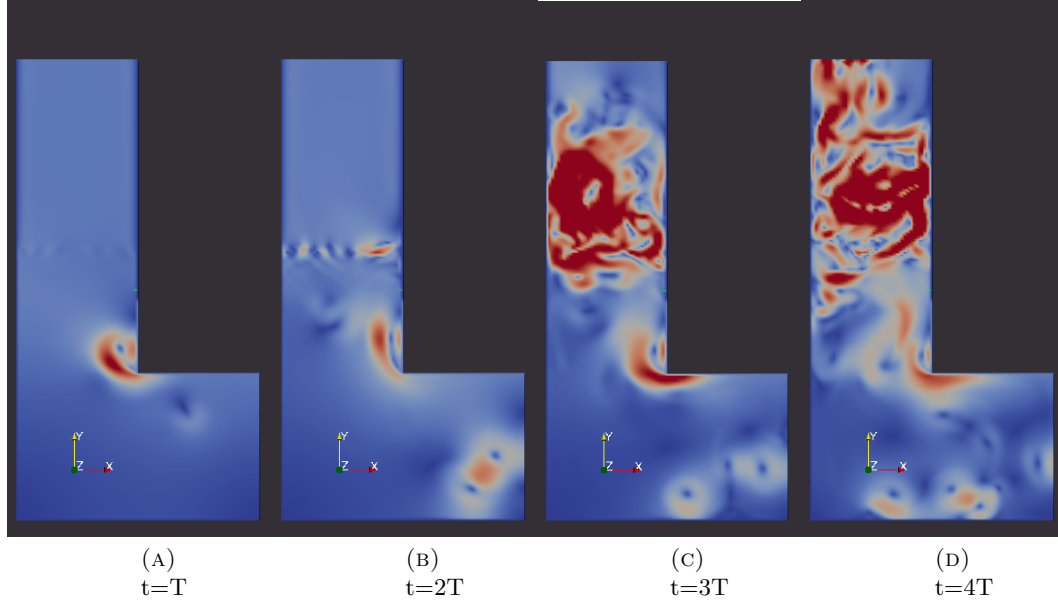


FIGURE 4.2: Illustration of fluid velocity in a fully rigid water tank, partly filled with water with a periodically moving object represented by moving boundaries, using *foam-extend 3.1* (Rizos, 2016)

### 3. Side walls

The design of this component is not limited by any special requirements apart from the obvious constrain of watertight splice with the bottom plates, through the bolted connection at the flange (Fig. 4.1). However, it is preferable for the side walls to be transparent so that water free surface and even bottom's deformation can be observable by naked eye.

Having determined the shape of the experimental arrangement, defining the dimensions of each component is what follows. The key feature for this process, is the definition of required dimensions of the bottom's flexible part. The dimensioning of the bottom plate involves the aspects of flexibility and structural integrity. The former would determine the achieved level of FSI while the latter can turn out to be questionable due to the significant amount of water inside the water container. Both aspects are affected by the same parameters (dimensions and material properties) but the resulting effects are contradicting.

#### 1. Flexibility

The response of the bottom plate is affected by its flexibility and the imposed excitation. In order to achieve responses of significant amplitude, the excitation and the flexibility should be related by means of frequency. More specifically, the frequency of vertical periodic motion imposed to the rigid cylinder is directly related to the frequency of resulting excitation that reaches the plate through the fluid's velocity field. One way to ensure that considerable responses is to apply oscillations of frequency that is close to the natural frequencies of the flexible plate (Fig. 4.3).



In the literature there are formulas only for the "dry" natural frequencies of plates. The general expression of the "dry" natural frequency is described by the following formula.

$$f_n = \frac{\lambda^2}{2\pi (d_{char})^2} \sqrt{\frac{D}{m_{st}}} \quad (4.1)$$

Where,

$\lambda$  is a coefficient dependent to the geometry  
 $d_{char}$  is a plate's characteristic dimension  
 $D = \frac{Eh_s^3}{12(1-\nu^2)}$  is the plate's stiffness coefficient  
 $m_{st}$  is the plate's structural mass per unit area and

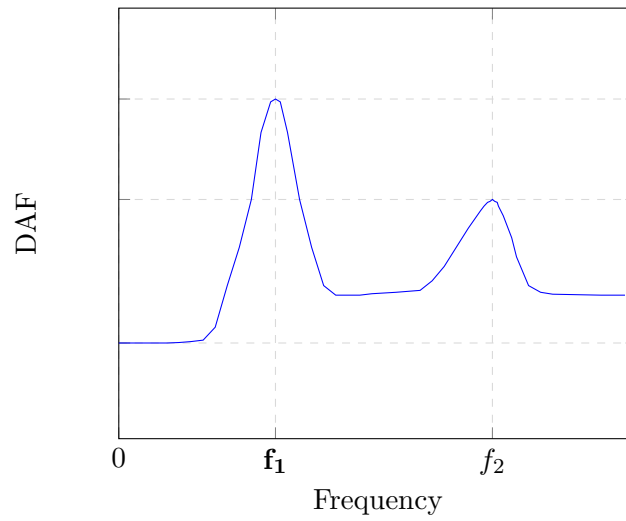


FIGURE 4.3: Qualitative graph of dynamic amplification factor for a multi-degrees of freedom system

	HDPE	PTFE	LDPE
Density [ $kg/m^3$ ]	940 - 965	2150 - 2200	910 - 928
Young's Modulus [ $MPa$ ]	600 - 1400	410 - 750	200 - 400
Tensile Strength [ $MPa$ ]	20 - 32	25 - 36	8 - 12
Poisson Ratio	0.42	0.46	0.42

TABLE 4.1: Mechanical properties of tested materials (source: Idemat 2003, available at <https://www.matbase.com>)

A rough estimation of the "wet" natural frequencies can be achieved by modifying the mass term in the formulas of the "dry" ones. In this modification, the mass per unit area of the water column above the plate is added to the actual mass per unit area of the plate. The height of the water column is equal to the water level inside the tank without the moving object(Fig. 4.4).

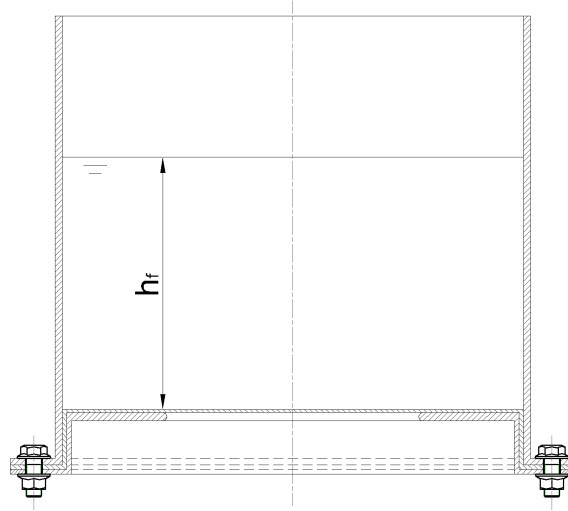
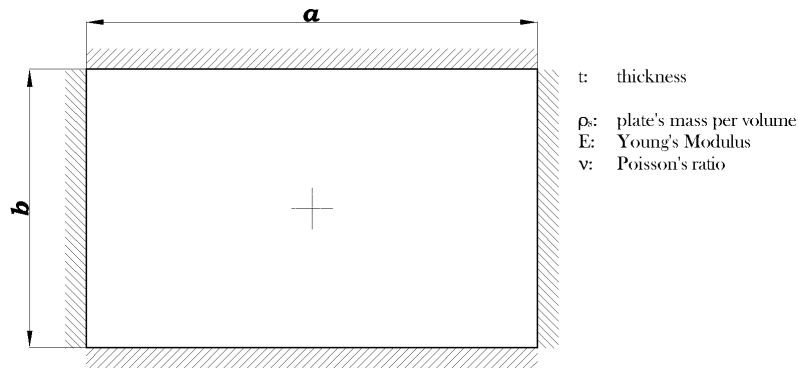


FIGURE 4.4: The height of the water column  $h_f$  refers to the empty tank

(a) **Rectangular Plate**



- "Dry" Natural Frequency (Leissa, 1969)

$$f_n = \frac{\lambda^2}{2\pi b^2} \sqrt{\frac{Et^3}{12(1-\nu^2)\rho_s t}} \quad (4.2)$$

- Estimated "Wet" Natural Frequency

$$f_n = \frac{\lambda^2}{2\pi b^2} \sqrt{\frac{Et^3}{12(1-\nu^2)(\rho_s t + \rho_f h_f)}} \quad (4.3)$$

Values of  $\lambda$  are dependent to length per width ratio (Table 4.2)

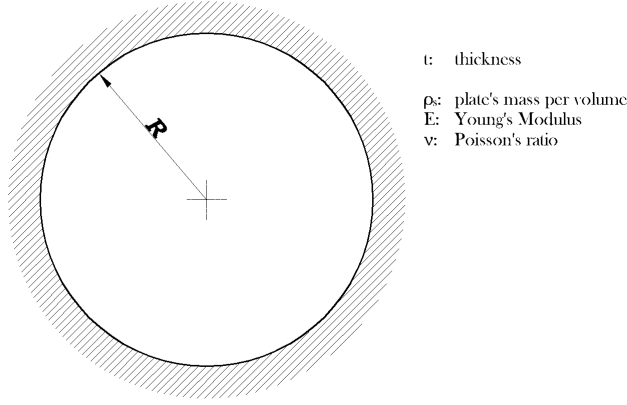
a/b	1.5	2	2.5	3	$\infty$
$\lambda$	27.00	24.56	23.76	23.19	22.37

TABLE 4.2: Values of  $\lambda$  obtained by Iguchi(Leissa, 1969)

The values of  $\lambda$  presented in Table 4.2 can be approximated by:

$$\lambda = -1.88 \left(\frac{a}{b}\right)^3 + 14.56 \left(\frac{a}{b}\right)^2 - 38.45 \left(\frac{a}{b}\right) + 58.26$$

(b) **Circular Plate**



- "Dry" Natural Frequency (Leissa, 1969)

$$f_n = \frac{\lambda_{nk}^2}{2\pi R^2} \sqrt{\frac{Et^3}{12(1-\nu^2)\rho_s t}} \quad (4.4)$$

$\lambda_{nk}$  are the dimensionless natural frequencies. Their values for n (angular nodes) and k (radial nodes) are given in Table 4.3. For fixed boundaries,  $\lambda_{nk}$  is not dependent to the Poisson's ratio.

- Estimated "Wet" Natural Frequency

The wet natural frequencies of the circular plates were calculated based on the same logic as for the rectangular plates.

$$f_n = \frac{\lambda_{nk}^2}{2\pi R^2} \sqrt{\frac{Et^3}{12(1-\nu^2)(\rho_s t + \rho_f h_f)}} \quad (4.5)$$

k	n = 0	n = 1	n = 2	n = 3
1	10.2158	21.2609	34.8770	51.0334
2	39.7711	60.8287	84.5837	111.0214
3	89.1041	120.0792	153.8151	190.3038
4	158.1842	199.0534	242.7285	28901799

TABLE 4.3: Values of  $\lambda_{nk}^2$  for different combinations of modes (Leissa, 1969)

## 2. Strength

The bottom plate of the water container has to withstand a significant amount of water. Its deflections would be measured with optical measures from beneath. Apparently, any scenario of failure that would lead to leakage has to be eliminated. For this reason, strength criteria were set, that relate the hydrostatic pressure at the bottom and the plate's strength. Apart from that, the expected deflections should remain within the elastic region of the selected material. These deflections would have a static component due to hydrostatic

pressure and a dynamic due to the excitation, but, only, the former one is to be predicted at this initial stage.

(a) **Maximum stress due to uniform static load**

The maximum bending moments and, therefore, maximum stress at a plate with fixed edges occur at the short span boundaries. For **rectangular** plates, the stress at these edges is calculated according to the following formula (Westergaard H.M., 1921).

$$\sigma_{e,max} = \frac{\rho_w h_w b^2}{2 \left(1 + (b/a)^4\right) t^2} \quad (4.6)$$

As in the case of rectangular plates, for fully clamped **circular** plates, the maximum stress occur at the boundaries (Timoshenko S., 1989):

$$\sigma_{c,max} = \frac{3 \rho_w h_w R^2}{4 t^2} \quad (4.7)$$

(b) **Maximum static deflection**

Another measure of structural integrity of the plate can be the static deflection of the plate. The static deflections of the plate compared to its characteristic dimensions should remain at very low levels because, otherwise, the induced pretension would dominate the resulting response. The deflection at the centre of the plate is calculated as follows (Westergaard H.M., 1921):

$$w_{max} = \frac{0.032}{1 + (b/a)^4} \left[ \frac{\rho_w h_w b^4 (1 - \nu^2)}{Et^3} \right] \quad (4.8)$$

For a circular plate, the static deflection is determined with the following formula (Timoshenko S., 1989).

$$w_{max} = \frac{3 \rho_w h_w R^4 (1 - \nu^2)}{16 Et^3} \quad (4.9)$$

### Conclusive remark for the first approach

A series of preliminary calculations was conducted for different values of dimensions, water height and different plate materials (listed in Table 4.1). The results revealed that designs which satisfied the strength criteria lead to high values of natural frequencies. Then, the required oscillation frequencies would be impractical to apply. On the contrary, designs with reasonable values of natural frequencies lead to large static deflection, rising the possibility of creep or excessive pretension that would restrain the amplitude of response. Finally, it has already mentioned that free surface effects

### 4.3.2 2nd approach: base excitation of the flexible plate

#### Description

The aforementioned flaws of the first approach revealed the need to search for alternative solutions. At least one of the requirements of either strength or high inherent flexibility should be removed from the designing considerations. The major flaw of

the first approach derived from the effect of hydrostatic pressure that acts on the flexible plate.

To eliminate this unfavourable effect, the flexible structure should be positioned inside the water domain. Being surrounded by water, the largest part of loads acting on different parts of the structure, due to hydrostatic pressure, would counteract each other. But still, the issues of boundary conditions and the required oscillation need to be addressed.

Keeping into account that the main objective is to design an experimental arrangement of reduced complexity, both the aforementioned issues were dealt with the addition of a rigid structure. This structure would not only keep the plate's edges clamped, but it would, also, oscillate the flexible plate. To achieve that, the flexible plate would be a part of an otherwise rigid structure that is moving periodically in the vertical direction.

More specifically, this rigid structure is a hollow plunger consisting of a outer shell and an inner hollow cylinder. At the bottom of the plunger the flexible plate is positioned between the shell and the hollow cylinder. This way the plate's boundaries remain fixed. The whole assembly is placed inside a container partly filled with water. Two tiny holes, drilled at the circumference of the plunger assembly, let the water enter the interior ensuring that the water level inside the plunger is the same as its draft. In this way, the unfavourable effects of hydrostatic pressure acting on the plate are eliminated. The plunger is attached to an oscillator that imposes a sinusoidal vertical motion. This means that the excitation is imposed directly to the edges of the flexible structure (base excitation). As already mentioned, the resulting plate's deflections have to be measured by means of optical methods and, therefore, the water container must be fully transparent.

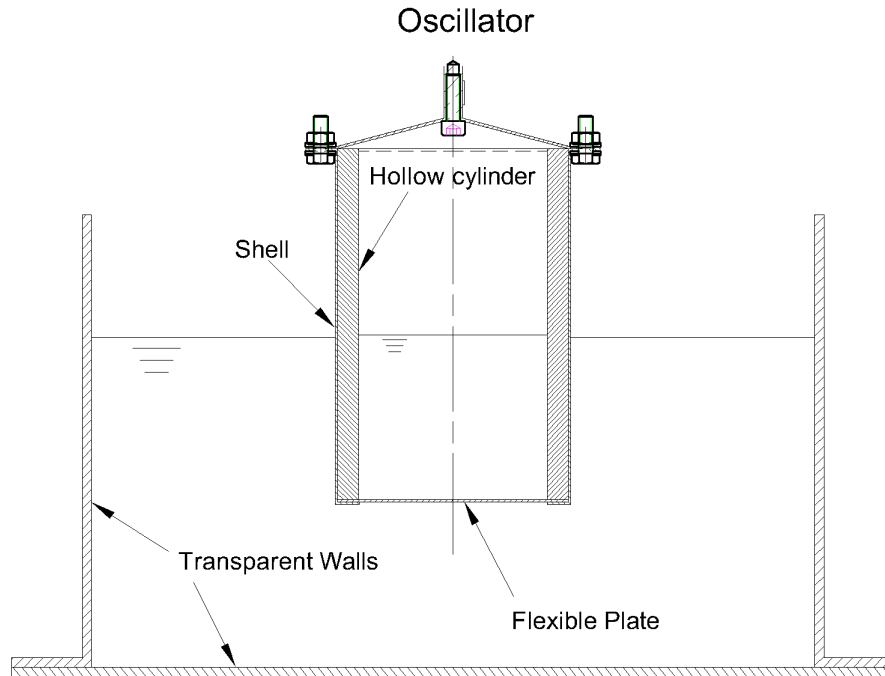


FIGURE 4.5: Preliminary sketch of the 2nd approach

### Conclusive remark for the second approach

The need to formulate a second approach was caused due to the aforementioned weaknesses of the first one. Apparently, any modifications made were focusing to the elimination of these weaknesses and, therefore, any comparison between the alternatives would have the second as winner. Having the flexible plate fully submerged, the effect of hydrostatic pressure around the plate is minimized. This means that more slender and, therefore, more flexible plates can be used. Additionally, the excitation is imposed directly to the plate and not through a disturbance at the fluid field. This raises the possibility to end up with significant measured deflections. Consequently, it is not longer necessary to correlate the natural frequencies of the plate with the oscillation frequency. Thus, the dimensions of the plate will be determined by rather practical reasons such as the operational limits of optical instruments that are to be used.

## 4.4 Detailed design of the experimental set-up

Having established the a preliminary design for the experimental set up, detailed designing is what follows. The following paragraphs includes in-depth descriptions for all components (e.g. measuring instruments, structures, additional equipment, etc.) of which the final setup would consist.

### 4.4.1 Measuring instruments

In this paragraph, the required measuring instruments are described in detail. For each instrument, the description includes its purpose for the particular application, the operating principle and the technical characteristics of the particular model used.

#### 1. 3-D Digital image correlation system

##### Purpose

As already discussed, the vibrations of the plate need to be measured with optical methods. Image correlation techniques are being used in order to determine the deformation of an object, for almost two decades. It is capable of measuring in-plane (2-D DIC) and/or out-plane (3-D DIC) motion of million points on the target surface. It is placed beneath the water container to measure the deflections at the plunger's bottom. After subtracting the rigid body motion (RBM) of the plunger, the out-plane motion of the flexible plate, obtained by image correlation, will give a full description of the plate's vibrational mode shapes.

##### Measuring principle

During the process of digital image correlation, the surface of a deformable object is discretized to a large number of overlapping facet elements with size of 10 - 20 pixels. Generally, for in- and out- of plane deformations at least two charge-coupled device (CCD) cameras are required. The cameras of a DIC system bear an array of pixels/cells, each of which can store a value from 0 to 255 which is the gray-scale colour map range (Helfrick et al., 2011). Typically, 0 represents black and 255 represents white colour. As it may seems obvious,

the stored value depends on the intensity of light that is reflected off the measured surface. For this reason, the most common practise followed, is that the object's surface is covered with a mat-white paint and, then, a stochastic pattern of black speckles is applied. The speckle size depends on the size of the measured area, but, in any case, all speckles must be of smaller size than the facets. In this way, a high contrast gray-scale image is created which is ideal for the correlation process.

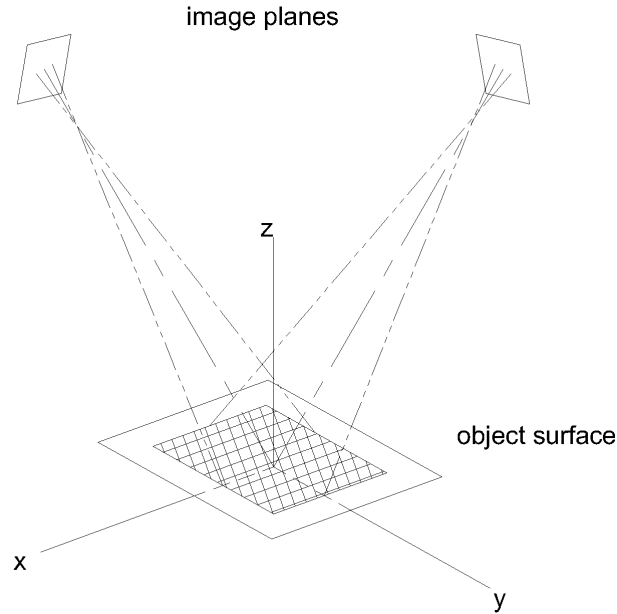


FIGURE 4.6: 3D digital image correlation configuration

The correlation process involves an algorithm for the tracking of the gray-scale pattern. Images taken by a camera can determine the motion of all points on the plane parallel to the pixel array (Fig. 4.7). Since, two cameras are pointing to the surface from different directions, the 3-dimensional coordinates of any point of the surface (in other words, the 3D contour) can be determined (Herbst and Splitthof). All images, taken by the cameras, are compared to a reference image. The deformations are calculated using the translation and rotation of each facet with respect to their position at the reference frame.

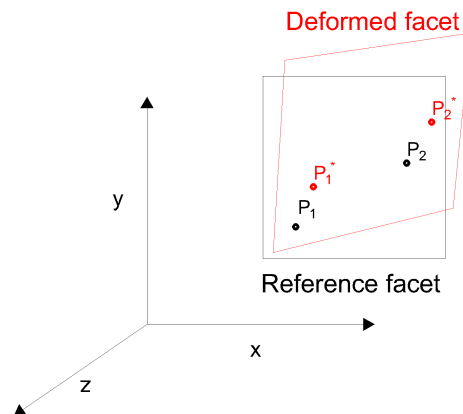


FIGURE 4.7: Reference and deformed facet

Before any test is conducted, all imaging parameters, such as the relative distance and angle between the two cameras and between the cameras and the object should be defined. This is done through a calibration measurement, during which several images of a reference plate that bears a black and white (dot or chequerboard) pattern are taken.

### Technical characteristics

The available 3-D DIC system consists of the following components:

- (a) **Two cameras** with resolution of  $2452 \times 2054$  pixels each of them bears CCD pixel arrays of  $8.46 \times 7.08\text{mm}$  size. Consequently the pixel size is of  $3.45\mu\text{m}$ . At full resolution, the sampling frequency can reach the value of 15 frames per second. However, the measurement speed can be adjusted by adjusting, also, the resolution of the obtained images. The maximum possible sampling frequency is 30 frames per second and the corresponding resolution is  $2452 \times 222$  pixels.
- (b) The set of cameras is accompanied with **two fixed focus lenses**, with focal length of  $75\text{mm}$ . The achievable focus depth varies between  $20\text{mm}$  and  $50\text{mm}$  and depends on the illumination and the clarity of the medium. The achievable field of view (FOV) depends on the focal length ( $f$ ), CCD sensor width ( $SW$ ) and the working distance ( $WD$ ). According to the supplier company (LIMESS Messtechnik & Software GmbH) the relation is the following:

$$FOV = SW \times \frac{WD - f}{f} \quad (4.10)$$

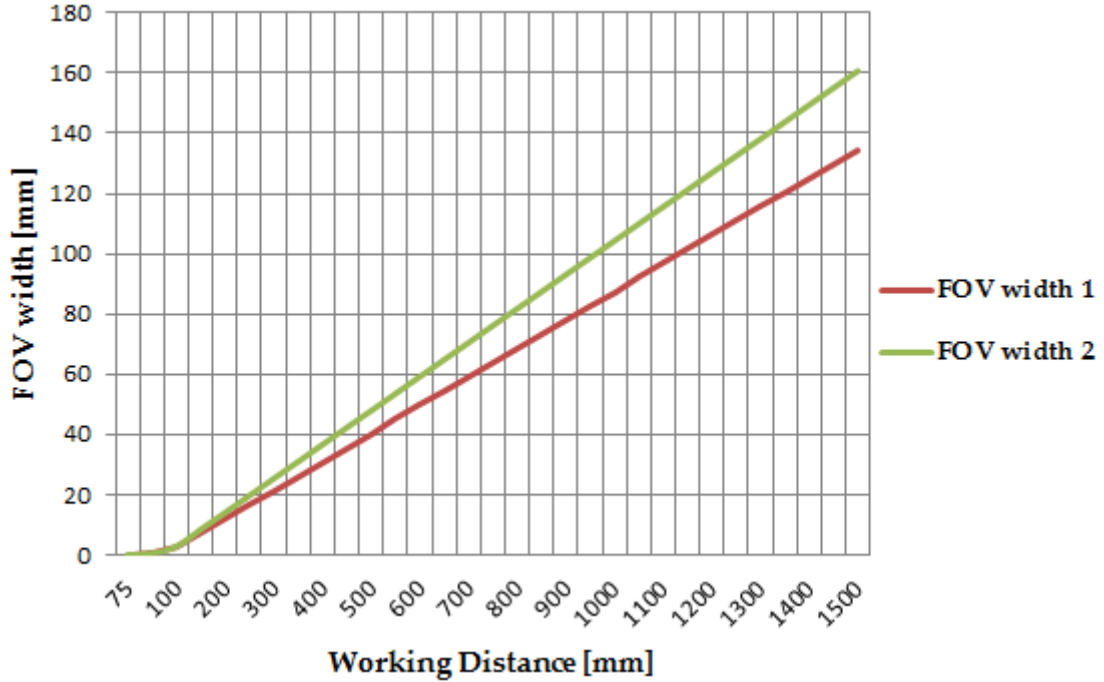


FIGURE 4.8: DIC cameras FOV width versus working distance



- (c) **Post-processing software** that is capable of three dimensional deformation and motion analysis as this was described in the paragraph referring to the measuring principle of image correlation. It is capable of processing images of many million data points. The analysis time, using the provided computer unit (Dual-core 2 GHz CPU), is, typically, less than 1 second per image. Data that can be directly displayed, are:

- 3D coordinates
- 3D displacements (with or without RBM)
- Surface strains

For displacements, resolution of 0.01 pixel can be achieved. With respect to strains, the achievable resolution is about 0.01% or even higher.

- (d) **Data Acquisition (DAQ)** system (hard- and software) that is able to record up to 8 analogue signals of  $\pm 10V$  and 16bit precision, simultaneously. Transfer functions can be applied to all signals. The acquisition process can be triggered either by an internal clock or by an external transistor-transistor logic (TTL) signal.

## 2. Single point laser Doppler vibrometer (LDV)

### Purpose

The purpose of using a second optical instrument for the plate's vibration measurement lies with the difference in its technical characteristics. More specifically, single point LDVs can measure the velocity of a vibrating point with great sampling frequency ( $\sim kHz$ ). Therefore, it can provide data for responses of higher frequency.

### Measuring principle

The operating principle of LDVs is based on optical interference. Velocity and displacement of a vibrating object are measured by determining the frequency and phase difference of two laser beams. One of them is a reference beam, which does not come out from the sensor head so that its path remain constant and  $I_1$  is its light intensity. The second beam, typically named 'object beam', is driven towards the surface of an object in the direction of the velocity and displacement of interest. Part of the object beam is reflected back to the sensor with intensity  $I_2$ , where it is made to coincide with the reference beam, creating a fringe pattern. The fringe passes through a photo detector, where it is converted to the output electrical signal. The intensity  $I$  of the resulting fringe is a function of the phase difference  $\Delta\phi$  between the reference and the object beam:

$$I(\Delta\phi(t)) = I_1 + I_2 + 2\sqrt{I_1 I_2} \cdot \cos \Delta\phi(t) \quad (4.11)$$

Where, the phase difference  $\Delta\phi$  is determined by the ratio of the path difference  $\Delta l$  to the laser wavelength  $\lambda$ :

$$\Delta\phi(t) = 2\pi \frac{\Delta l(t)}{\lambda} \quad (4.12)$$

Apart from the magnitude of displacement, the direction is, also, defined with directionally sensitive counting of the laser fringe. The velocity at the direction of the object beam  $u(t)$ , is calculated using the time derivative of path difference:

$$u(t) = \frac{1}{2} \frac{dl(t)}{dt} \quad (4.13)$$

Due to the Doppler effect, the object laser beam experiences a frequency shift  $f_D$ , which is proportional to the object's velocity:

$$f_D = 2 \cdot \frac{u(t)}{\lambda} \quad (4.14)$$

When the object and the reference beams are superimposed, the photo detector receives a wave with a beat frequency, which coincides to the Doppler shift. However, this can only determine the magnitude of velocity. The sign of velocity can be defined with the introduction of a constant frequency shift, so that a reference velocity component is created. This frequency shift can be obtained with an optical modulator, known as Bragg cell, acting on one of the fringe components (e.g. reference beam). The Doppler frequency shift  $f_D$  is added to the constant frequency shift  $f_c$  and, therefore, the object's velocity can be fully described by the sign and the magnitude of the ultimate frequency shift with respect to  $f_c$ . Interferometers that are sensitive to the direction of the motion are known as heterodyne interferometers (Fig. 4.9).

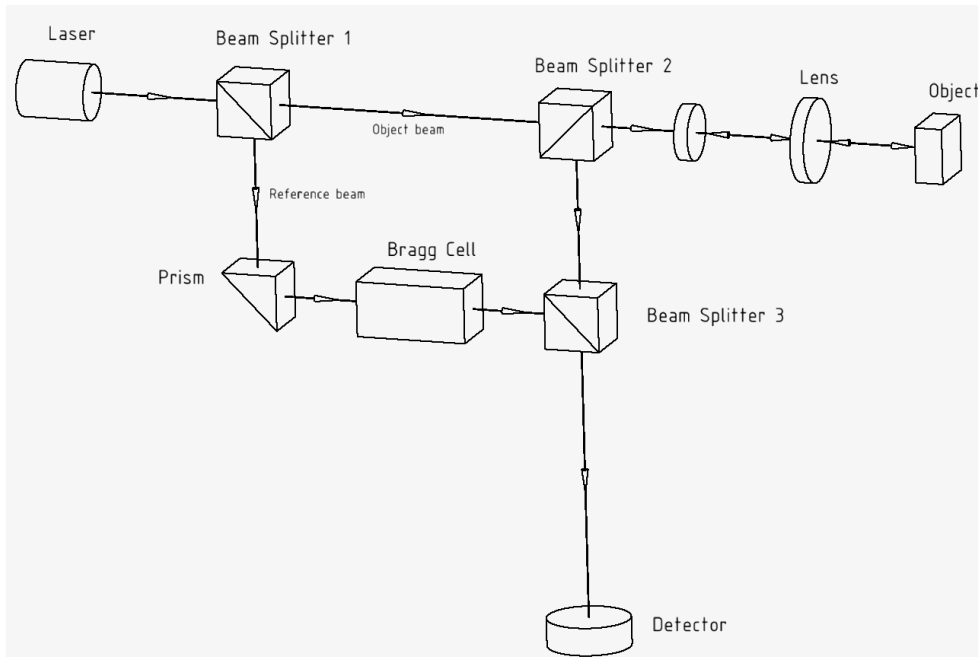


FIGURE 4.9: Schematic presentation of a heterodyne interferometer's configuration (reproduction from PolytecGmbH, 2003)

### Technical characteristics

The system of the single point LDV consists of two components: a laser head and a controller. The system had been manufactured by *Polytec GmbH* and was borrowed from the facilities of Precision and Microsystems Engineering (PME) department of TU Delft.

The **laser head (OFV - 505)** emits a Helium Neon (HeNe) laser beam of 633 nm, which means that is visible. The consequence is, unfortunately, that DIC is not expected to work at the surface covered by the laser spot. However, as it is shown in Fig. 4.10 the spot size is negligible. The laser beam is classified in *Class 2* and, therefore, its use does not require special health and safety (H&S) measures. The sensor head is supplied with a mid-range front lens with of 60 mm focal length and 200 mm minimum stand-off distance. The length of laser cavity for the particular model is 204 mm. According to PolytecGmbH, 2003, the intensity of received optical signal increases to a maximum, when the optical path difference  $\Delta L$  (see measuring principle) is a multiple. As a result, for OFV - 505 the optimal stand-off distances (*OSD*) in *mm* are given by the following formula (PolytecGmbH, 2003).

$$OSD = 234 + n \cdot l \quad (4.15)$$

Where,  $n = 0; 1; 2; \dots$  and  $l = 204 \pm 1$  mm is the laser cavity length.

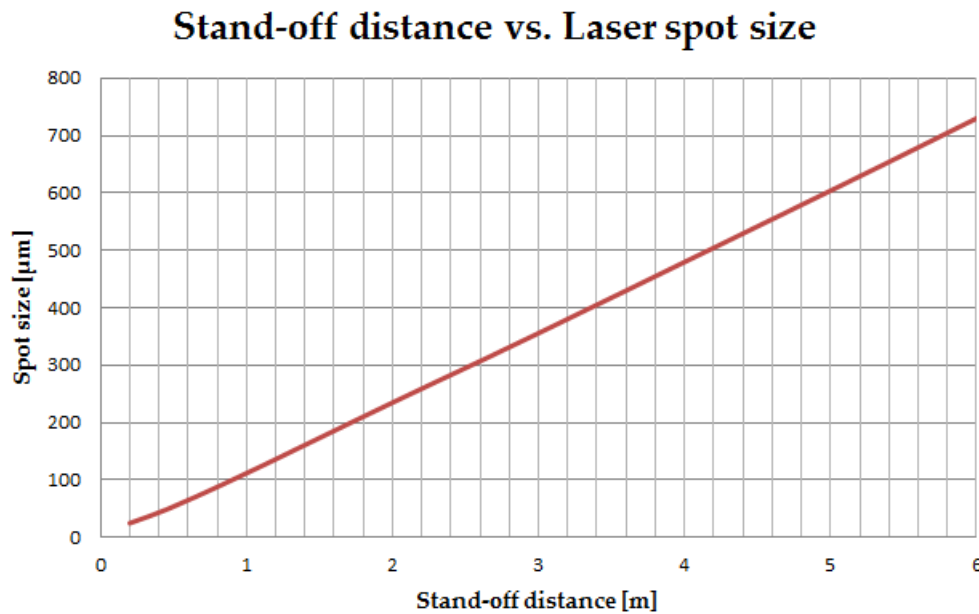


FIGURE 4.10: Laser spot size vs. stand-off distance for OFV-505 with mid-range lens

The technical data of OFV - 505 are summarized at Table 4.4

The **controller OFV - 2200** receives the signal from the sensor head and decodes it to an analogue voltage signal that is proportional to the vibration velocity. The most important technical specifications of the controller are shown at Table 4.5.

### 3. Triangulation laser displacement measurer

#### Purpose

The motion of the vibrating plate consists of two components: the vibration and the rigid body motion imposed by the oscillator. In order to monitor the latter component, a laser triangulation sensor is used to measure the motion

**OFV-505 Specifications**

Laser Type	Helium Neon (HeNe)
Laser class	Class 2 (eye safe)
Laser wavelength	633 nm
Focus	Auto or manual focus
Operating temperature	+5°C ... +40°C
Relative humidity	Max. 80%, non-condensing
Weight	3.4 kg
Dimensions [W×H×L]	120 × 80 × 345 mm
Lens Type	mid-range
Focal length	60 mm
Min. stand-off distance	200 mm
Aperture diameter	6.8 mm

TABLE 4.4: LDV sensor head OFV-505 technical data

**OFV-2200 Specifications**

Operating temperature	+5°C ... +40°C
Storage temperature	−5°C ... +60°C
Relative humidity	Max. 80%, non-condensing
Weight	10.5 kg
Dimensions	450 × 360 × 135 mm
Protection class	I (protective grounding)
Velocity decoder range (max.)	125 mm/s/V
Resolution at max. range	5 μm/s
Max. vibration freq.	250 kHz
Max. Acceleration	200000 g
Voltage output	±10 V
Output impedance	50 Ω

TABLE 4.5: LDV controller OFV-2200 technical data

of a rigid part of the plunger. However, it is not advisable to use triangulation sensors in transparent mediums other than air (Berkovic and Shafir, 2012). For this reason, the triangulation measurer is placed above the plunger with its laser beam pointing at the upper part that is not expected to immerse.

**Measuring principle**

Optical triangulation is based on the principal of similar triangles. A laser beam travels from the sensor's laser source to the object of which the position or displacement is to be measured. An optic lens is placed beside the laser source in perpendicular to the incident laser beam direction. Rear of the optic lens there is an array of pixel detectors. In the general case, the object's surface induces diffusive reflection of the incident laser beam. As shown in Fig. 4.11, a reflected laser beam splits into two parts as it passes through the optic lens. The arising laser beams are captured by the line detector. The position of the object, as shown in Fig. 4.11, is determined by the distance between the pixels

on which the laser beams impact, using the triangles similarity:

$$Position = AB = AC \cdot \frac{CE}{DE} \quad (4.16)$$

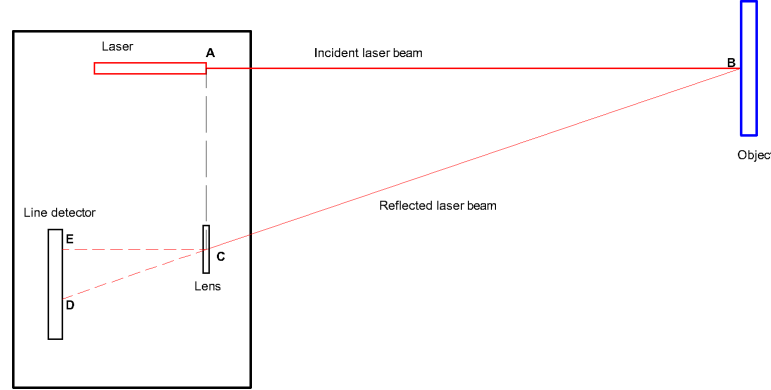


FIGURE 4.11: Schematic presentation of optical triangulation operating principle

The size of pixel array influences the measuring range of the sensor. Due to the geometry of the aforementioned configuration, apart from an upper limit, there is, also, a lower limit for the measurable distance (Berkovic and Shafir, 2012). The sensors available in the industry are capable to measure distances from 10 up to 1000 mm (Chen, Brown, and Song, 2000). Accuracy of up to several micrometers can be obtained, but it can be deteriorated for larger distances. With respect to temporal resolution, hundreds of  $kHz$  can be achieved.

### Technical characteristics

The triangulation sensor used for the current experiments, is manufactured by *Micro-Epsilon Messtechnik* and borrowed from the measurement shop of *Mechanical, Maritime and Materials Engineering* faculty of TU Delft. The technical specifications of the sensor used, are shown at Table 4.6.

## 4. Force Transducer

### Purpose

The applied force from the linear oscillator to the plunger is monitored with a force transducer that is installed with a bolted connection between the oscillator's shaft and the plunger. Apart from monitoring, the output of the load cell can offer validation data to a FSI solver, given the fact that installing pressure gauges inside the water container would create non-favourable disruptions of the fluid field. The plunger experience hydrodynamic loading which can be calculated numerically by integrating the pressures acting at the wetted surfaces. The result of the pressure integration can be compared to the output of the force transducer.

**ILD 1401-200 Specifications**

Laser type	Semiconductor laser
Laser class	Class 2 (eye safe)
Laser wavelength	670 <i>nm</i>
Measuring range	200 <i>mm</i>
Minimum stand-off distance	60 <i>mm</i>
Resolution (static)	20 $\mu m$
Resolution (dynamic)	100 $\mu m$
Measuring rate	1 <i>kHz</i>
Spot diameter	2100 $\mu m$
Operating temperature	0°C ... +55°C
Storage temperature	−20°C ... +70°C
Weight	100 <i>g</i>
Dimensions	65 × 50 × 20 <i>mm</i>
Voltage output (analogue)	1 ... 5 <i>V</i>

TABLE 4.6: Triangulation laser displacement measurer Micro-Epsilon ILD 1401-200 technical data

### Measuring principle

Force transducers are measuring instruments that can convert tensile and/or compression force to electrical signal. Their arrangement consists of strain gauges circuits tightly bonded to a spring material. Typically, strain gauges are thin, grid-shaped metallic foils laminated with thin plastic sheets. The working principle of a strain gauge is based on the property of metallic objects to change their electrical resistance when they experience elongation or contraction. When external loads are applied to the transducer, the metallic foils is deformed and, therefore, its electrical resistance changes.

To measure the change of resistance, the arrangement of Wheastone bridge is employed. Bridge circuits, typically, consist of two legs connected in parallel. Both legs bear two resistors, one of which is of known value. In one leg, there is a variable, but calibrated resistor. In the other leg, the second resistor is the one to be measured. The legs are connected with a galvanometer, as shown in Fig. 4.12 .

In order to determine the value of the unknown resistor, the galvanometer must read zero. For this reason the variable resistor is adjusted accordingly. When the bridge is balanced, the ratios between the resistance values of the same leg are equal:

$$\frac{R_x}{R_A} = \frac{R_{var}}{R_B} \Rightarrow R_x = R_A \cdot \frac{R_{var}}{R_B} \quad (4.17)$$

The relation between the ratio of the strain-initiated change of resistance  $\Delta R_x$  to the reference resistance  $R_x$  and the strain  $\varepsilon$  is linear:

$$\frac{\Delta R}{R} = GF \cdot \varepsilon \quad (4.18)$$

Where,  $GF$  is the gauge factor that represents the sensor's sensitivity.

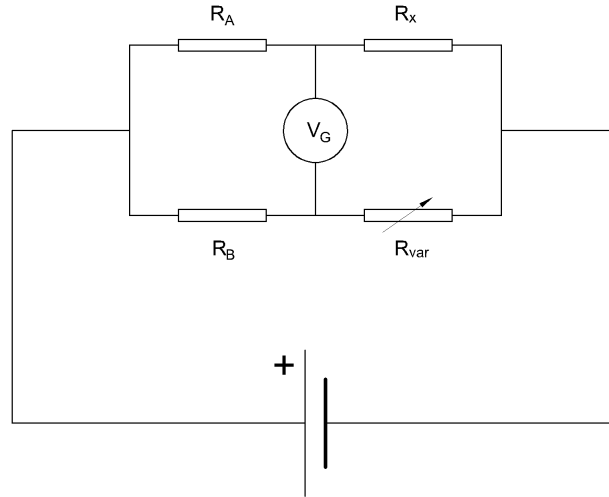


FIGURE 4.12: Schematic presentation of Wheatstone bridge

Obviously, in the bridge shown in Fig. 4.12, resistor  $R_x$  represents the strain gauge. However, depending on the application, more complicated configurations can be required. 2-gauge or 4-gauge systems are more preferable when temperature compensation and/or isolation of only the target strain are of utmost importance. For temperature compensation, 2-gauge systems are used, with one active and one dummy gauge. For the elimination of other strain components, 2-gauge systems with two active strain gauges are used. 4-gauge systems are used when both requirements must be met and large strains are expected.

### Technical characteristics

The required measurement range was determined by estimating the hydrodynamic force that the plunger will experience (Appendix A). The range of force with respect to the oscillation characteristics (frequency and amplitude) that are to be examined, are shown in Figure 4.13

The graph at Figure 4.13, reveals that the load cell should be able to measure both tension and compression loads and the measuring range should be at least  $\pm 100 \text{ N}$ . Specifications of the purchased sensor are shown at Table 4.7

Load Cell Specifications	
Measuring range	$\pm 250 \text{ N}$
Safe overload	150 %
Ultimate overload	300 %
Principal dimensions	$50.8 \times 76.2 \times 14.5 \text{ mm}$
Recommended torque on fixation	$25 \text{ Nm}$
Material	Nickel plated alloy steel

TABLE 4.7: Load Cell technical data

### 4.4.2 Fabricated structures

1. **Transparent water container** of circular shape made of PMMA. The dimensions of the water container are shown at the sketch of its cross section

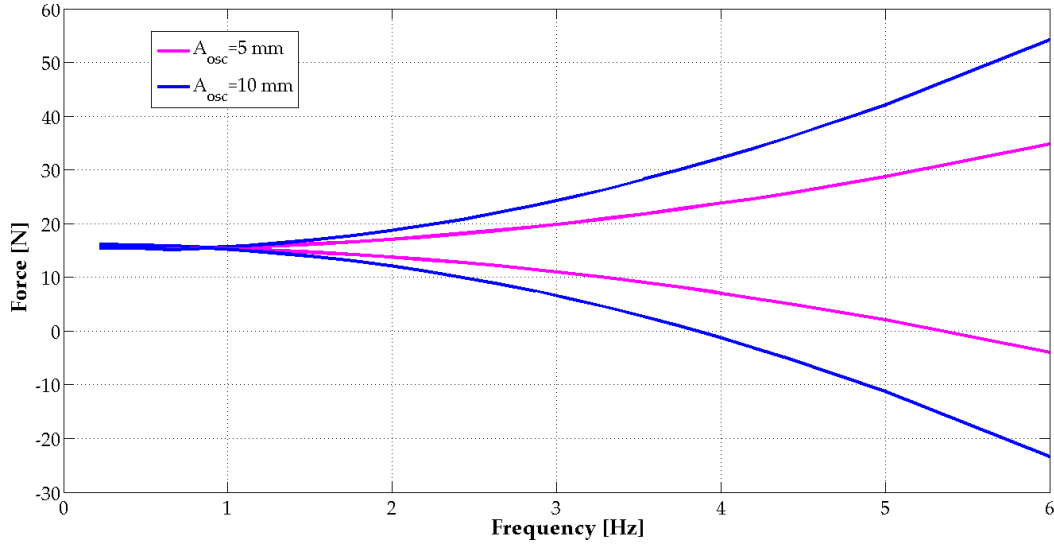


FIGURE 4.13: Graph with the pre-estimated range of forces applied to the plunger for  $A_{osc} = 0.5, 1 \text{ cm}$  and  $f_{osc} \in [0, 6]$ , case: "Deep"

(Fig. 4.14). The water level inside the container is constantly set equal to 150 mm.

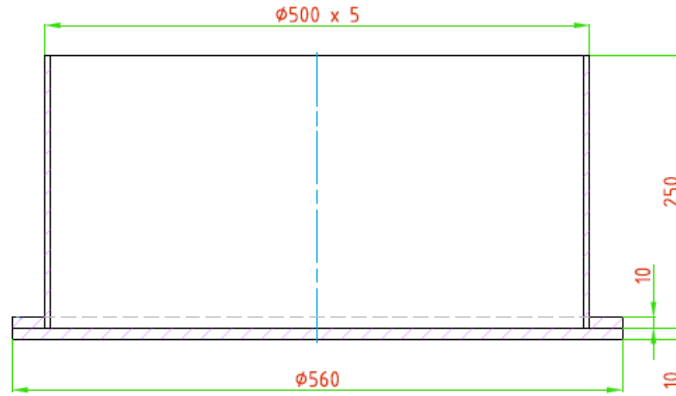


FIGURE 4.14: Cross section of the water container

2. **Plunger** of a hollow cylindrical shape with flexible bottom plate. The plunger has a shell made of steel with a circular slot at its lower tip. Inside the shell there is a hollow PVC cylinder. Between the lower tip of the cylinder and the steel shell a PTFE sheet is placed with thickness of 0.5 or 0.25 mm. The cylinder and the PTFE sheet will be pushed towards the notched bottom of shell through an annular lid bolted at the upper flange of the shell. The bolted connections consists of 8 M5 bolts, that will apply a uniformly distributed load to the PVC cylinder and then to the plate's edges. In this way the fully clamped boundary condition will be obtained. In order to ensure that before each test start, the water level inside the plunger is equal to its draft, two very small holes ( $\varnothing 2 \text{ mm}$ ) are drilled at the shell and the PVC cylinder. A socket screw placed closer to the upper flange of the shell will keep the holes aligned.



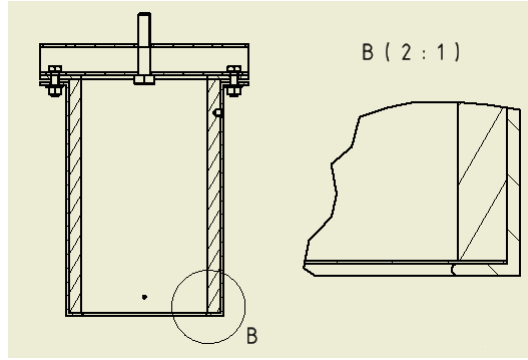
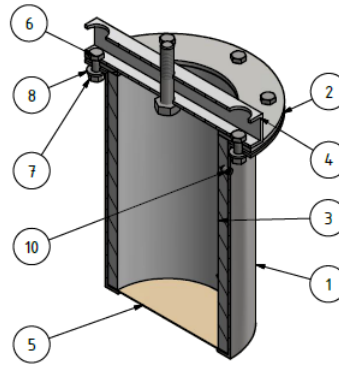


FIGURE 4.15: Clamped boundaries of the PTFE bottom plate in enlarged view

An aluminium beam of hollow square cross section is attached to the annular lid with the same bolted connection. Through this beam the plunger will be connected to the oscillator. (see fig. 4.16). As far as the dimensions are concerned, the outer diameter of the plunger is  $104\text{mm}$  and its overall height is  $157\text{mm}$ . The circular slot's diameter, that corresponds to the diameter of the bottom's flexible part, is  $80\text{mm}$ .



PARTS LIST				
ITEM	QTY	PART NUMBER		DESCRIPTION
1	1	FSI_03		Steel Plunger Shell
2	1	FSI_04		Steel Annular Lid
3	1	FSI_05		PVC Hollow Cylinder
4	1	FSI_06		Aluminium Connection Beam
5	1	FSI_07		PTFE Sheet
6	8	ANSI B18.2.3.1M - M5 x 0,8 x 16		Metric Hex Cap Screw
7	8	ANSI B 18.2.4.1 M - M5 x 0,8		Hex Nut
8	8	ANSI B18.22M - 5 N		Metric Plain Washers
9	1	ANSI B18.2.3.5M - M8 x 1,25 x 40		Hex Bolt
10	1	ANSI B18.3.6M - M4x0,7 x 6		Broached Hexagon Socket Set Screw - Cone Point

FIGURE 4.16: 3D drawing of the plunger assembly with parts list

3. **Wooden base:** The purpose of this structure is to offer a stable position to the water container when it is installed at the support structure. It bears transverse girders so that there will be no deflections at the bottom plate of the water container due to the hydrostatic pressure.

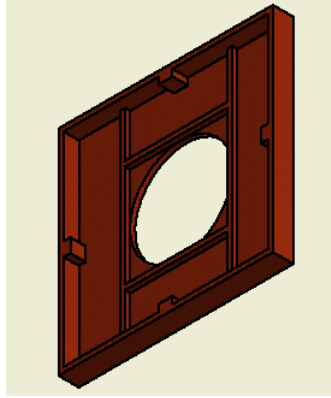


FIGURE 4.17: 3D drawing of the wooden base

4. **Support Structure:** Obviously, the components of the aforementioned arrangement need to be mounted to a stable support structure, of which the dimensions are determined by the required distances between the components (optical instruments - plunger and plunger - oscillator). The support structure is an assembly of aluminium columns and braces. It consists of two parts: the main part and a superstructure. At the main part, the water container, the DIC cameras and the LDV will be installed. In addition, a wooden base for the water container is attached. The superstructure supports the assembly of the plunger and the linear oscillator, the laser displacement measurer and shaft bearing.

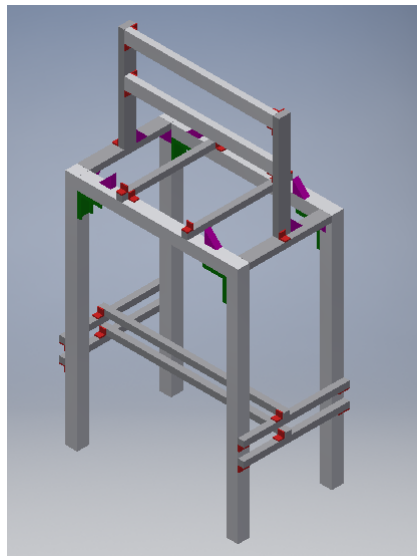


FIGURE 4.18: 3D drawing of the support structure

#### 4.4.3 Additional equipment

1. **Linear motor** The plunger is oscillated by a linear motor which is an electromagnetic direct drive in tubular form. The linear motor consists of the slider and the stator. The slider is made of neodymium magnets that are mounted in a high-precision stainless steel tube. The stator contains the motor windings, bearings for the slider, position capture sensors, and a microprocessor circuit

for monitoring the motor. The particular motor provided by LinMot© can impose a force of up to  $163N$  which are sufficient for our application.

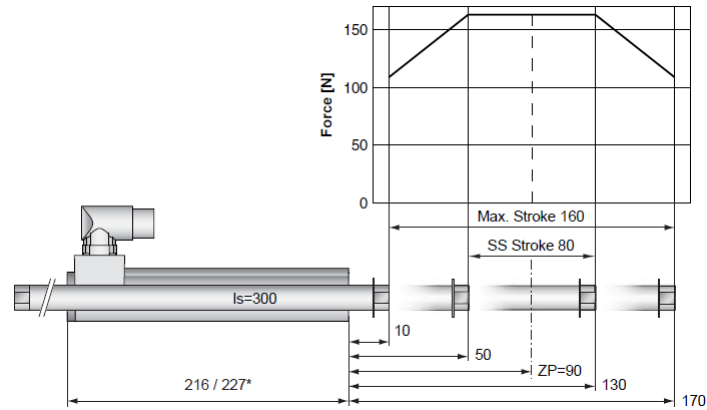


FIGURE 4.19: Force vs Position graph of LinMot P01-37x120/80x160 motor

Due to its operating principle it can offer great values of speed and accelerations. The exact values depend on the weight of the moving object, as it can be seen at the following graph obtained by LinMot© specification data sheet (Fig. 4.20).

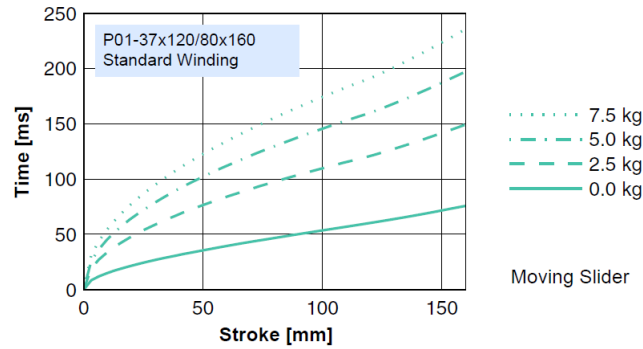


FIGURE 4.20: Position vs Time graph of LinMot P01-37x120/80x160 motor

2. **Shaft bearing.** When the plunger is imposed to harmonic motion, standing waves are expected to appear, especially when the harmonic motion has relatively higher frequencies. Due to these waves, the plunger can experience loading on the horizontal plane. Any displacement in a lateral direction will affect severely the vibration measurements and it will wear down the internal surface of the stator. For the aforementioned reasons, it was decided that a shaft bearing has to be installed to the superstructure, between the motor and the plunger, in order to restrain this unfavourable effect.
3. **Light sources.** As already mentioned, the performance of DIC cameras can be deteriorated when there is not enough ambient lighting. Therefore, it is necessary to place light sources around the water container.

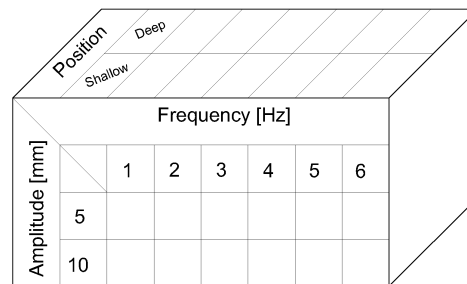
## 4.5 Experiments plan

Having the general arrangement designed and the required equipment defined, it is necessary to determine the experimental matrix. The experimental phase would consist of a series of forced vibration tests for both cases of PTFE plate's thickness (0.5 and 0.25 mm). With respect to the oscillation, which would have sinusoidal shape, the investigated parameters are the oscillation's frequency and amplitude. Regarding to frequency, all integer values from 1 to 6 Hz will be tested. Due to the limited sampling frequency of DIC cameras (max. 30 Hz), any larger value of oscillation frequency would lead to very rough descriptions of the displacements per cycle, even for the rigid body motion.

As far as the amplitude is concerned, two cases are to be tested: 5 mm and 10 mm. Due to the fact that the oscillation frequency range is more likely laid within the quasi static region of the plate's response, relatively large values of oscillation amplitude were selected. For any larger values of amplitude, the plunger's bottom plate may be driven outside the focus range of DIC.

Finally, two cases of submergence depth were selected. As already mentioned, it is favourable to involve free surface effects in the experiments. The reasoning behind the choice of these depth values, derives from some useful remarks obtained by the literature. To begin with, the most characteristic phenomena that require hydro-elastic analysis (slamming, ringing etc.) involve water's free surface. Additionally, modelling free surface effects is a key feature of the CFD solver that is to be validated (ComFLOW). Therefore, it was decided that a case where the plate is near to the free surface needs to be tested. However, the available optical instruments can not give reliable measurements, when the plate is transferred from air to water, due to the created bubbles. Therefore, the plate can not be placed too close to the surface, in order to eliminate the risk of emersion. Moreover, previous studies that conducted for the investigation of submerged plate vibrations, revealed that added mass shows significant variation when the submergence depth of the plate is smaller than the half of its characteristic dimension (length for rectangular and diameter for circular plate). For larger depth the added mass remains constant.

Consequently, it was decided to test a "deep" and a "shallow" case. For each case, the submergence depth that corresponds to the central position of RBM range, were determined with respect to the diameter of the flexible plate (80 mm). In the first case, the submergence depth is set to be equal to the plate's diameter. In the second case, the submergence depth is smaller than the plate's radius (i.e. 25 mm), which means it is closer to the free surface. All the cases to be tested are shown in Figure 4.21.



Amplitude [mm]	Frequency [Hz]						Position
	1	2	3	4	5	6	
5							Shallow
10							Deep

FIGURE 4.21: Experimental matrix for each case of plate's thickness

## 4.6 Summary

The work flow described in this chapter included all necessary actions that needed to be taken before the realization of the experiments. First of all, the main objective of the experiment, which is to offer validation data to FSI solvers, and its repercussions are highlighted.

Taking these into account, two approaches were investigated. In the first one, the structure of interest is a flexible plate that is a part of a water container's bottom. The plate would be excited due to pressure variations within the water domain produced by the vertical periodic motion of a cylinder placed in the container. This approach showed several weaknesses. The major of which was that it was impossible to find the sweet-spot between the requirements, referring to the structure, of strength and inherent flexibility. Therefore, a second approach was needed where these flaws do not longer exist. To achieve that, the flexible plate is placed inside a water container through an otherwise rigid hollow plunger. Hydrostatic pressure acts on both sides of the plate, so the strength requirement was eliminated. The oscillation is imposed to the plunger which means that the boundaries of the plate are moving according to this oscillation. The resulting deflections of the flexible plate are to be measured with optical instruments placed beneath the water container.

Having established the approach to be followed, the arrangement could be designed in detail. To begin with, the measuring instruments along with their purpose and technical characteristics were determined. The list of instruments includes a set of 3D DIC cameras and a single point LDV, both used to measure the response of the flexible plate. Also, there is a laser displacement measurer to monitor the RBM of the plunger. Finally, a load cell attached to the shaft system, that connects the oscillator with the plunger, is to measure the applied force. Additional required equipment, includes an electromagnetic linear drive that would oscillate the plunger, a bearing that restrains any lateral motions of the plunger and light sources that would illuminate the region around plunger's bottom to facilitate DIC measurements. Apparently, detailed designs of all structural components which needed to be fabricated were, also, created.

Finally, designing the experiment includes, also, the definition of the experimental matrix. The parameters involved were related to the flexible plate's thickness, the oscillation characteristics (frequency and amplitude) and the submergence depth of the plate.

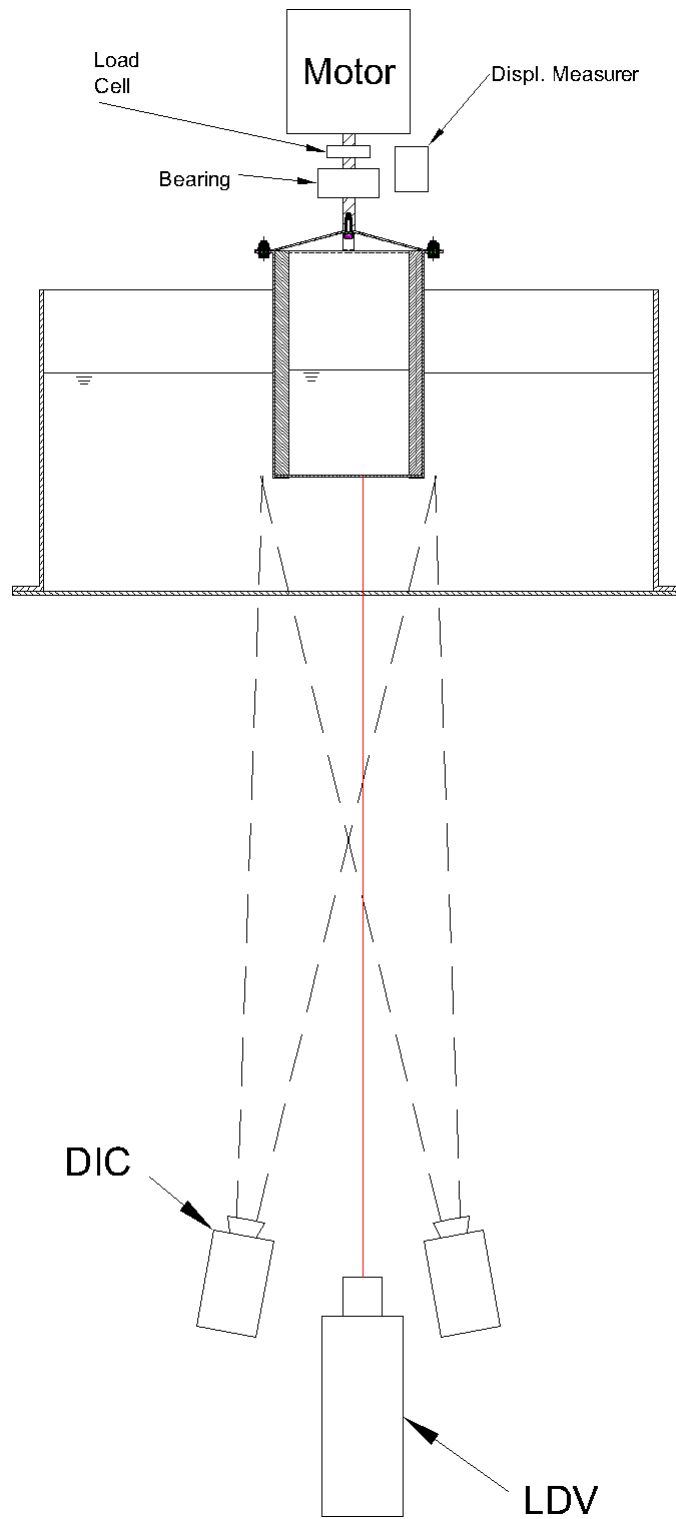


FIGURE 4.22: Schematic presentation of the experimental arrangement

## Chapter 5

# Preparation of the experimental arrangement

### 5.1 Introduction

Once both the goals of the experiments and the way to achieve them have been defined, the realisation of the experiments can begin. In this chapter, the preparation of the experimental arrangement is described in detail. Firstly, there is a brief elaboration on aspects of assembling structural components and measuring instruments. Having the structural part of the setup finalized, the crucial issue of data acquisition was settled. Then, all measuring instruments were calibrated for the needs of the particular set up. Finally, the aspect of recording the free surface in the water container was added to the set-up, in order to investigate the possibility of measuring the water elevation at the container's side walls.

### 5.2 Set-up fabrication

This section refers to the realization of the detailed designing described in the previous chapter. The description that follows does not include the fabrication of structures which involve material processing in workshop. On the contrary, the process of defining DIC set up parameters, required before system's calibration, is described extensively.

#### 5.2.1 Support structure assembly

The support structure consists of aluminium columns connected with angle brackets made of aluminium or zinc. The whole structure consisted of two parts: the main structure and the superstructure. The purpose of the former part is to support the PMMA water container with its wooden base plate and the measuring instruments placed beneath it (DIC cameras and LDV head). The relative distances were determined according to Figure 4.8 and equation 4.15, respectively. Since the plunger was to be placed in two different positions, the horizontal columns to which the optical instruments were attached, had to be capable to be vertically translated. The superstructure bears the alignment plate, upon which the linear motor with the shaft system (motor's slider, load cell, shaft and bearing) and the laser displacement measurer.

#### 5.2.2 Alignment

All these components placed on the superstructure were installed before any other component of the set up was installed at the support structure. The reason for that, was that the linear motor was used as a reference for aligning all remaining

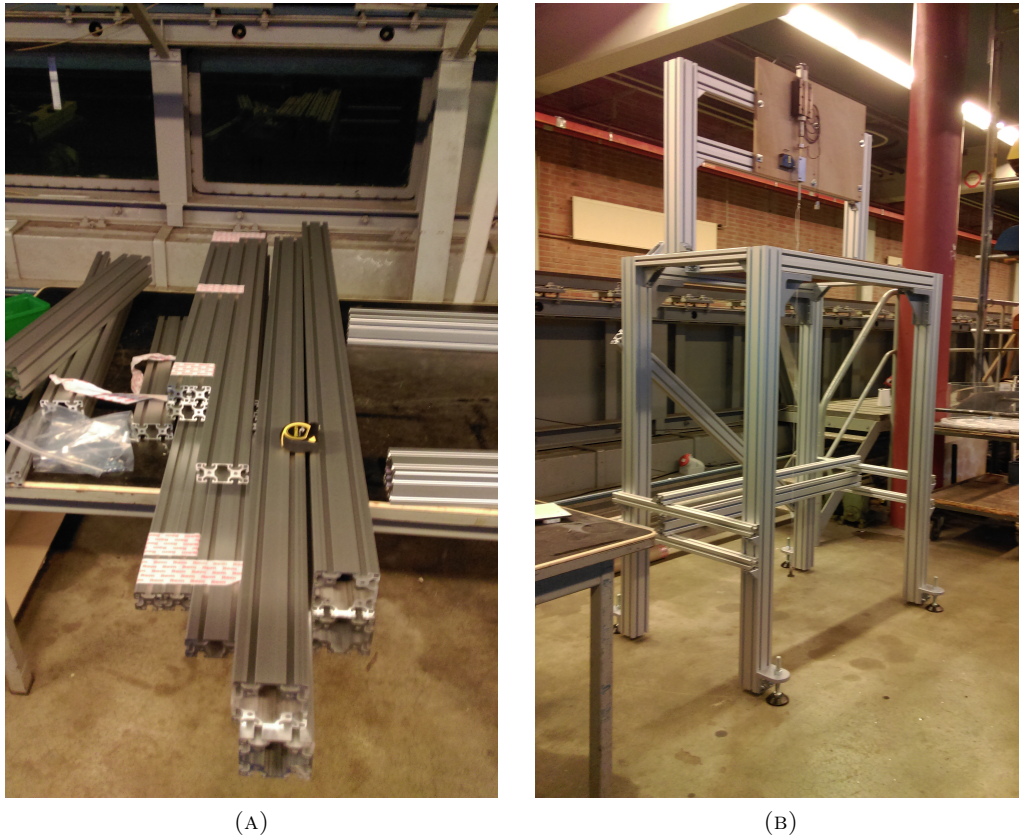


FIGURE 5.1: Aluminium columns before and after assembling

components. To do so, a rope with a wedge at its tip was attached to the motors slider. Symmetry lines were marked at the container's wooden base. Using a ruler, the position of the base plate was adjusted so that the rope coincides with the plate's centre point. Using the rope, reference points were marked at the horizontal columns that would bear the LDV and the DIC cameras. These instruments were placed accordingly, based on the fact that this reference point corresponds to the centre point of the plunger's bottom.

### 5.2.3 Positioning the LDV head

As already mentioned, the vertical distance between the plunger's bottom and the LDV head was determined according to Eq. 4.8. For both cases of plunger position (i.e. deep and shallow) the distance was set to 1050 mm. With respect to the horizontal position, the expected mode shapes need to be taken into account, in order to avoid any nodal point. The modes of circular plates include nodal circles and diameters (Fig. 5.2). The position of nodal circles are expected at the edges or/and at a co-centric circle of half size. On the contrary, the exact position of nodal diameters can not be predicted, apart from a single point of them: the centre. The oscillation frequencies of the investigated cases are low enough, so that the fundamental mode is expected to dominate the response. However, it was decided that the laser spot should be placed between the centre and second nodal circle, determined by theory.

Another aspect of the set-up, that needs to be taken into account, is the reflection due to the bottom PMMA plate of the water container. More specifically, the



intensity of the reflected laser beam can be larger than the one of the back-scattered beam from the target plate. Usually, the practice followed is that the window is tilted slightly, so that the reflected beam does not enter the laser head. For the particular set-up, a slight tilt of the water container would ruin one of its most important aspects, which is symmetry.

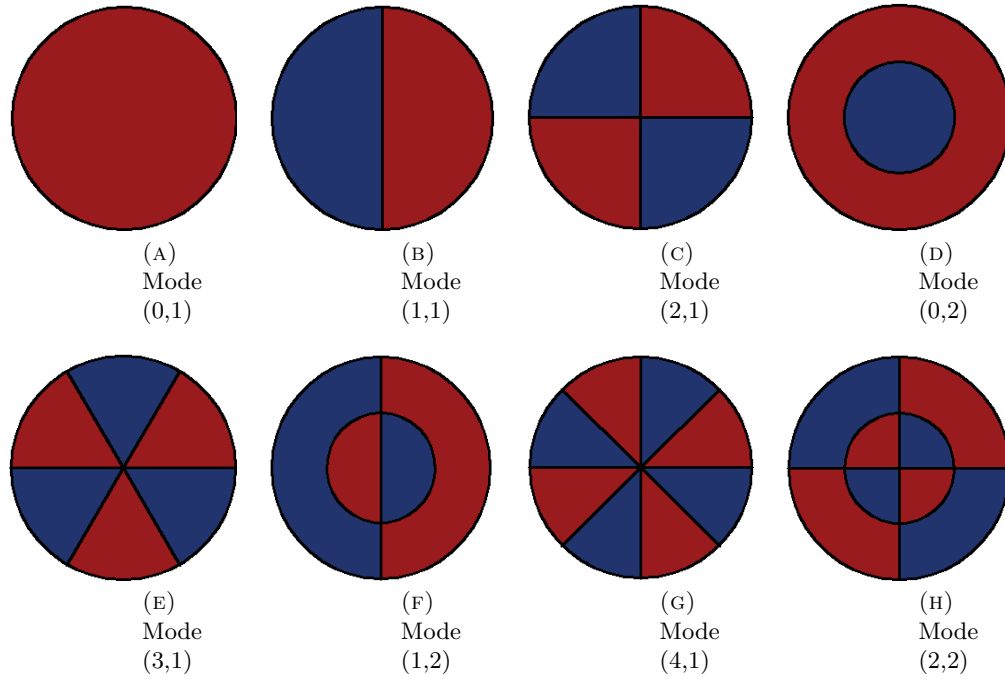


FIGURE 5.2: Mode shapes of circular plates

It was, therefore, decided to give a minor tilt angle ( $\leq 1^\circ$ ) to the LDV head. This was achieved by positioning a gusset between the laser head and the adapter plate, through which it was attached to the support structure.

#### 5.2.4 Plunger preparation for image correlation

The key feature of DIC working principle is the detection of a black and white contrast pattern on the measured object. For this reason, the plunger's bottom surface needed to be painted accordingly with paint that would not be affected from surrounding water. The contrast pattern chosen consisted of a white background and black stochastic speckle pattern. The size of speckles and the distance between would determine whether the success of image correlation and the obtained spatial resolution. However, the speckle pattern was produced using a conventional airbrush, and, therefore, the aforementioned characteristics could not be controlled with great accuracy. A lot of trials were needed in order to obtain the desired results.

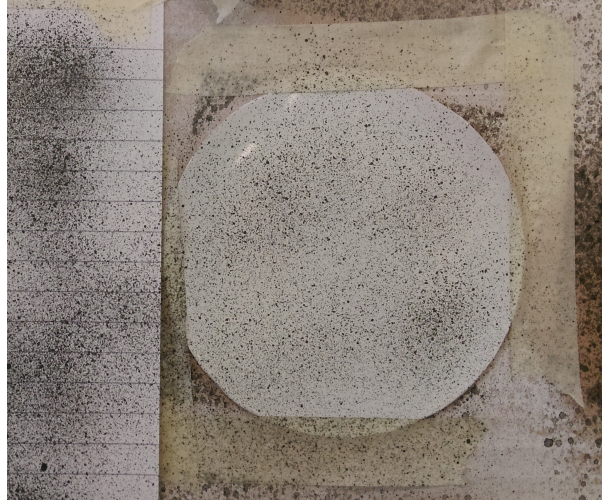


FIGURE 5.3: Application of black speckle pattern on the flexible PTFE plate

The contrast pattern needed to be applied both on the flexible and the rigid part of the plunger's bottom. With respect to the former, a large number of specimens was prepared for redundancy. As far as the rigid part is concerned, DIC measurements of the RBM would be necessary for cross-checking the measurements acquired from the rest of the instruments. Finally, in order to avoid dissolution in water, white acrylic paint was used for the background. However, for the speckle pattern, black graphite paint was used and, therefore, significant amount of time required for the surface to dry before placed in water.

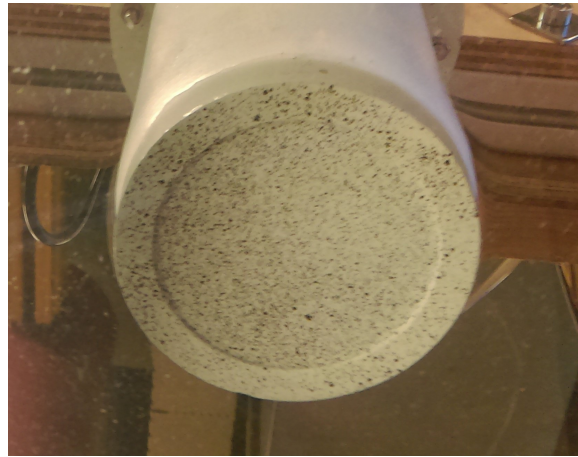


FIGURE 5.4: View of plunger's bottom from the position of DIC cameras

### 5.2.5 Configuring DIC set-up

The most challenging step to finalise the arrangement was the configuration of DIC cameras. Apparently, the objective was to configure the parameters of the set-up so that images of good quality could be obtained for all cases. One of the key features to achieve this, is to provide targeted illumination to the surface of interest. More specifically, the lighting should illuminate the field of water inside the container and reflections towards the DIC cameras had to be avoided. For this reason two LED

were positioned around the water container, while the rest light sources of the room were switched off.

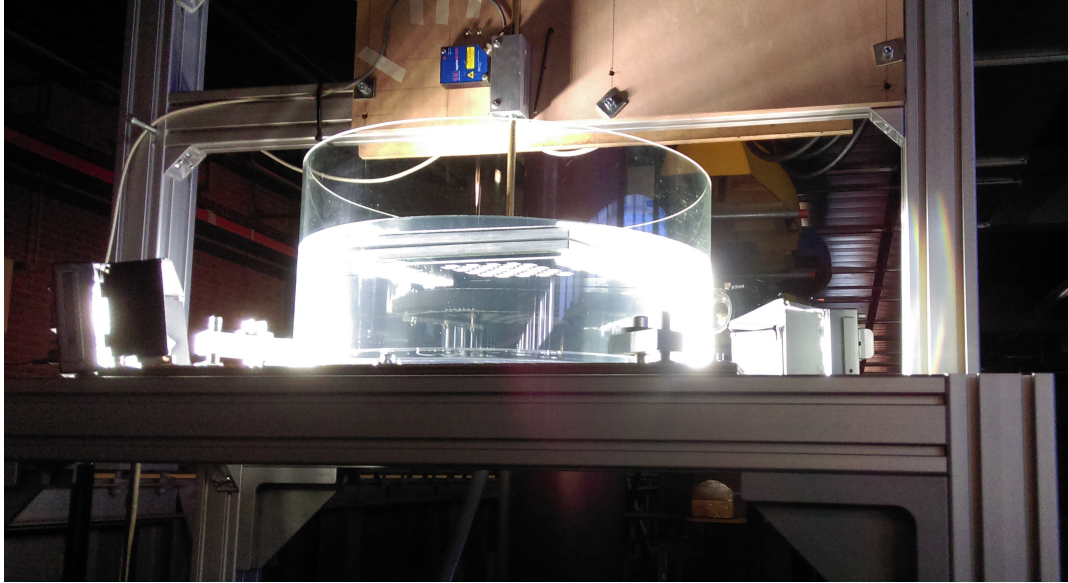


FIGURE 5.5: Two LED lamps placed around the water container for targeted illumination to the plunger

The positioning of the cameras has a crucial impact on the quality of the images. It is affected by the required relative distance between cameras and the surface of interest and the relative angle between the camera's direction and the normal to the measured surface direction. An initial value for the former was determined using Equation 4.10. With respect to the latter, it is prescribed by the supplier company that for 3D measurements this angle should range from 20 to 30 degrees. As the angle gets larger, the sensitivity to out-of-plane displacements is increased. However, large angles may create problems with the focus of the images. The focus remains constant on plane parallel to the CCD receiver of a camera. Since there should be a relative angle between the measured surface and the CCD receiver the focus varies with a single field of view. As soon as the measured surface remains within the focus depth of this variation is imperceptibly small. The cases investigated in this series of experiments involve relatively large total displacements ( $\sim 20mm$ ). It was observed that for angles near the upper limit (i.e. 30 deg) the focus varied significantly at a single image for all positions within the motion range. For this reason, it was decided that the relative angle should remain at lower values (i.e. 21 – 22 deg).

The accurate positioning of each camera has to be done along with the adjustment of the focus, the aperture size and the shutter time. Only the last of the aforementioned parameters can be adjusted after a calibration of the DIC system. However, both the aperture size and the shutter time affect the brightness of the images and that means that both should be chosen wisely before one proceeds to the calibration. As already discussed, the illumination could not be ample due to unwanted reflections. Moreover, the shutter time should be as small as possible, due to the fast motions to be imposed. After several trial tests the shutter time ended up to be set at  $3\mu s$ . Larger shutter times would increase the brightness, but they resulted to blurred images. Shorter shutter times led to shadowed images. For the same reason, the aperture was kept almost wide open.

## 5.3 Setting up the control instruments

### 5.3.1 Data acquisition, triggering and synchronization

One of the key features of the experimental arrangement is the presence of two types of measuring instruments. On one hand, there are the instruments of which the outputs are analogue signals and, on the other hand, there are the cameras of which the images can be processed only using a specialised software. Consequently, the completion of the experimental set up requires the management of electric signals that control the operation of the whole arrangement and the synchronised acquisition of measurements derived from different instruments.

As already described in previous chapter, the stereoscopic system of cameras include a DAQ box capable to handle eight analogue signals along with the image acquisition. However, the sampling frequency of the cameras and, thereafter, the corresponding DAQ box is limited to 30  $Hz$ . Since it is important to have as many data time points as possible per oscillation cycle, there is no point to limit the rest of the instruments to such a low sampling rate. For this reason, a second DAQ box was needed to handle the analogue signals.

One of the most crucial aspects of the signal management is the synchronization of the analogue signals and images acquired from the sensors and DIC system respectively. Inevitably, using two separate DAQ boxes introduces the necessity of signal synchronization which can be achieved with an interconnection between them. This interconnection should give the capability to coordinate the measurements' time points with the image acquisition time points.

In order to ensure that this is achieved, the triggering of the image acquisition needs to be precisely controlled. The DIC system's DAQ board has the feature to acquire images according to an external clock. This clock has the shape of a TTL signal of 5 Volts and variable frequency. The setting of image acquisition using an external clock is flank sensitive which means that one can select whether the images will be acquired at the rising or the falling flank of the (Figure 5.7). Consequently, for the triggering of image acquisition and a TTL signal generator was used (Figure 5.6).

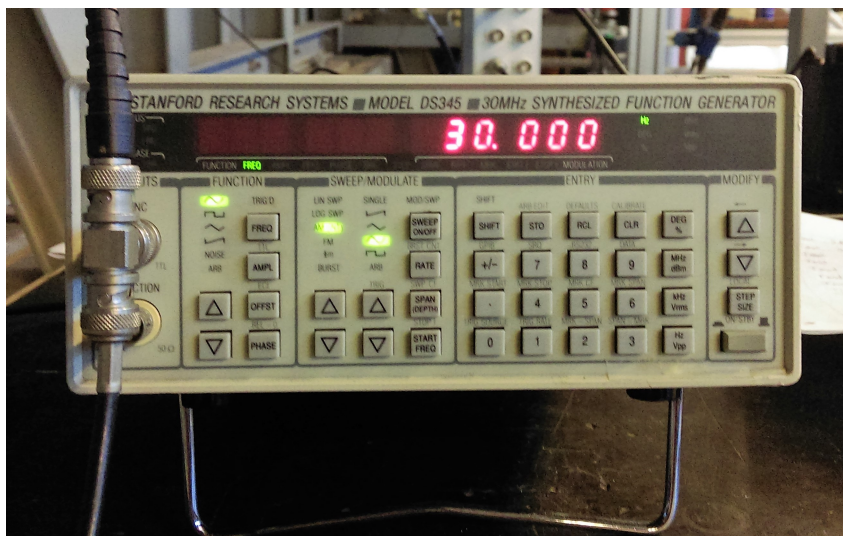


FIGURE 5.6: Control panel of signal generator used for image acquisition triggering



Its output signal was splitted so that it can be imported to both DAQ boxes. With respect to the analogue signals DAQ box, the sampling frequency are set to be an integer multiple of the sampling frequency of the DIC system. In this way, the time points of image acquisition are recorded to both DAQ boxes, thus all acquired data can be synchronized.

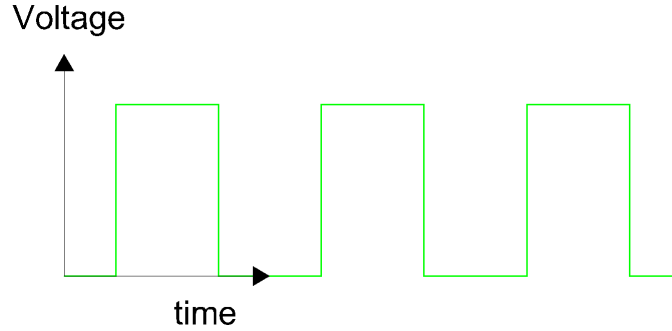


FIGURE 5.7: Triggering TTL signal for DIC image acquisition

### 5.3.2 Filtering and amplification

The measurements coming from analogue signals of all sensors used for this series of experiments needed first to be filtered in order to limit the level of noise. Therefore, a filtering box with a 2<sup>nd</sup> order Butterworth low-pass filter was used. The maximum possible cut-off frequency was equal to 100 *Hz* and that was the value set for the signals of the triangulation displacement measurer and the force transducer. The signal of the LDV was filtered only by the 4<sup>th</sup> order Butterworth low-pass filter of its own controller. The minimum possible value of cut-off frequency was used which is equal to 10 *kHz*. Apparently, the choice of skipping the filter box particularly for the LDV signal was done intentionally, in order to be able to capture as many frequency components of the flexible plate's vibration, as possible. Any noise would be identified and filtered out, during post-processing. Finally, the signal of the force transducer was amplified before acquired by the second DAQ box.

### 5.3.3 Oscillation enforcement

The operation of the electromagnetic linear motor is controlled by a software developed by the manufacturing company. The user can define all necessary characteristics for the control of the imposed motion, like the motion curves, external forces, the positioning of the motor and the PID control system characteristics. The imposed motion was supposed to be imported to the oscillator's driver through this software. However, the storing capacity of the driver is not sufficient to handle the motion curve to be imposed. For this reason, a separate software that acts as a signal generator, needed to be employed. More specifically, files with '.txt' extension that contain time series of voltage were imported to the software. With respect to the required wiring, the signal was exported with USB cable from a PC to the DAQ box Nr.1 (Fig. 5.15) and from the output port with a BNC cable to the linear motor's control unit. The function that translates the voltage to displacement was controlled by the oscillator's software.

The motion curves initially created for the experiments had sinusoidal shape with frequency and amplitude values set according to the experimental matrix described in previous chapter. The phase was selected to be equal to 90° *deg* so that the motion starts from the upper position of the periodic motion. This value was

selected based on the premise, that if the motion started from the equilibrium position (where the velocity is maximum), the acceleration at the initiating time point would theoretically reach infinity. Severe accelerations can be handled by the particular linear motor, but, on the other hand, it is possible that the strain gauges of the force transducer can be permanently deformed distorting the measurements. For the same reason, the oscillation frequency was progressively increased to the target value. This frequency sweep period lasted in seconds the value of the target frequency. Finally, for practical reasons, the motion curves included a ten - second period of stand stillness before the actual motion was imposed. The period of motion lasted 30 second, so that more than enough number of cycles of motion is available.

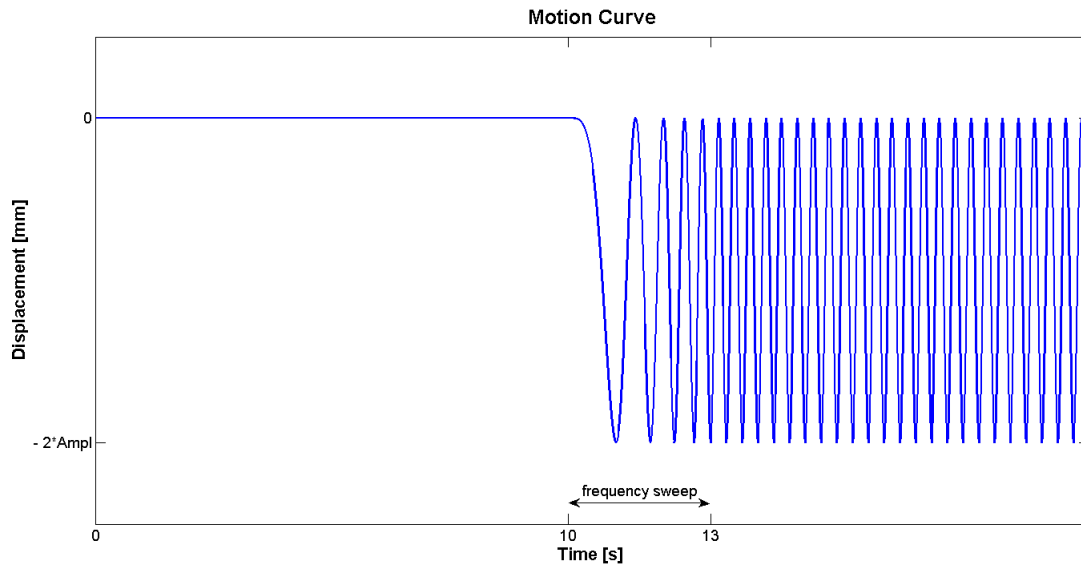


FIGURE 5.8: Example of a motion curve for target frequency of  $3Hz$

## 5.4 Calibration

For instruments with analogue output, the calibration procedure involves the derivation of a transfer function. For the stereoscopic camera set, calibration is a standardized procedure which is necessary for the cameras to adapt their projection parameter to a particular set up. In this section the procedures followed for the calibration of all instrument used are described in detail.

### 5.4.1 DIC cameras

The calibration of the cameras set-up includes the definition of their operating parameters, which can be categorised into the *intrinsic* and *extrinsic* parameters. The former ones, refer to the imaging parameters of each camera (e.g. focal length), while the latter ones refer to the relative distance and orientation of each camera with respect to the other one and the surface of interest.

Intrinsic	Extrinsic
Focal length $\{x, y\}$	Translation $\{x, y, z\}$
Principal point $\{x, y\}$	Rotation $\{x, y, z\}$
Radial distortion $\{r^2, r^4\}$	
Tangential distortion $\{t_x, t_y\}$	

TABLE 5.1: List of parameters calculated during a calibration of DIC cameras

To achieve that, a series of images of a standardised surface, called *calibration target plate* and placed at the same position as the measured surface. The target plate bears a black and white chequerboard patter.

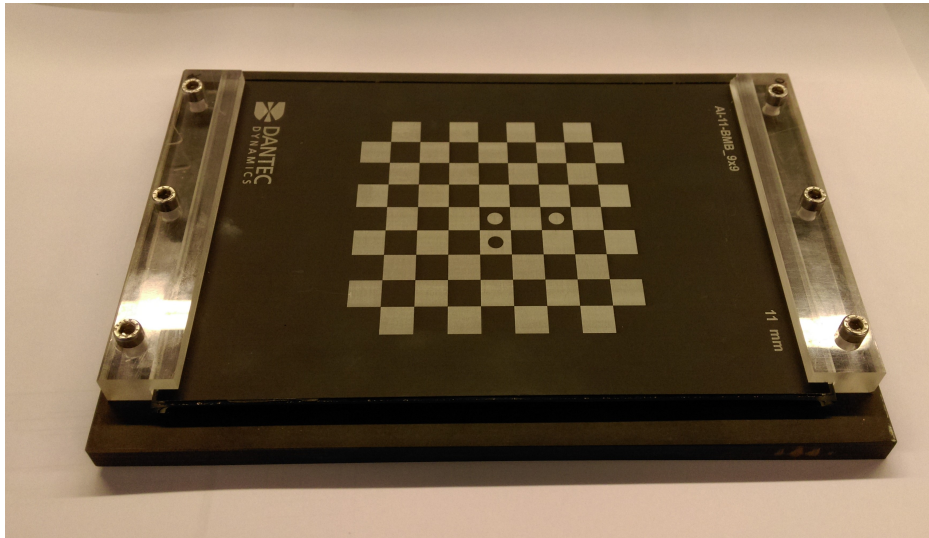


FIGURE 5.9: DIC calibration target plate attached to its adapter plate

The size of the pattern should be large enough to cover the whole field of interest, otherwise the plate should be translated to cover the whole area during the calibration. In addition, it is necessary that in the series of images, the target plate should be hold in different orientations. In all images, both cameras should be able to detect a minimum number corners of the blue and white squares. This minimum number can not smaller than 50% of the total number of corners but, in practice this limit is set to 75%. As, shown in Figure 5.9, at the central squares of the pattern there are circular markers with the opposite colour. These markers are detected at the first image of the calibration series, in order to formulate the initial coordinate system. The centre of the central white marker defines the origin point. The direction from the origin to the neighbouring black marker defines the  $x$ -axis, and the  $y$ -axis is defined by the direction to the neighbouring white marker. Finally, the  $z$ -axis is perpendicular to the target plate with positive direction towards the plane of the cameras. Having the first three imaged recorded, the software initiates the calculation of the calibration parameters. The calculations involve an optimization process. The resulting uncertainty of the found corners is demonstrated by a *residuum* in the unit of pixels. For a successful calibration the residuum should not exceed the value of 0.5. Calibrations that result to residuum larger than 1 are unacceptable.

Apparently, any change of the camera's intrinsic or/and extrinsic parameters, makes a new calibration necessary. Inevitably, for this particular series of experiments, three calibrations need to be performed each for any case of plunger's position (see Figure 4.21). The calibration target plate should be placed at the position that the plunger's bottom plate would be at the experiments. However, as described in the previous chapter, the range of plunger's motion is going to reach  $20\text{mm}$ . During calibration, the target plate was placed at the mid-value of this range. For its accurate positioning at the desired locations, the target plate was connected through a long rod to the linear motor. In order to make this connection feasible, an adapter plate with a threaded hole was fabricated. In order to be able, to apply the desired rotations to the target plate during the calibrations, the adapter plate was connected to the rod through a ball mount base, generally used for cameras. During the calibration the target plate was rotated with angles that were progressively increased in order to increase the sensitivity of the cameras to displacements in the out-of-plane direction. However, very large angles may set some corners outside the field of view and, also, increase the uncertainty (residuum).

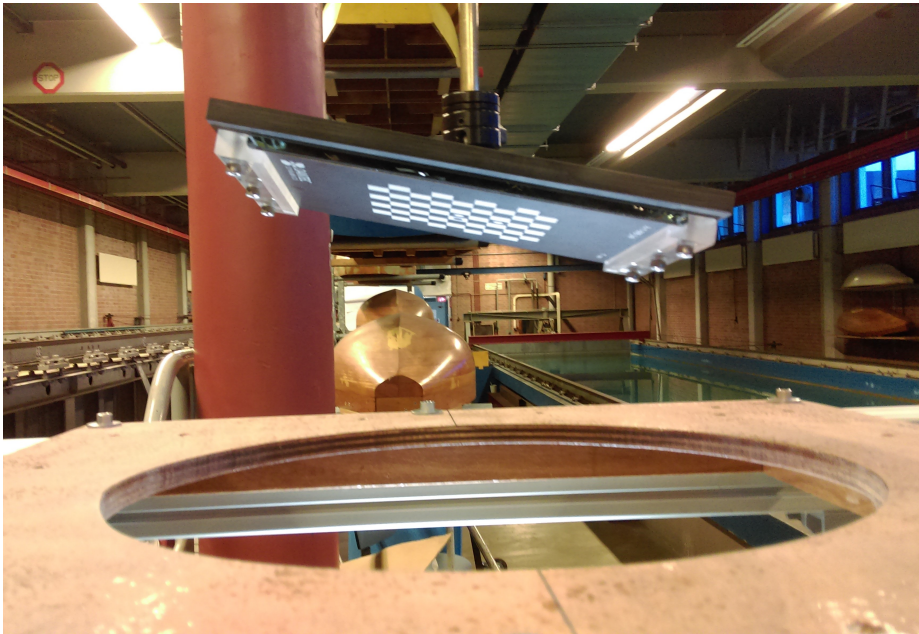


FIGURE 5.10: DIC target plate rotated, during calibration for "dry" experiments

Great care was given, so that the focus depth of the cameras was large enough so that clear images are obtained not only at the calibration position, but also at the limits of motion range. This was successful up to a certain extent. In practice, locally the clarity level of images was not constant for different positions within the motion range. This effect was enhanced as the relative distance and, therefore, the relative angle between the cameras increased. However, it is prescribed, that the relative angle between the cameras, can not be smaller than 40 degrees. After several trial and error adjustments of the cameras' focus, images of good quality within the whole range. Finally, the residuum numbers achieved for the calibrations that were used for the experiments are shown at Table 5.2.



Position case	Residuuum [pixels]
Shallow	0.341
Deep	0.373
Dry	0.405

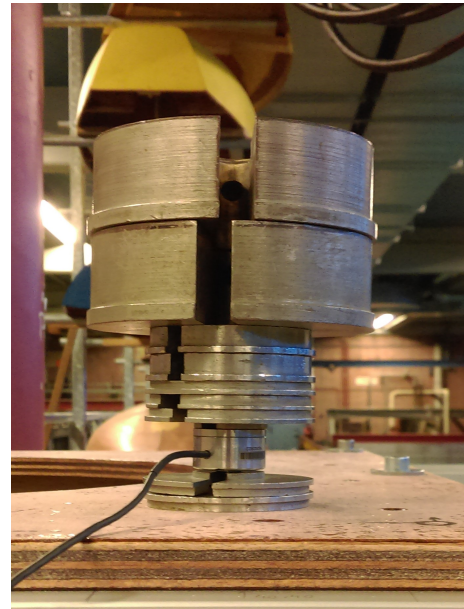
TABLE 5.2: Achieved uncertainties for each calibration case

### 5.4.2 Force transducer

Contrary to DIC cameras, the calibration of the force transducer is not a complicated procedure. Although a linear transfer function was expected, several cast iron test weights were used. It was expected that during the experiments, both compression and tensile loads would be imposed to the plunger (see Fig. 4.13). Therefore, a hanger of negligible weight was used for tension and a holed plate was used for compression.



(A) Tension



(B) Compression

FIGURE 5.11: Force transducer loaded with test weights for calibration

The results of several calibrations, are presented in Figure 5.12. The fitted curve is, also, included. The equation of the fitted curve (i.e. transfer function) is the following.

$$\text{Newtons} = 23.55 \times \text{Volts} - 0.04918 \quad (5.1)$$

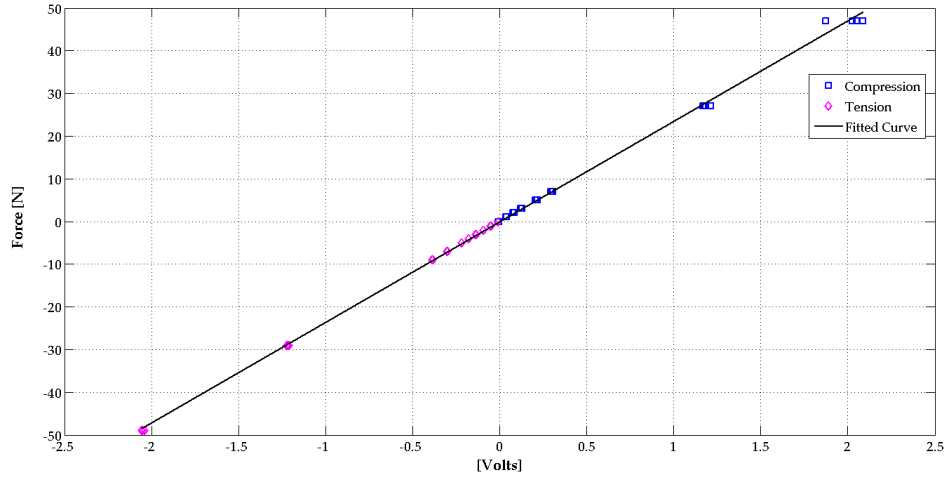


FIGURE 5.12: Results of force transducer calibration

### 5.4.3 Triangulation laser displacement measurer

The laser displacement measurer used for measuring the rigid body motion of the plunger has a range from 60 mm to 260 mm (Table 4.6) and it pointed towards the plunger's upper flange. During the experiments the plunger would be oscillated around two levels of its bottom submergence (i.e. shallow and deep). During the calibration, the plunger was attached to the linear motor and displacements were applied around the aforementioned positions. The exported transfer function gives the distance in *mm* with respect to the plane of the laser head.

$$\text{Millimeters} = 24.02 \times \text{Volts} + 11.16 \quad (5.2)$$

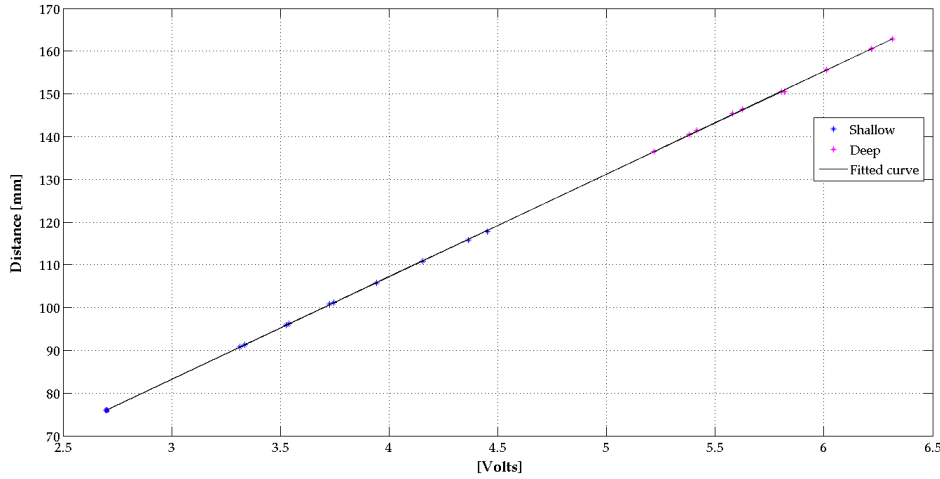


FIGURE 5.13: Results of triangulation laser displacement measurer calibration

### 5.4.4 Laser Doppler vibrometer

The output of the LDV would be an analogue signal representing the velocity of a single point at the PTFE plate. Hopefully, the controller (OFV-2200) of the laser head, that bears the velocity decoder, gives the possibility to the user to select the scaling factor of the measurements among three choices that are listed below.

Scaling Factor	Peak-to-peak range output	Resolution
5 $\text{mm/s}/V$	100 $\text{mm/s}$	0.5 $\mu\text{m/s}$
25 $\text{mm/s}/V$	500 $\text{mm/s}$	2 $\mu\text{m/s}$
125 $\text{mm/s}/V$	2500 $\text{mm/s}$	5 $\mu\text{m/s}$

TABLE 5.3: Velocity decoder of OFV-2200 measurement ranges

Due to the relatively large rigid body motion that would be imposed, the largest scaling factor ( $125 \frac{\text{mm}}{\text{s}}/V$ ) was chosen. However, in practice, a very small offset was detected in measurements of zero velocity. This was scaled with the selected factor and then subtracted from the measurements.

## 5.5 Setting up a video camera for water elevation measurements

Having the experimental arrangement fully prepared as it was designed beforehand, a video camera was added to the general set up. Initially, the purpose of this camera was just to record videos of the experiments. However, it was observed that it may be possible to be used for other purposes and specifically for measurements of the free surface elevation.

The experimental approach described so far, involves measurements for quantities related to the motion of a structure inside a fluid domain, while there are no measurements related to fluid velocity or pressure. The reason for this, is that conventional instruments, such as pressure and wave gauges, would intrude the water, in order to provide valuable measurements. In this way, the fluid flow would be distorted and the geometry of fluid domain would turn out to be more complex. As already stated, one of the most important aspects of this experimental arrangement is the reduced complexity, so that it can be replicated easily in numerical simulations with respect to setting up the model and computational cost. On the other hand, PIV is a non-intrusive technique that can offer fluid flow measurements on a plane, which would be sufficient for a symmetric set-up. However, its use involves a Class-IV and, inevitably, the resulting interference among all optical instruments (i.e. DIC and LDV) would be catastrophic.

However, the illumination provided for purposes of DIC measurements created noticeable contrast between the water and ambient air. This aspect could be exploited by focusing the video camera to the free surface during the experiments. For this reason the video camera was positioned next to the water container. Their relative angle was such, that the cameras was looking towards the centre of the container. The purpose was to measure the water elevation at the tank's side walls. The measurements would be obtained after processing the videos recorded during the experiments. Finally, it must be mentioned the experimental set up was not modified at all for this kind of measurements, since they were not included in the initial plans. Therefore, the success of this procedure can not be guaranteed.

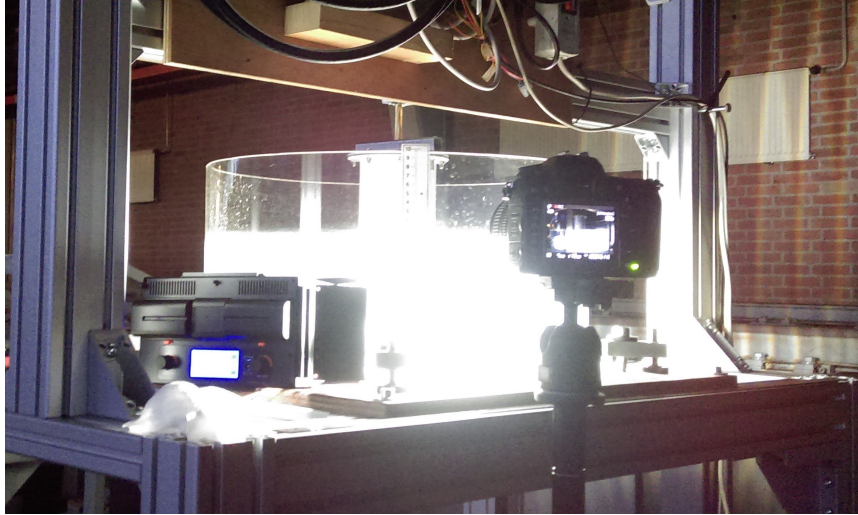


FIGURE 5.14: Achieved contrast between water and ambient air

## 5.6 Summary

This chapter elaborates on the procedural tasks required to be executed before beginning the experiments. The process began with assembling the support structure and positioning on it all components of the set-up. Great care was taken on the alignment between the linear motor - shaft - plunger assembly and the water container. Moreover, all optical measuring instruments were placed at the appropriate positions, according to the values of optimal stand-off distances indicated by the supplier companies. Measurements with a DIC set of cameras requires preparatory works, such as speckle pattern application on the measured surface and, of course, the necessary configurations of the camera set-up required before proceeding to its calibration.

Another important aspect of the experimental set-up, is the signal manipulation. The unavoidable presence of two DAQ units (one for analogue signals and one for DIC cameras) raised the need of an interconnection between them, in order to synchronize the measurements. This was achieved by means of a reference signal, which, in practice, was the signal used for triggering image acquisition from DIC cameras.

Once the arrangement was fully prepared, all measuring instruments had to be calibrated. For those with analogue output, the calibration procedure involved the derivation of a transfer function. For the DIC camera set, calibration is a standardized procedure of determining the projection parameters, which was necessary for the cameras to adapt their projection parameter to the particular set up.

Finally, an extra feature was added to the general arrangement, without affecting any of its aforementioned aspects. More specifically, a video camera was positioned beside the water container aiming at the free surface. Due to the noticeable contrast between water and ambient air, processing the videos may give time-series of the water elevation induced by the plunger's motion.

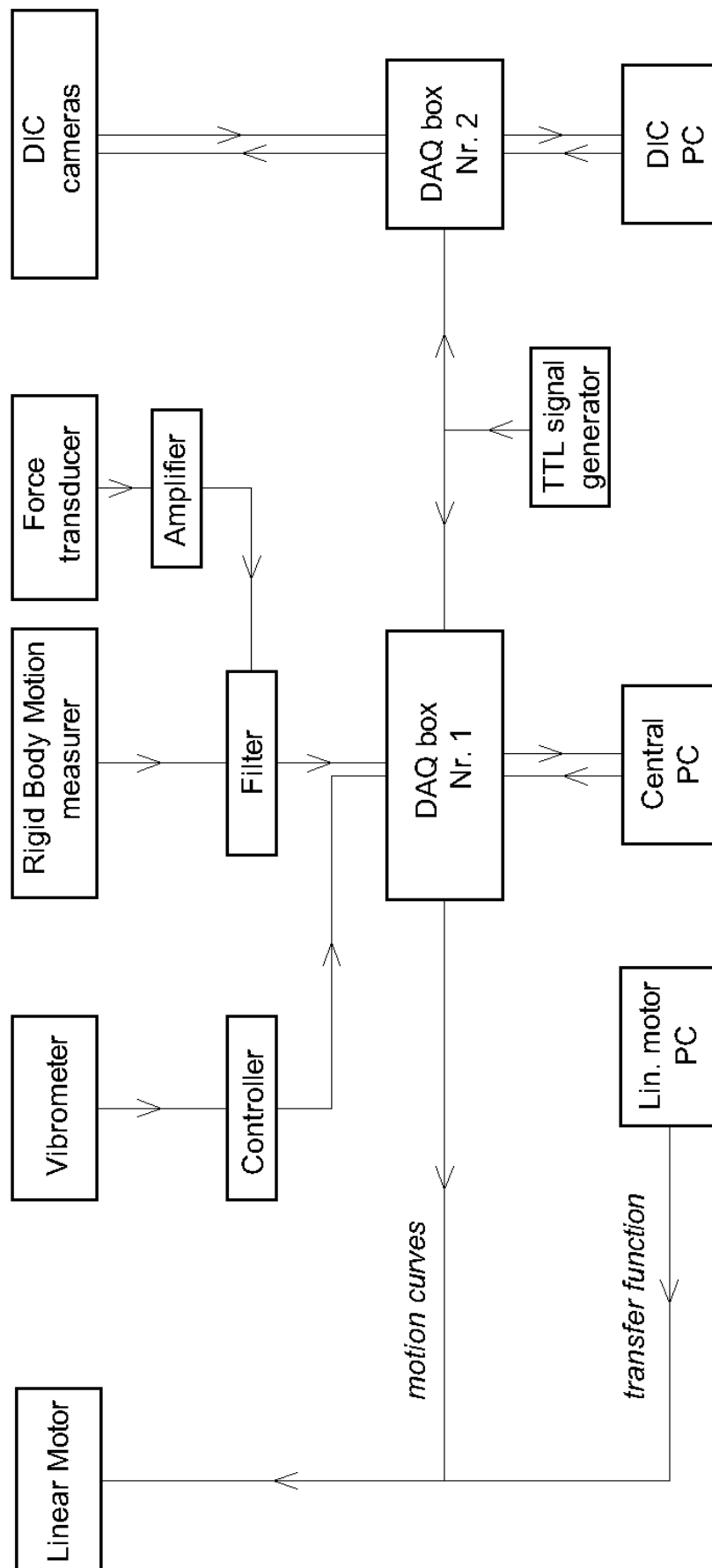


FIGURE 5.15: Schematic diagram of signal flow



## Chapter 6

# Execution of experiments - Results

### 6.1 Introduction

Having the experimental set-up finalized, the experiments were conducted according to the experimental matrix as it is shown in Figure 4.21. However, due to encountered problems the experimental matrix had to be slightly modified. Therefore, before the results are presented, some aspects related to the conducted experiments that finalized the experimental matrix and the cases that were investigated, have to be discussed. Then, representative results from each measuring instruments are presented as well as the treatment to which they had to be subjected.

### 6.2 Cases investigated

While conducting the experiments one major problem was encountered with respect to the cases of higher frequencies (i.e. 5 and 6 Hz). More specifically, for all cases of oscillation frequency equal to 6 Hz and cases of 5 Hz and oscillation amplitude of 10 mm, severe sloshing took place inside the plunger.

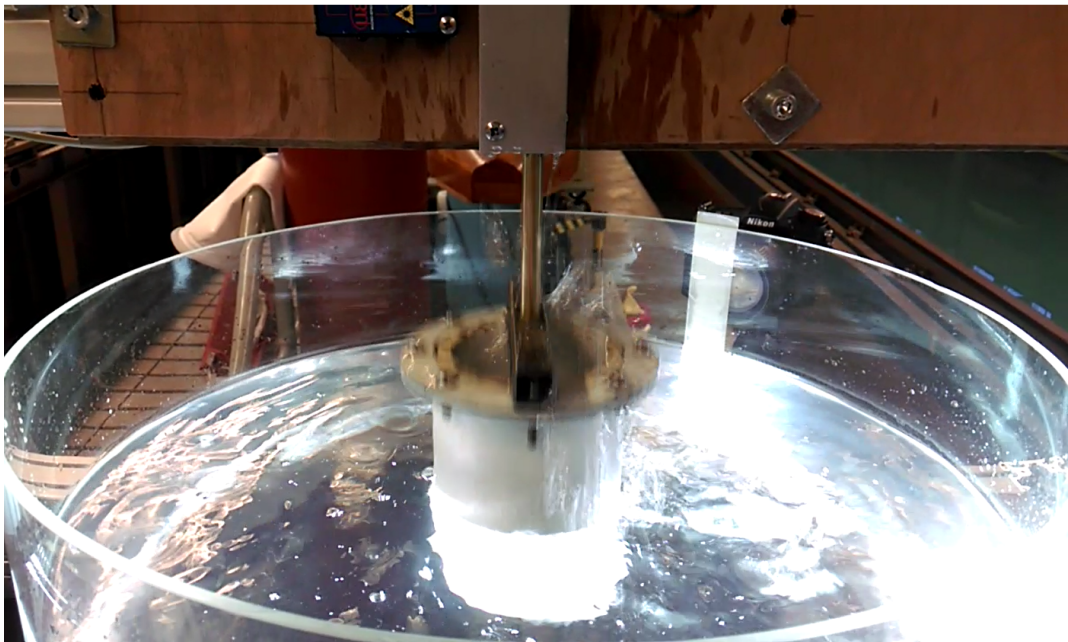


FIGURE 6.1: Sloshing inside the plunger



The measurements were distorted due to the resulting effects, which were the following:

- Water came out of the water container
- Drops of water hit the triangulation laser displacement measurer placed above the water container and the measurements were ruined
- The water coming out of the plunger and hit the free surface of the water container, creating bubble in the interior of the water domain. These bubbles were passing beneath the plunger's bottom and, therefore, images acquired by the DIC system could not offer reliable measurements.

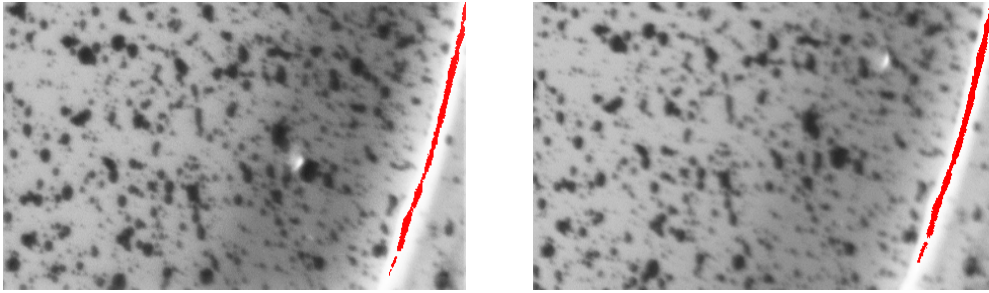


FIGURE 6.2: Bubble travelling beneath plunger's bottom captured by DIC cameras

Due to the unfavourable effects, these cases need to be eliminated from the experimental matrix. Doing so, there were no cases left for oscillation frequency of 6 Hz. For this reason, new cases with frequency of 6 Hz and 2 mm amplitude were added. Moreover, one case of "dry" experiments at  $f_{osc} = 4$  Hz was added for reference.

		Frequency [Hz]					
		1	2	3	4	5	6
Amplitude [mm]	5						
	10						
	2						

FIGURE 6.3: Final version of the experimental matrix for each case of plate thickness



For purposes of the current report, specific cases were selected to be processed and presented. The reasoning behind selecting these cases was that all types of parameters ( $f_{osc}$ ,  $A_{osc}$ , position and plate thickness) had to be included. Moreover, visual observation during the execution of experiments, also, determined the choices made. The investigated case are listed at Table 6.1.

Case Nr.	$f_{osc}$ [Hz]	$A_{osc}$ [mm]	thickness [mm]	Position
1	2	10	0.25	Shallow
2	2	10	0.25	Deep
3	4	10	0.25	Deep
4	6	2	0.25	Deep
5	6	2	0.50	Deep

TABLE 6.1: Investigated cases

### 6.3 Digital Image Correlation

Before the actual results of image correlation are presented, there are still some aspect of their acquisition that need to be highlighted. The sampling frequency of DIC set up can be adjusted from 0.2 up to 30 Hz. For the particular application, larger acquisition frequencies are more preferable. For this reason, the upper limit of 30 Hz was chosen. The signal generator used for triggering was set accordingly as was the image acquisition setting on DIC processing software.

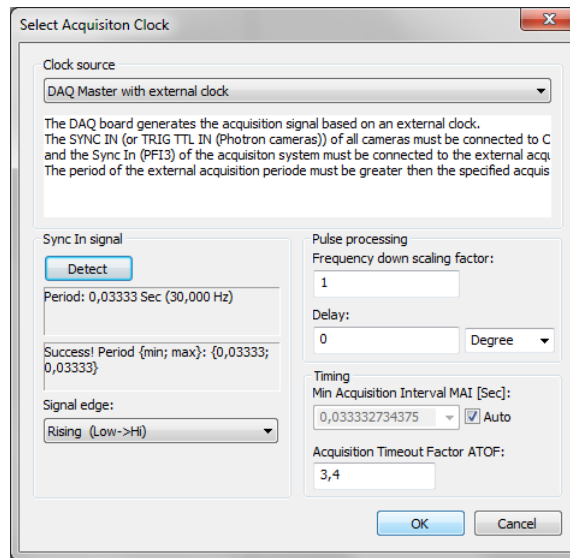


FIGURE 6.4: External clock setting for image acquisition in DIC processing software

However, this creates a drawback with respect to the size of FOV. In fact, as the sampling frequency increases, the size of the smaller side of the FOV decreases from 2054 to 222 pixels. In order to cover the whole area of the plunger's bottom, for each case of the experimental matrix, the experiments need to be conducted 11 times. The transition from one stripe-like FOV to the next involved an overlap of 30 pixels, in order to reduce the possibility of having not correlated regions between the FOVs.

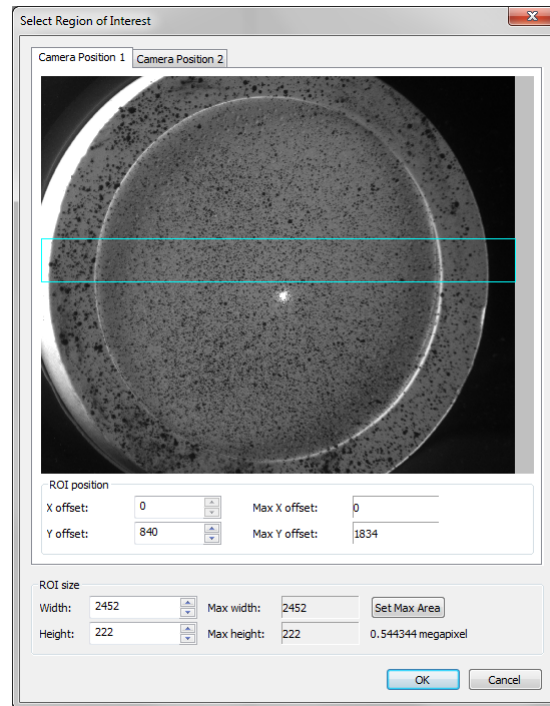


FIGURE 6.5: Selection of the region of interest

### 6.3.1 Evaluation

The process during which the 3D coordinates of the captured surface for each measurement step is described by the term "evaluation". The evaluation process includes a number of steps that are required for a successful image correlation:

#### 1. Evaluation settings definition

In the initial step of the evaluation process the extrinsic and intrinsic parameters of the cameras, calculated during calibration need to be imported. Then, the reference measurement step has to be defined. The reference measurement step is the one according to which the displacements and strains are calculated. This means that at this step, the displacements and strains for all directions are zero. Finally, some advanced settings need to be defined. The most important of those are the facet size and the grid point interval that determine the spatial resolution of the results. Additionally, the maximum value of correlation accuracy is defined in pixels. Facets for which the resulting uncertainty of coordinate measurements exceeds this limit will not be correlated.

#### 2. Mask definition

In this step the region of all acquired images that should be correlated is defined. This region is discretized according to the facet size defined in the previous step.

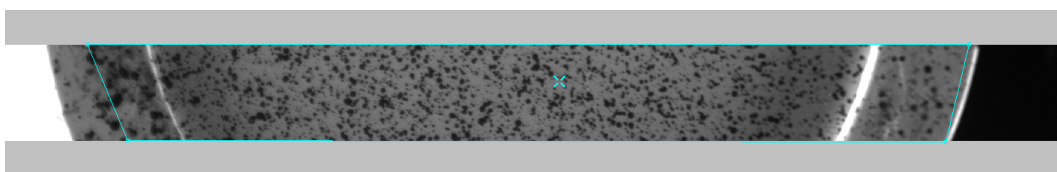


FIGURE 6.6: Definition of mask including rigid parts

### 3. Start-point search

The aforementioned steps were preparatory. From this step the actual image correlation begins. The process starts with the manual definition of a start-point within the mask at the reference measurement step. This point defines the facet from which the image correlation will start. Then, the software should be able to define the exact same facet at all subsequent measurement steps. Theoretically, this can be done automatically. However, in practice there were measurement steps where the software had to be enhanced by manually positioning the start-point. The number of steps for which this was necessary, increased for cases that the imposed motion was faster. The success of the start-point search for each measurement step defines whether this step can be correlated within the accuracy limits set in step. For cases of faster motion, there was a small percentage of images ( $\sim 5\%$ ) for which the accuracy criterion was not satisfied and therefore were not correlated.

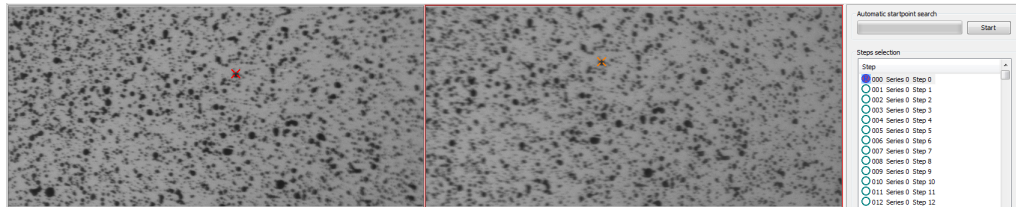


FIGURE 6.7: Start-point search for reference measurement step

### 4. Image correlation

Having the start-points set, the correlation algorithm can be initiated. For each step, the correlation begins from the start-points and, then, follows them optimum path with respect to image quality. The algorithm calculates the 3D coordinates of the measured surface at the grid point set at earlier step.

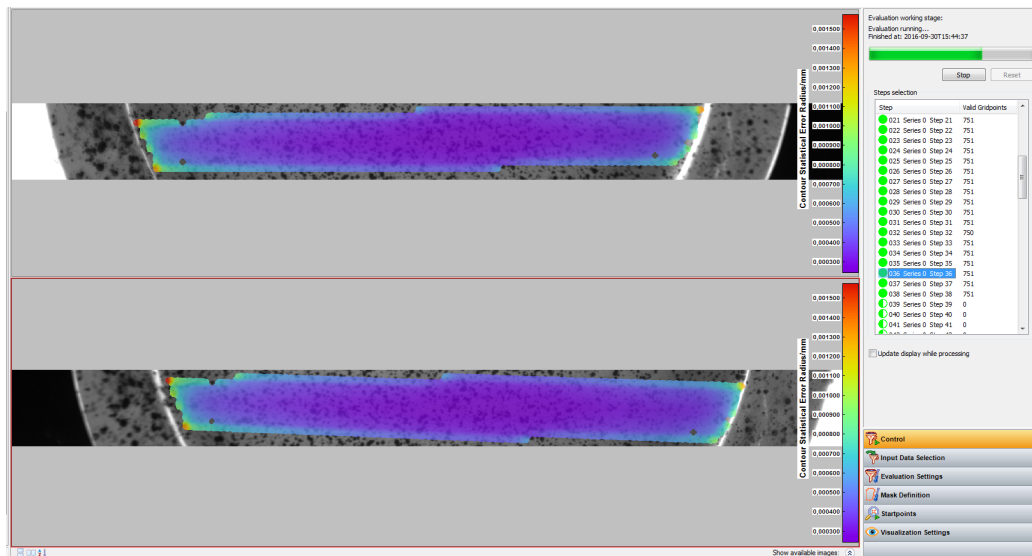


FIGURE 6.8: Presentation of the evaluated facets and the achieved uncertainty

### 6.3.2 Results

The results of image correlation included coordinates, displacements and strains for grid points to which the FOV were discretized. The coordinates were measured with respect to the system of coordinates defined during the calibration process. The displacements in  $x$ ,  $y$  and  $z$  direction and  $x$ -,  $y$ - and tangential strains were calculated with respect to a reference step, which for all cases was set to be the first time step.

For all cases investigated, there were few facets at each measurement step that could not be correlated, because the achieved uncertainty exceeded the maximum permissible value. For almost all measurement steps the number of non-correlated facets was too small to prevent from reaching a conclusion about the mode shapes of the plate's response.

The frequencies of the imposed oscillation (Table 6.3) are expected to be much lower than the fundamental natural frequency of the plate. Assuming a linear response, the only mode shape that was expected to appear at the results was the fundamental one. Indeed, for most measurement steps the mode with one nodal circle (boundary) and no nodal diameter (i.e. mode 0,1) appeared. However, as it is shown in following paragraphs the imposed motion, also, included and higher frequency components. The result, was that in a small number of steps, the response was of higher mode shapes.

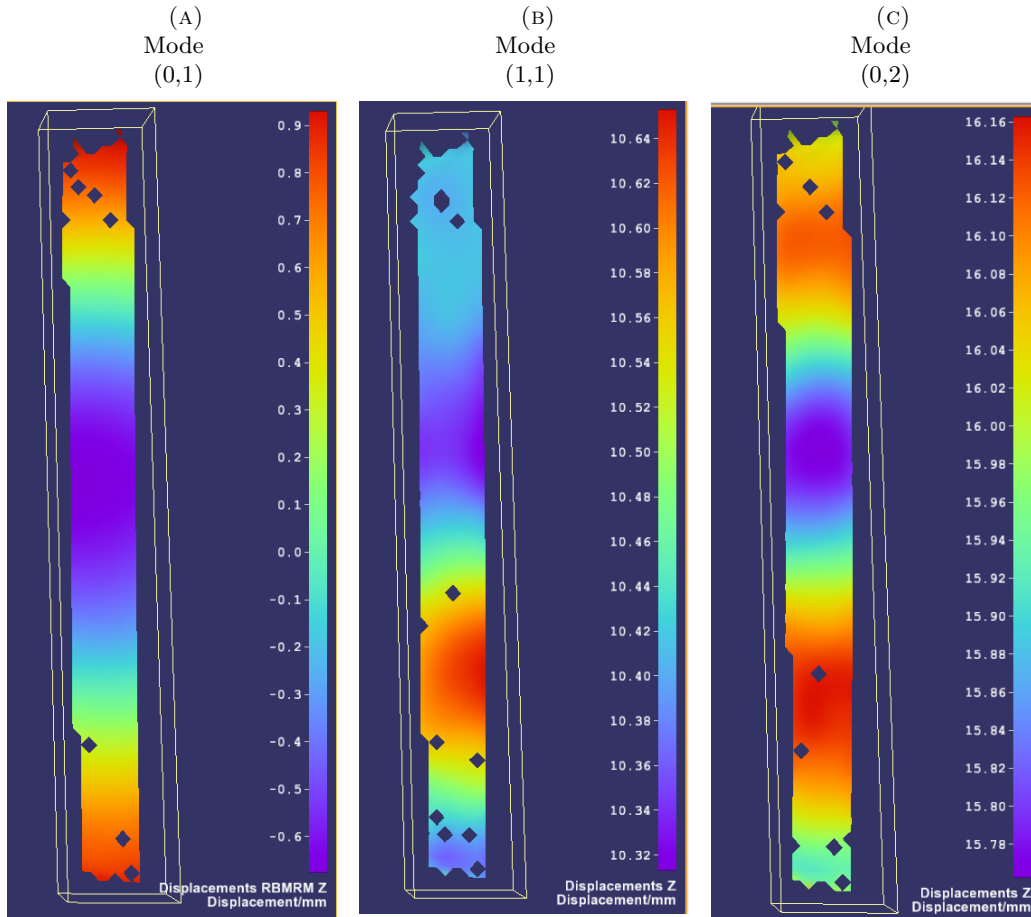


FIGURE 6.9: Indicative snapshots with results of a central FOV for Case Nr.2

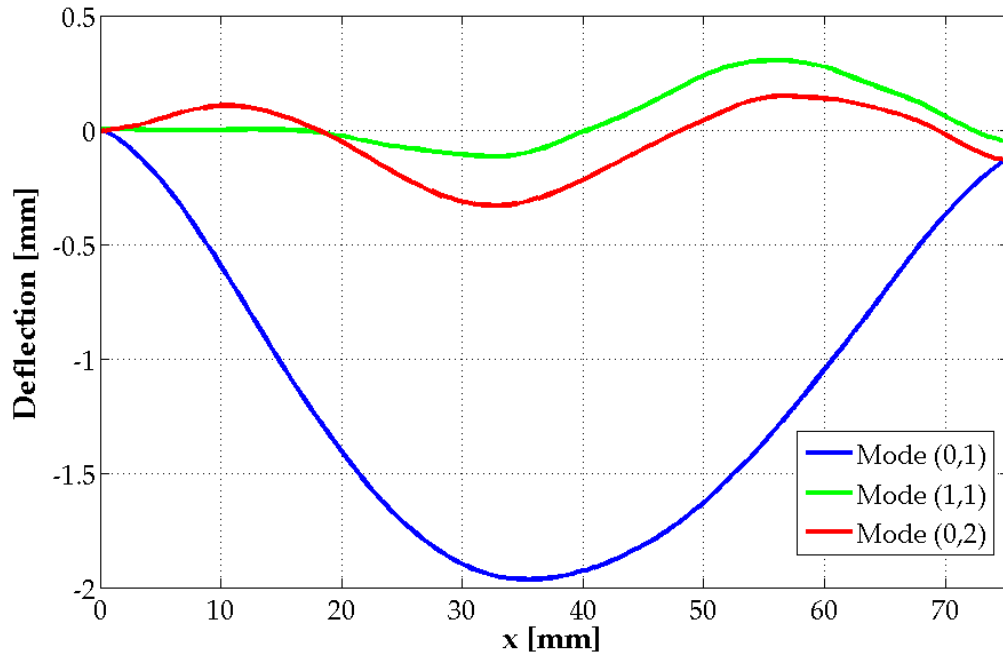


FIGURE 6.10: Deflections along the centre line of the FOV pictured in Figure 6.9

Case Nr.	Maximum Deflection $Z_{\text{defl}}$ [mm]	Max. Normalized Defl. $Z_{\text{defl}}/A_{\text{osc}}$
1	4.36	0.44
2	3.39	0.34
3	5.38	0.53
4	2.92	1.46
5	2.87	1.43

TABLE 6.2: Maximum deflections measured by DIC for all cases investigated

Having conducted an overview of the results for all cases, it was observed that the measured displacements in the  $z$ -direction did not correspond to the ones expected according to the imposed motion. More specifically, there was a deviation between the obtained displacements for on regions on the rigid part of the plunger's bottom with the values of the motion curves imported to the linear motor's drive.

This needed to be investigated further. Using the DIC processing software, gauge points were placed on locations of FOV that correspond to rigid parts, for all investigated cases. Time series of the  $z$ -displacements were exported in order to obtain RBM measurements from DIC (Fig. 6.11). These measurements were compared to the RBM measurements obtained by the laser displacement measurer.

The results of these comparisons validated the first impressions according to which the measured displacements by DIC were smaller than the actual ones. However, these unwanted results did not occur for the experiments during which the plunger was not surrounded by water (i.e. "dry" experiments). Furthermore, the comparison for cases, where the plunger's bottom was at the shallow position, revealed larger deviations than for the cases with the plunger at deep position. In other

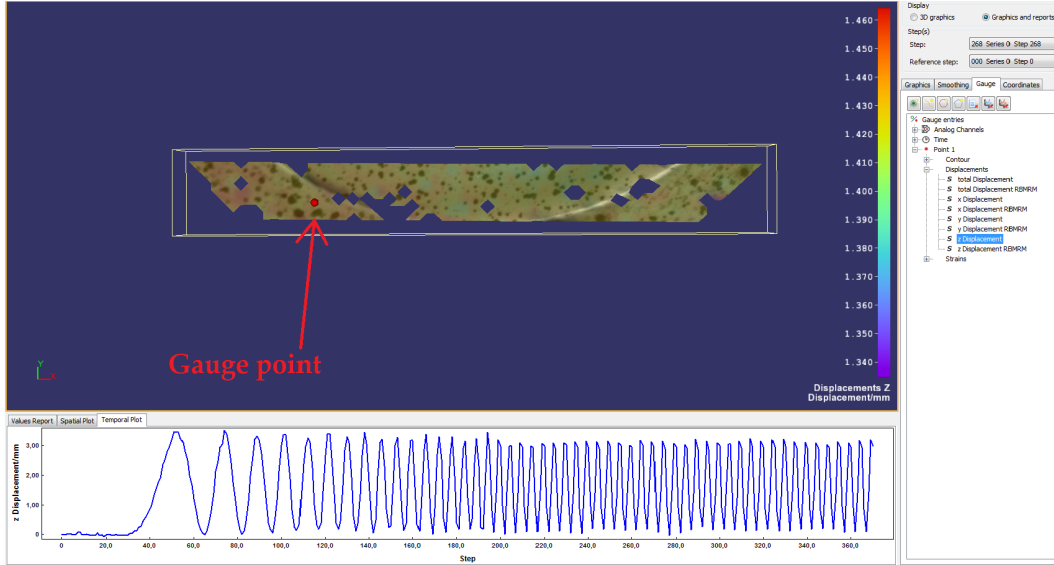


FIGURE 6.11: Gauge point at rigid part of the surface and exported temporal plot of  $z$ - displacements

words, the deviation between the actual position and the one measured by DIC cameras increased with the distance between the measured surface and the bottom plate of the water container. All the aforementioned facts led to the conclusion that the reason for this error induced, was refraction.

Using the RBM measurements of the triangulation laser as reference a scaling factor was calculated for each time step. Then, the total displacements, which include the plunger's motion and the plate's deflections, measured by DIC cameras, were scaled according to this factor. In this way the actual displacements were approximated, also, for the measurements by DIC. The deflections of the plate were approximated by subtracting the measured RBM from the total displacements.

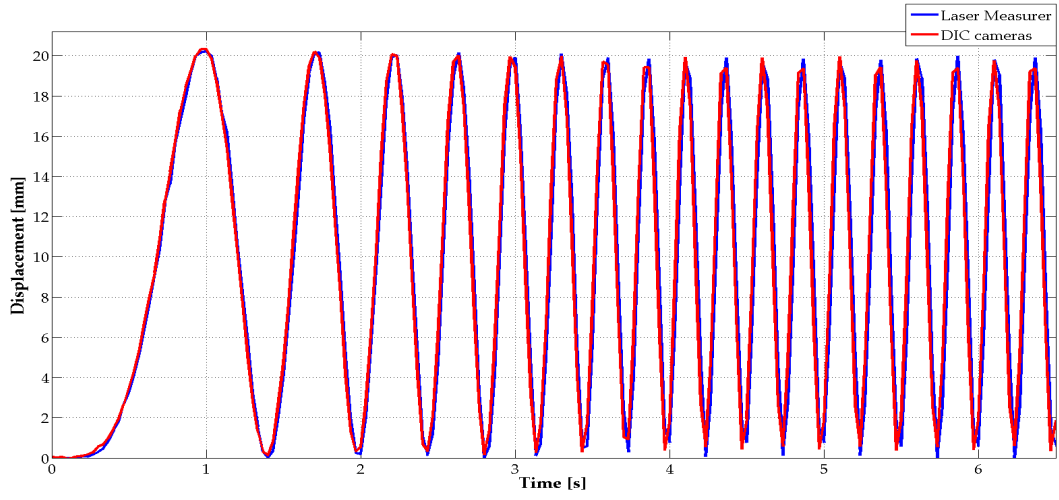
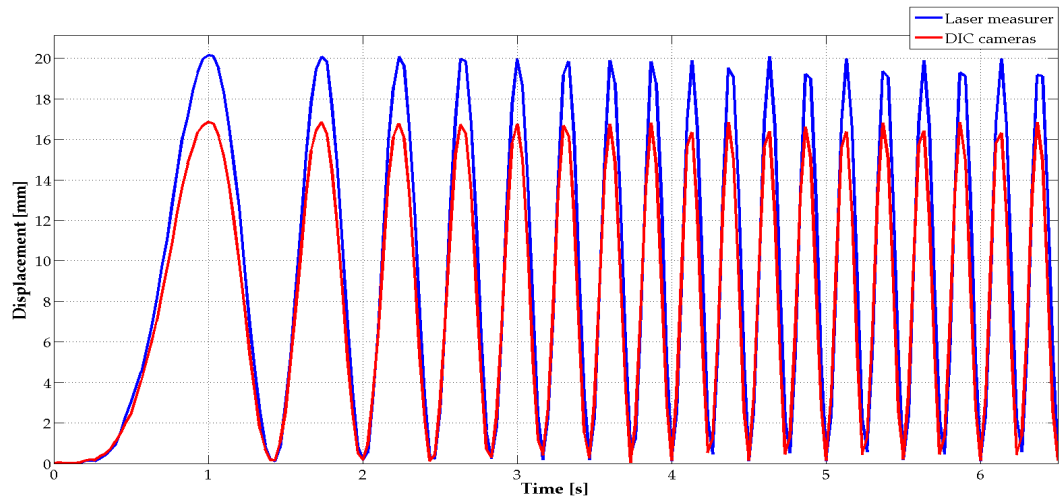
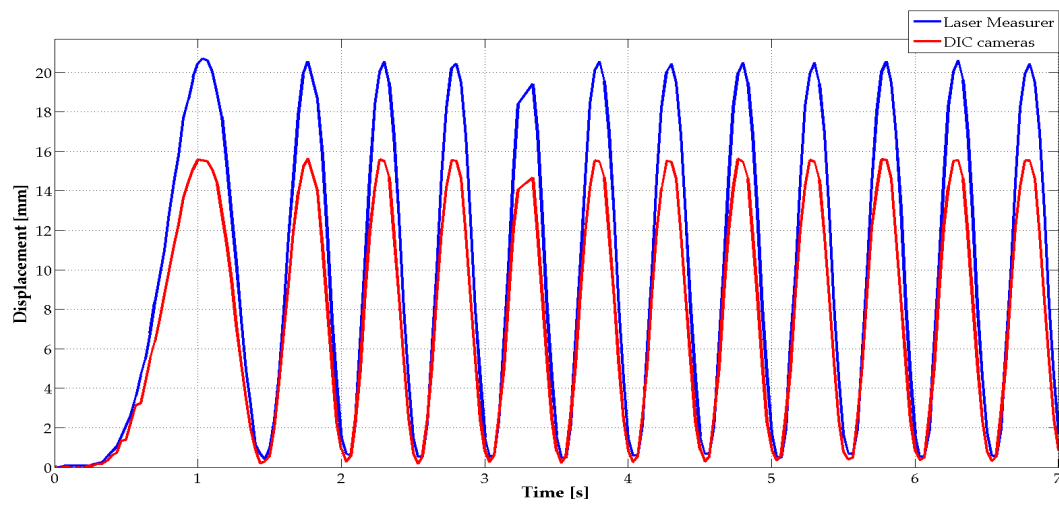
(A) "Dry" case -  $f_{osc} = 4$  Hz(B) "Deep" case -  $f_{osc} = 4$  Hz(C) "Shallow" case -  $f_{osc} = 2$  Hz

FIGURE 6.12: Comparison of rigid body motion measurements between laser measurer and DIC cameras

## 6.4 Laser Doppler Vibrometer results

The measurements acquired by the single point LDV, included time series of velocity at a single point on the flexible PTFE plate of plunger's bottom. The velocity of a structure's point, as any kinematic property, can be used for validating numerical simulations of FSI. Nevertheless, cross-checking the measurements acquired from different instruments would give an indication with respect to the reliability of results. The measurements that are directly related to the structure's deflections are the one acquired from DIC and those the vibrometer. DIC provide full-field measurements of displacements and, therefore, comparison requires the integration of velocity measurements obtained by LDV.

Before cross checking is carried out, any noise components included in the measurements need to be filtered out. It should be mentioned again that, a low pass filter of 10 kHz was applied to the LDV signal, while all the other analogue signals were filtered at 100 Hz. It is, therefore, necessary to analyse the response of the structure in the frequency domain, in order to identify frequency components that derive from the plate's vibrations and filter out the ones attributed to noise.

The major source of noise in LDV measurements derived by the operation of the linear motor. Although the effect of noise at the motor's operation was intense, the imported motion was, at the end, imposed successfully to the plunger. One can assume, that the presence of a thick PMMA plate and water between the LDV head and the surface of interest would be able to induce distortions at the measurements. However, as it is proven at the following paragraphs, the operation of the linear motor was the only source of noise during the experiments.

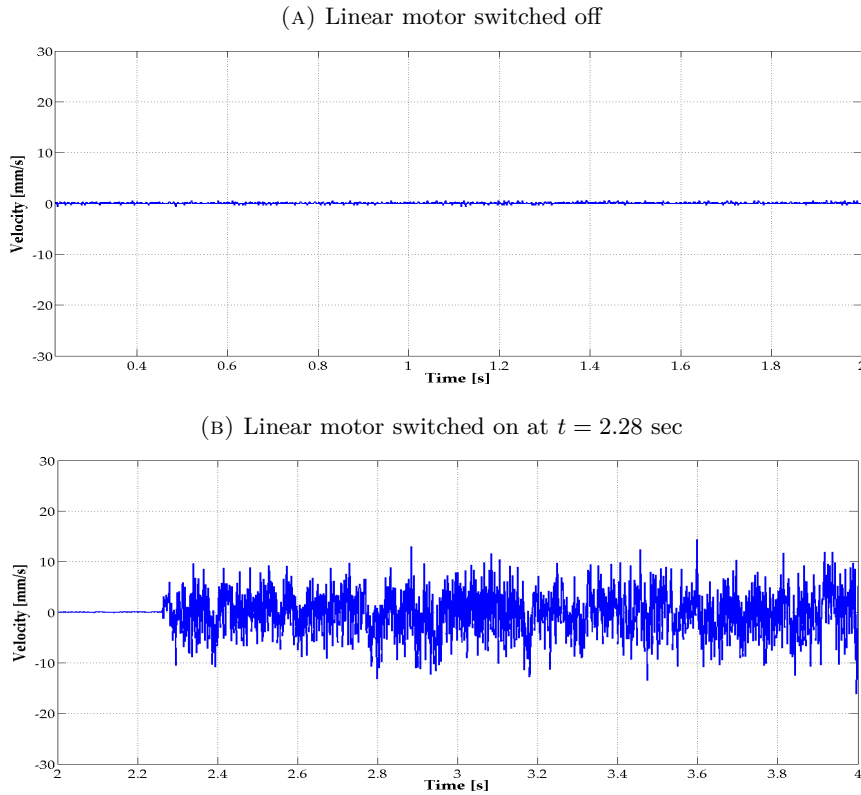


FIGURE 6.13: Velocity measurement by LDV keeping the plunger standstill

For the following analysis, only results of Case Nr. 3 are presented (see Table



6.1). However, the steps followed and the conclusions made apply to all investigated cases.

As described in previous chapter, the motion curves imported to the linear motor included a period of 10 seconds with the plunger kept standstill and, then, the actual motion was imposed (see Fig. 5.8). In order to get an overview of the noise created by the motor, Fast Fourier Transformation was applied to the signals of RBM, force and velocity (LDV signal). The transformation was applied separately to the 10 sec-period of standstill and to the motion period.

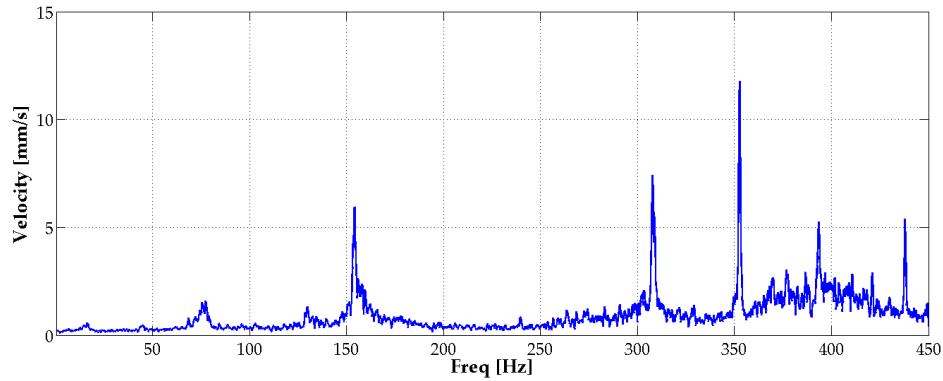


FIGURE 6.14: Result of FFT of LDV signal for standstill period of imported motion curve

The response of the plate, while the plunger kept standstill, in the frequency domain is presented in Figure 6.14. One can observe peaks of different amplitude distributed within the whole range of frequencies of the analysis. This response graph gives an indication of the presence of noise in the LDV signal. Apparently, the period while the plunger is kept still was included in the motion curves only for practical reasons and does not raise any interest for further analysis. The interest is focused to the period of motion, for which the noise should be identified.

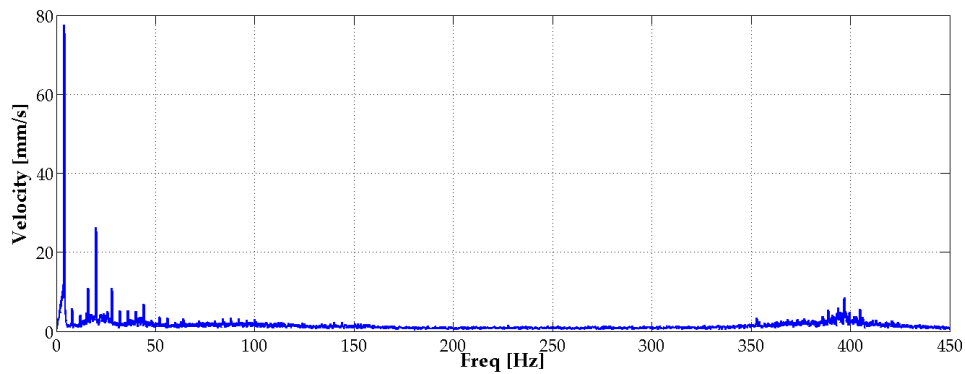


FIGURE 6.15: Response of the plate due to the imposed motion in frequency domain

As expected the largest peak in the graph coincides with the steady-state oscillation frequency. Additionally, there are noticeable peaks at frequencies that are integer multiples of the oscillation frequency. Finally, peaks are, also, found at higher values of frequencies (i.e. from 300 to 450 Hz) for all cases.

### 6.4.1 Noise identification

The observations made by the previous graphs, reveal the need to investigate further the effect of motor's operation to the PTFE plate's response. Moreover, it should be clarified whether any of these effects can be reproduced during the numerical simulations or they induce unwanted parts of response that need to be filter out.

As already noted, there are two noteworthy characteristics of the plate's response in the frequency domain:

- I. Peaks at the integer multiples of the oscillation frequency
- II. Peaks at the higher region of the frequency range.

For these two characteristics of the response, it is required in order to identify whether they are caused by:

- a) the plunger's rigid body motion, or
- b) the bottom's plate flexibility

In case that the first scenario is valid, then further investigation needs to be conducted in order to clarify whether this motion is caused by the linear motor or by the response of the surrounding water. As far as the second scenario is concerned, it need to be specified whether the response is induced by the motor's noisy operation or by the excitation any natural frequency of the PTFE plate.

Transforming, also, the RBM and force signals from time to frequency domain, one can observe that peaks at integer multiples of the oscillation frequency are present at all signals (Figures 6.16 and 6.17). On the contrary, the peaks at higher frequencies are present only at the LDV signal. It is, then, concluded that the integer multiples are attributed to RBM, while the peaks at high frequencies seem to be relevant to bottom's plate flexibility.

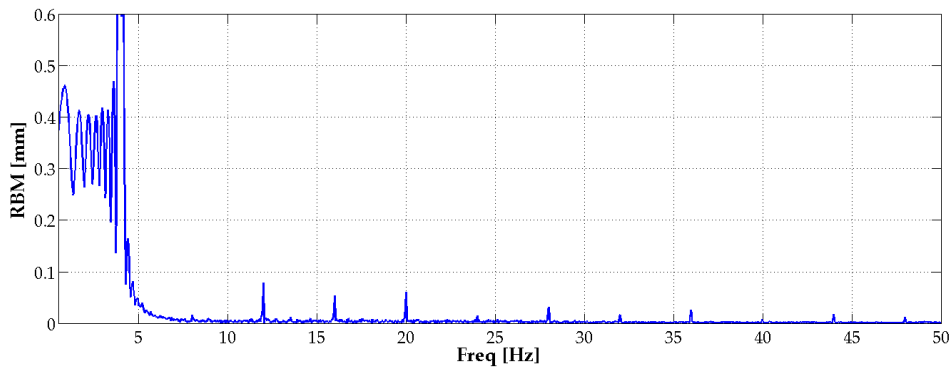


FIGURE 6.16: Zoomed graph of rigid body motion response in frequency domain

Having categorized the types of these response characteristics, now is important to identify the causes for each of these responses. For this reason additional tests were needed.

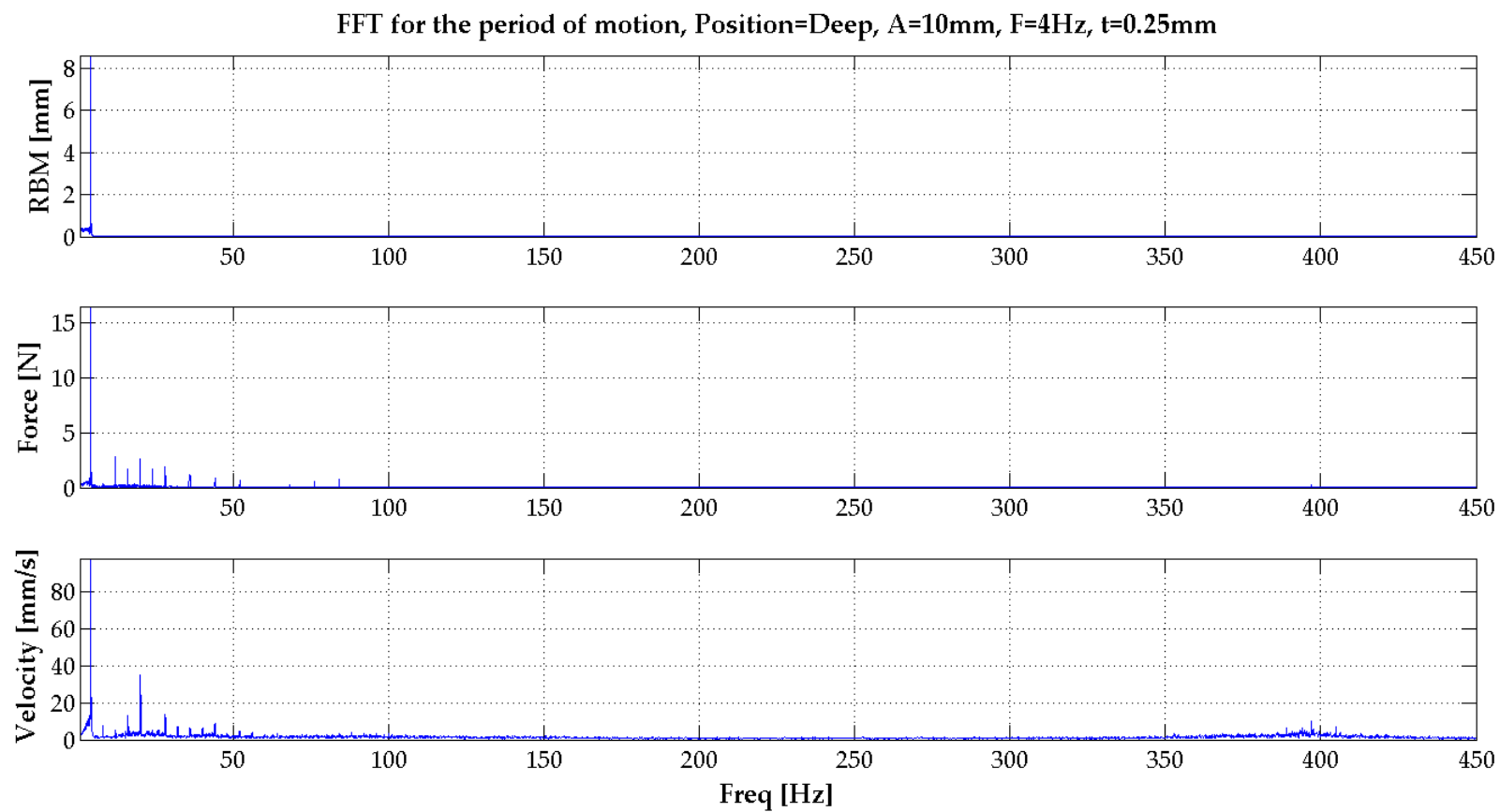


FIGURE 6.17: Graphs of rigid body motion, force and bottom plate's velocity in frequency domain

### "Dry" tests

Since it was verified that the response at integer multiples derives by the rigid body motion of the plunger, it is now left to determine whether this motion is induced by the surrounding water or is an effect of the motor's operation.

In case that the latter is valid, the motion imposed at the numerical experiments should not be the motion curves imposed in the physical experiments but the inverse Fourier transform of the RBM signal in frequency domain. Otherwise, the motion imposed at numerical simulations should be the motion curve created for the physical experiments and the response at the integer multiples of the oscillation frequency should be present in the results.

The results of comparison revealed that the measured amplitudes were smaller for the dry experiments, as expected. Though, the peaks at the integer multiples of the oscillation frequency were there, also, for the "dry" case. This leads to the conclusion that the response at these frequencies is not induced by the variations of pressure around the plunger's bottom

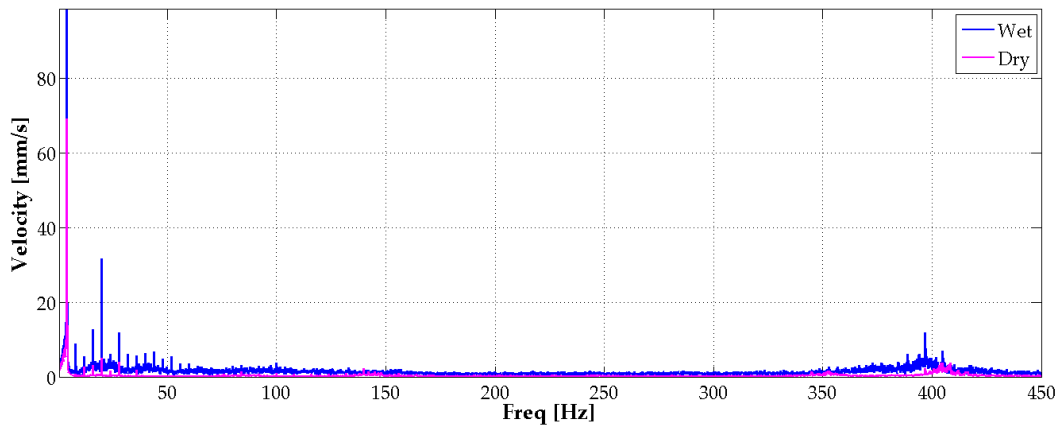


FIGURE 6.18: Comparison between the bottom plate's response in frequency domain between "wet" and "dry" experiments

### Tests with different PID controller settings

The performance of the linear motor is controlled by a PID controller of which the coefficients can be modified. There are two default set of values for the coefficients, the so called "soft" and "stiff" modes. For purposes of the experiments described so far, the "soft" mode was employed.

In order to investigate the impact of PID controller modes to the response in the frequency domain and whether some of these peaks described above can be restrained, additional tests with different control parameters were conducted. More specifically, the default "stiff" and one "softer" mode were tested. Unfortunately, the results did not offer any valuable information, apart from changes in the range of frequencies where peaks at integer multiples of the oscillation frequency. This may be a verification of the conclusion that this effect of the response is attributed to the linear motor's performance.

Mode	P	I	D
"Softer"	1.5	0	3
"Soft"	2.5	0	6
"Stiff"	6.2	0	10

TABLE 6.3: P, I and D parameter values for different controller modes

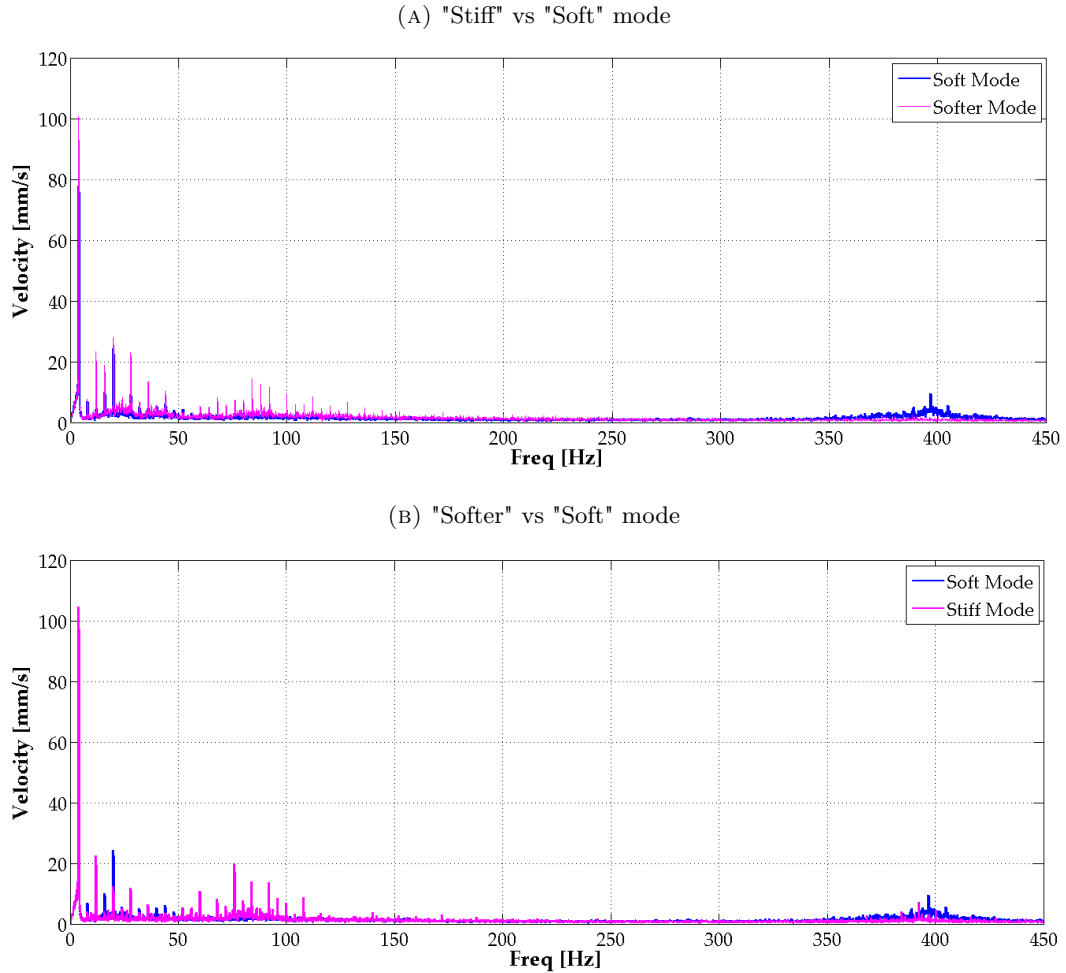


FIGURE 6.19: Comparison of the plate's responses between different PID controller modes

### Tests with rigid bottom

In these tests the PTFE bottom plate was substituted by a PMMA plate covered by acrylic paint in order to make measurements with the LDV feasible. The resulting response included, of course, smaller amplitudes. Peaks at the integer multiples of the oscillation frequency were, also, present. For the peaks at higher frequencies there was a notable change. For the flexible plate one can see the amplitudes increasing from 350 up to 420 Hz. For the rigid bottom there are three sharp peaks in the response around the region of 430 Hz.

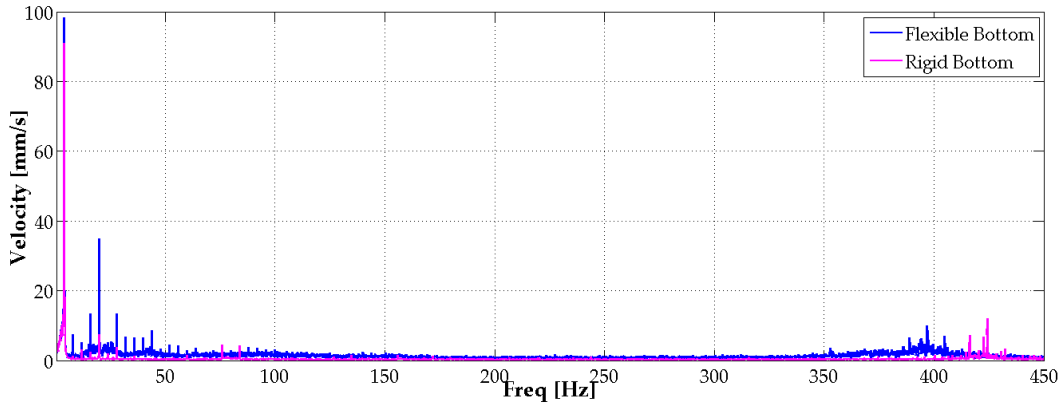


FIGURE 6.20: Comparison between the response of PTFE (flexible) and PMMA (rigid) plates in frequency domain

### Free vibration test

The additional tests described so far, offered valuable information related to the peaks at the integer multiples of the response and how these should be taken into account at the formulation of the imposed RBM in the forthcoming numerical simulations. However, they did not manage to offer any information about which frequency components correspond to noise and need to be filtered.

For this reason, it was decided to conduct one last series of tests. In this series, a fast step excitation is imposed to the plunger and, then, the free vibration of the PTFE plate is measured. It was of utmost importance that the effect of the motor's operation would not affect the measurements. In other words, the free vibration of the plate should be measured with the linear motor switched off.

In order to achieve that, the process followed for these tests was the following.

- The plunger was displaced from its "zero" position by 2 cm upwards.
- A motion curve of standstill at "zero" position was fed to the motor, making it move the plunger downwards by 2 cm, as fast as possible.
- Then, immediately the linear motor was switch off
- Measurements from the LDV were acquired during this whole process

Unfortunately, the linear motor could only be switched off manually and this means that for fractions of a second the effect of noise coming from the motor was present. However, this turned out to be useful for the comparison between the responses that do and do not include noise.

Two response signals were transformed to frequency domain: One includes, only, the period during which the motor was switched off and one included, also, the period during which the motor was still in operation. The results for the former case revealed three noticeable peaks in the response. These peaks can be corresponded to natural frequencies of the plate. On the contrary, the response of the case that includes noise revealed a large number of peaks for frequencies larger than the third peaks encountered in the previous case. Up to this value of frequency, magnification the response's amplitudes were noticed.

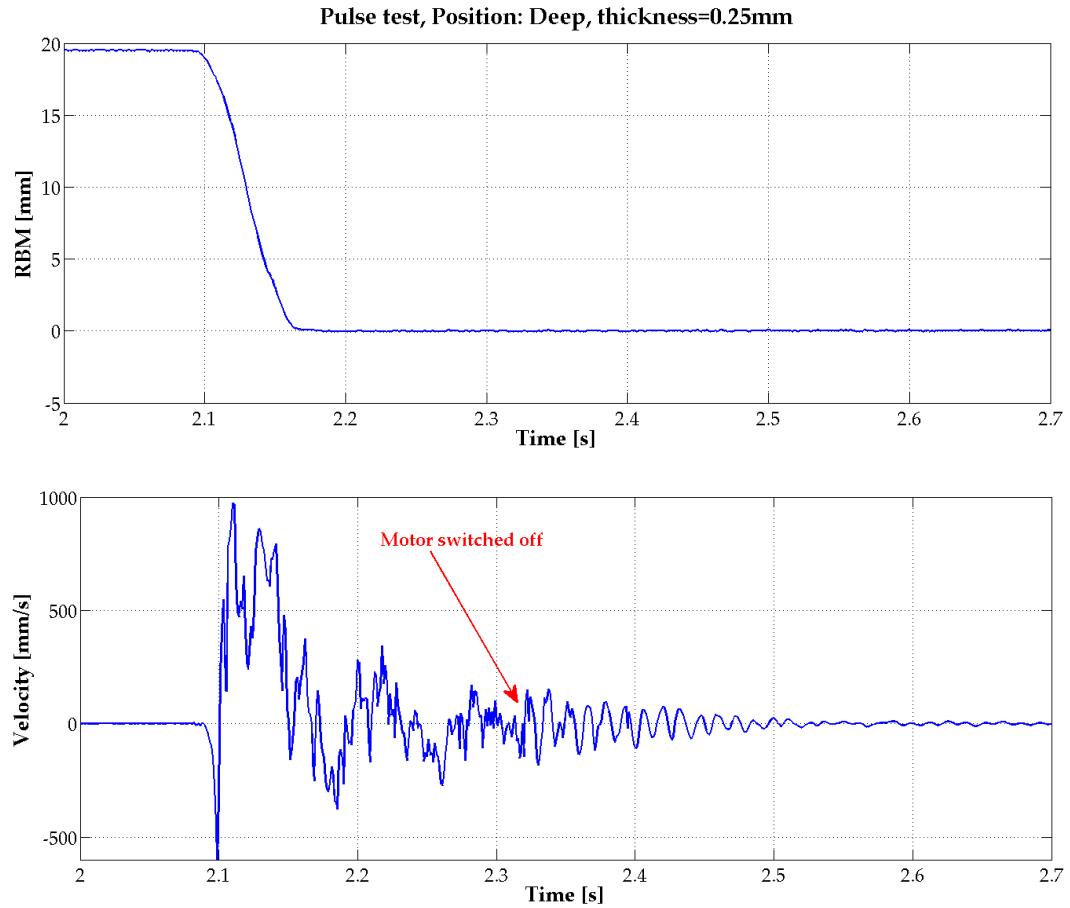


FIGURE 6.21: RBM and velocity measurements for free-vibration test

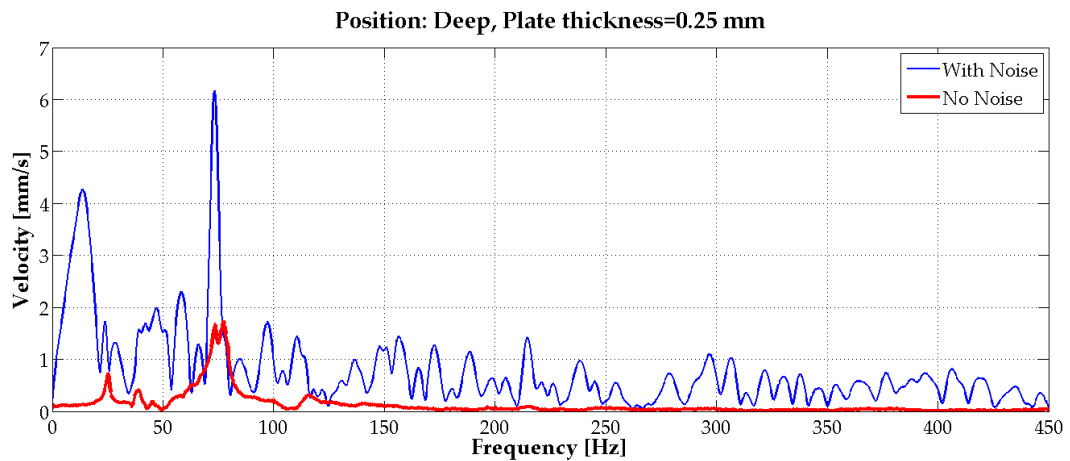


FIGURE 6.22: Response to free vibration test with and without noise included

### 6.4.2 Filtering

The identification of noise that needs to be filtered out from the measurements turned out to be quite a challenging task. Even though, a large number of different types of additional test were conducted, there was not clear indication of specific

	Filter Nr. 1	Filter Nr. 2
Type	FIR	FIR
Order	30	4
Passband Freq [Hz]	12	85
Stopband Freq [Hz]	16	92
Design Method	Least Squares	Least Squares

TABLE 6.4: Characteristics of designed low-pass filters

frequency components that correspond to noise. However, the free vibration tests led to two significant conclusions:

- I The response of the plate that was not affected by noise, included significant contributions by frequency components up to nearly 80 Hz.
- II The effect of noise appeared along the whole range of frequencies.

Using these two points, two different low pass filters were designed to be applied to the LDV signal. The characteristics of the designed filters are presented in Table 6.4.

The choice of cut-off frequency for these two filters were based on two different reasonings. With respect to Filter Nr.1, a small value of cut-off frequency was chosen. Assuming linearity, the response of the plate should include only frequencies included in the excitation (i.e. basic oscillation frequency and its integer multiples). Using Filter Nr.1 for all cases, the basic oscillation frequency and some of its first integer multiples are included and higher frequencies are filtered out. As far as Filter Nr.2 is concerned, all significant frequency components detected in the free vibration response are included in the final signal. These frequencies are expected to appear at the transient response of the plate. The resulted signal are shown in Figure 6.23.

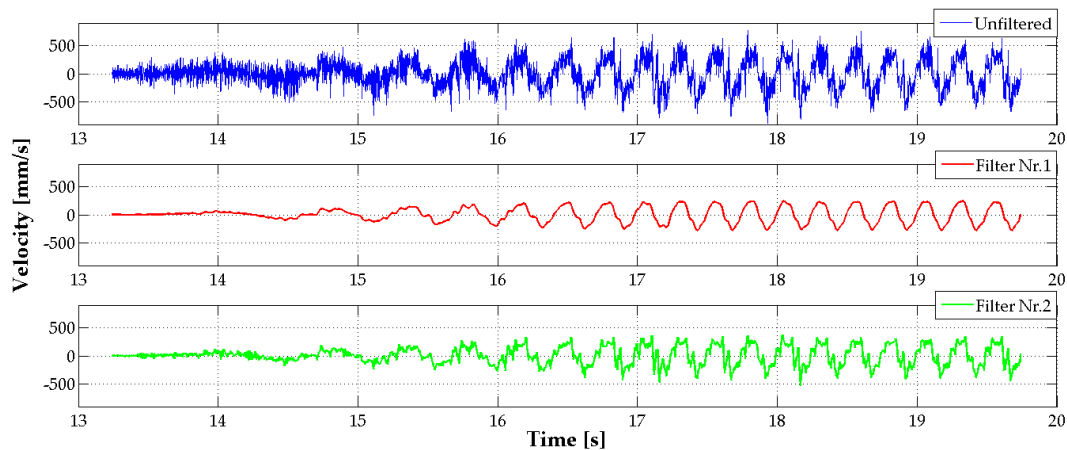


FIGURE 6.23: Raw and filtered LDV measurement

### 6.4.3 Cross-checking between DIC and LDV measurements

The objective of the whole process described above was to determine whether DIC and LDV measurements are compatible. In order to proceed to the comparison, two procedures still need to be done. First, LDV measurements need to be integrated in order to obtain the displacements. For this reason, an integration algorithm using the cumulative trapezoidal rule was applied to the filtered signals.



With respect to DIC measurements, gauge points were positioned in the neighbourhood around the location of the LDV laser spot. One should take into account that the facets corresponding to the laser spot could not be correlated. Time series of the displacements were exported and, then, scaled for correcting the refracted measurements.

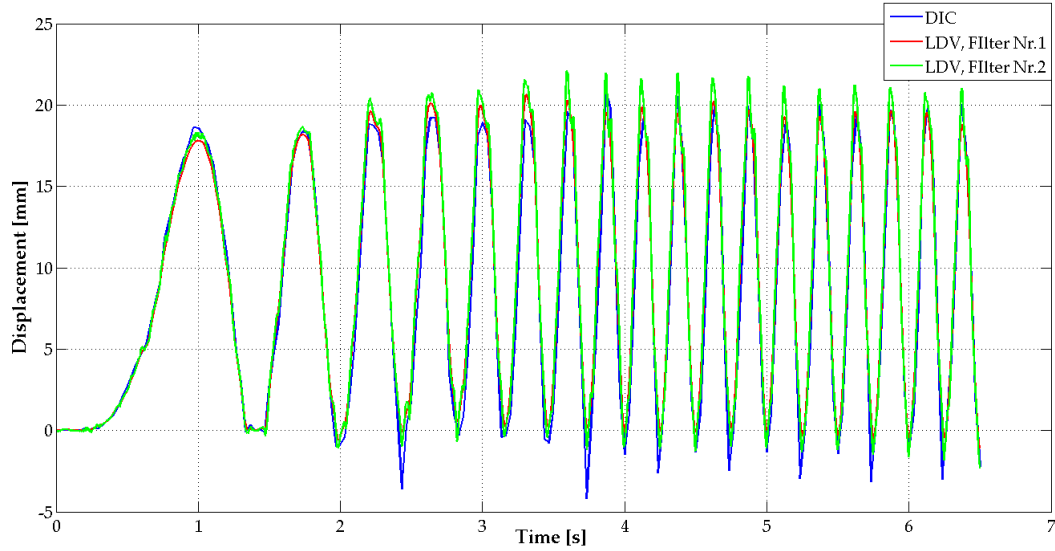


FIGURE 6.24: Displacement comparison between DIC and LDV outputs

Finally, the curves were compared and the quality of fitting for all cases was quantified by the calculation of the Normalized Root Mean Square Deviation (NRMSD). The results reveal that displacements from Filter Nr.2 shows greater fitting to DIC measurements.

Case	Filter Nr.1	Filter Nr.2
Shallow, $f_{osc} = 2$ Hz	11.48%	9.53%
Deep, $f_{osc} = 2$ Hz	9.63%	9.52%
Deep, $f_{osc} = 4$ Hz	15.56%	14.70%
Deep, $f_{osc} = 6$ Hz	22.78%	22.50%

TABLE 6.5: NRMSD between DIC and LDV measurements of total displacements

Using the total displacements, the normalized overall error values show that for cases of lower frequencies (i.e 2 and 4 Hz) the fitting has fair quality. However, as the oscillation frequency gets larger, the error increases as well (Table 6.5).

When the comparison involves the deflections, which are calculated by subtracting the RBM from the total displacements, the error is of the same order of magnitude (Table 6.6).

Case	Filter Nr.1	Filter Nr.2
Shallow, $f_{osc} = 2$ Hz	79.52%	65.96%
Deep, $f_{osc} = 2$ Hz	70.28%	69.44%
Deep, $f_{osc} = 4$ Hz	103.38%	97.64%
Deep, $f_{osc} = 6$ Hz	136.10%	121.59%

TABLE 6.6: NRMSD between DIC and LDV measurements of deflections

## 6.5 Water elevation measurements

Video processing is based on an algorithm that can trace the coordinates of the boundary between white and black regions of a frame. The algorithm had already been developed in the Towing Tank laboratory of TU Delft. The first prerequisite for the employment of the algorithm is that sufficient contrast between water and surrounding air is achieved. For the particular application, lighting needed to be provided for purposes of DIC measurements. The lighting was focused towards the water inside the tank using 2 LED lamps and surrounding lights were switched off. This arrangement by itself created contrast making water bright and air dark. Since priority was given to DIC measurements, further modifications of the set-up, in order to optimize the conditions for surface measurements, were not attempted.



FIGURE 6.25: Video camera placed next to water container and the achieved contrast between water and ambient air

The algorithm that processes the videos uses as input the geometry of water domain. Additionally, a system of coordinates needs to be set. With respect to this system, the coordinates that correspond to the centre of the camera lens as well as the relative angle between the measured geometry and the axis normal to the camera lens, need to be imported. For this particular case the coordinate system was an edge of the container's wooden plate and the axis of the camera was passing through its centre.

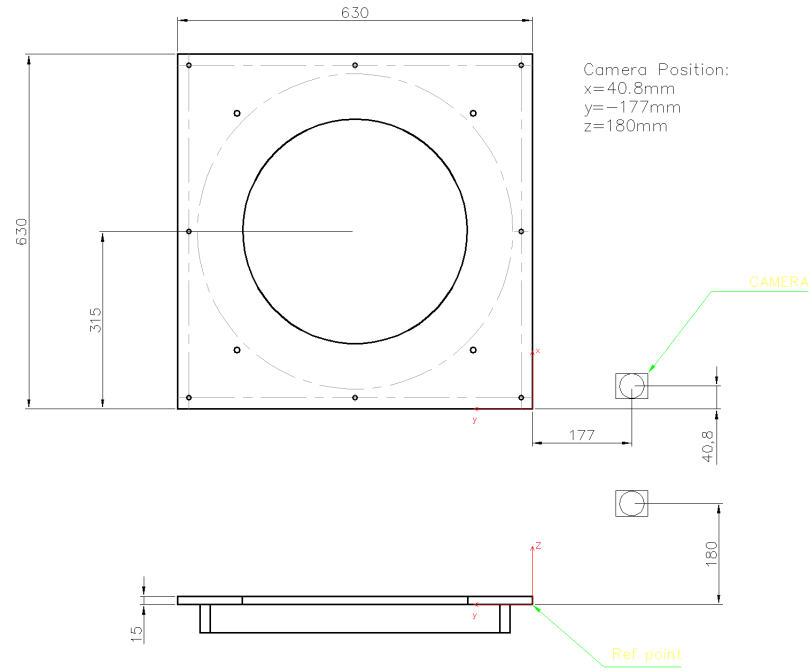


FIGURE 6.26: Sketch indicating the coordinates of video camera

Once the geometry is imported the algorithm can correspond each pixel to a set of 3D coordinates. The next step is to discretize the obtained frames in the horizontal direction by vertical lines on which time series of  $z$ -coordinates of the free surface would be identified at the end. Before this becomes feasible, a Red-Blue-Green (RGB) filter needs to be designed in order to convert the videos to a series of grey-scale frames. The goal is to create a sharp borderline between dark and bright region, which in this case represents the free surface. Since the water domain is symmetric, the water elevation is the same for all the points on the circumference of the free surface. Therefore, to decrease computational cost and increase the efficiency of the RGB filter, a small region of the whole frame was isolated, in order to conduct the measurements.

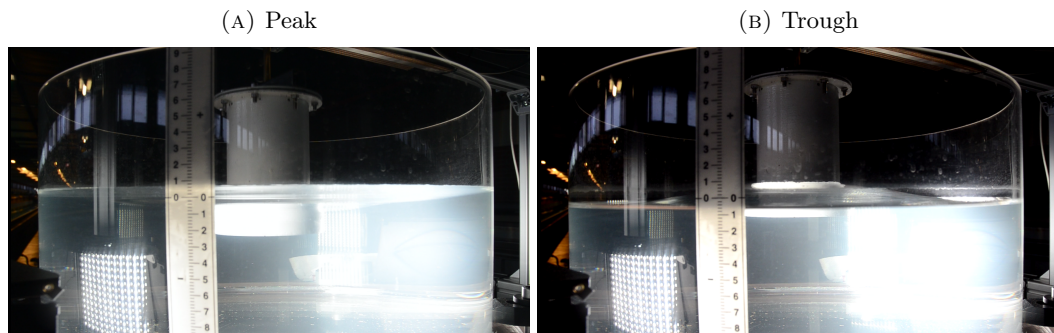


FIGURE 6.27: Snapshots of recorded videos capturing water elevation

Having the videos processed according to the aforementioned steps, the water elevation for a small number of points within a small region of the free surface's circumference was obtained. As expected taking into account symmetry, there was no significant deviation in the measured elevations per time step among different

points. The achieved accuracy reached the value of 0.2 mm. For time steps when the water elevation at the side walls was on its peak, the algorithms faced no problem. However, for steps when the water elevation at the side walls was on its trough, the filter could not identify the elevation at the side walls, due to reflections coming from the inner part of water domain (Fig. 6.27). The resulting time series of surface elevation had the shape seen at Figure 6.28.

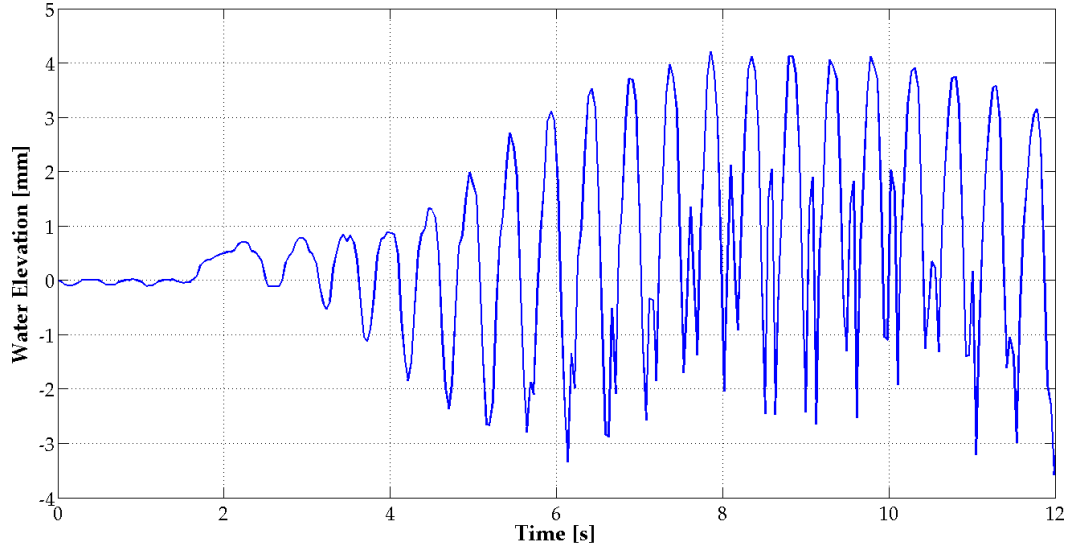


FIGURE 6.28: Measured water elevation for Case Nr. 2

One can observe the problematic behaviour of the results for water elevations that correspond to troughs. Therefore, it was decided to isolate the measurements that correspond to peaks for each oscillation cycle. For cases of oscillation frequency other than 2 Hz, the measured elevations were comparable to the obtained accuracy, thus, it was decided not to be presented. Finally, the measurements of the selected cases were compared to measurements where the plunger's bottom is totally rigid.

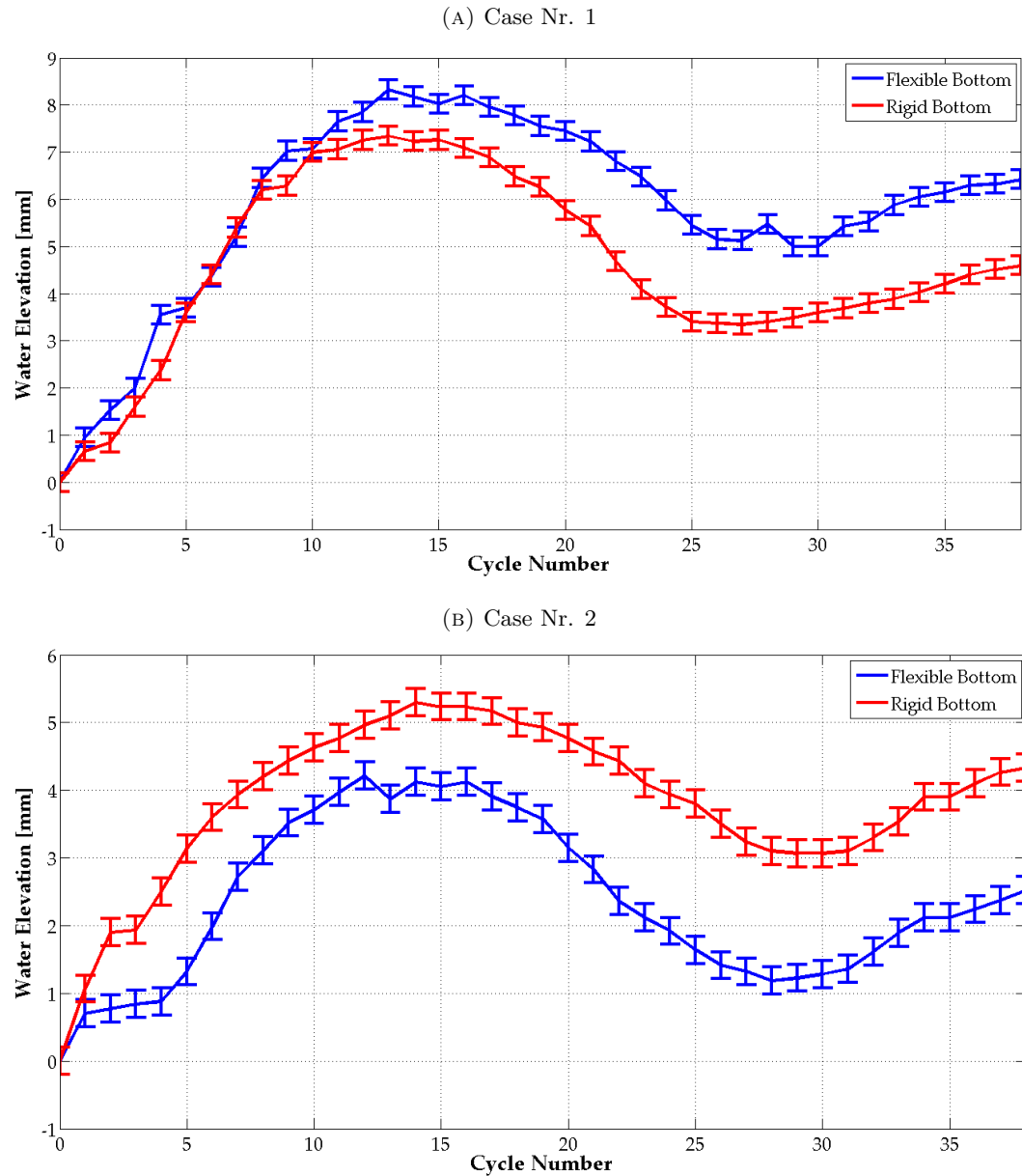


FIGURE 6.29: Measured peaks of water elevation at container's side walls

## 6.6 Summary

In this chapter, the final phase of this project is described. Due to the vast amount of results, only few representative cases were presented. However, before the results were presented, some problem encountered during the execution of experiments are mentioned. Specifically, due to severe sloshing inside the plunger, some cases had to be skipped and, therefore, the experimental matrix had to be slightly modified.

The presentation of results began with measurements obtained by DIC. It has been shown that the measured displacements were affected by refraction and, therefore, they had to be scaled. Apart from the need for scaling, the captured snapshots showed that the fundamental mode shape prevailed. However, there were, also, higher mode shapes encountered less often with much lower magnitude of response.

Proceeding to the LDV results, the unfavourable effects of the linear drive's operation were revealed. Significant amount of noise, was observed even for periods when the plunger was kept still. Analysing the response of the plate in frequency domain, one could see noticeable peaks at integer multiples of the imposed oscillation frequency. Moreover, peaks (comparably smaller) were noticed at very high frequencies  $\sim 400$  Hz. To investigate the reason for these characteristics of response, additional tests were conducted. This new series of experiments included tests with the plunger having a rigid bottom, tests in dry conditions and tests with different PID controller settings of the linear drive. It was concluded that, the peaks at the integer multiples are caused by the imposed rigid body motion. Nevertheless, this conclusion could not give an indication of which frequency components needed to be filtered out. Then, free vibration tests were conducted. The analysed response was split into two parts: one where the oscillator is switch on and one with the oscillator switched off. The comparison between the responses revealed that the noise coming from the oscillator is not restricted within a certain bandwidth. From the latter part of response, peaks were noticed at frequencies up to the region around 80 Hz. Using the last two remarks, two low-pass filters were designed: one with a low ( $12\text{Hz}$ ) and one with higher ( $85\text{Hz}$ ) Hz cut-off frequency. Having the velocity measurements filtered and, then, integrated, the resulting displacements were compared with those measured with DIC. The displacement derived from the second filter showed better fitting for all investigated cases. The deviation between the measurements increased with the oscillation frequency and, therefore, cases of lower  $f_{osc}$  are most reliable to be used for validation. Unfortunately, for all cases the deviations were of the same order of magnitude as the measured deflections.

Finally, water elevation measurements at the side walls, obtained by video processing, were presented. The processing takes advantage of the significant contrast between water and air. This attempt was not fully successful, since troughs could not be measured, due to reflections coming from the inner part of water domain.

## Chapter 7

# Conclusions & Recommendations

### 7.1 Conclusions

The activities described in this thesis are a part of a general effort to develop a accurate and efficient computational tool for modelling FSI. The current thesis was focused on the aspect of accuracy, since its main objective was to produce reliable data for validating such a computational tool. Therefore, a series of experiments was deigned and conducted. The results were processed and analysed in order to evaluate their reliability. The conclusions reached are elaborated below.

#### General remarks for the designed arrangement

To begin with, the designed arrangement fulfilled some of the goals initially stated. According to these goals, the designed experimental arrangement should be of small scale and the involved geometries of fluid and structure domains should be of reduced complexity. The quantities measured, involved the response of PTFE plate, with displacements and velocity by DIC and LDV respectively, and plunger's motion, with RBM and force measurements. However, the designed arrangement was not capable to obtain measurements directly related to fluid field in the region around the flexible structure (i.e. PTFE plate). Therefore, the effect of structure's deflections to fluid's pressure or velocity field could not be investigated. In other words, it can not be verified that a two-way coupled system was created by this arrangement.

#### DIC results

Proceeding to the results, it was directly observed that measurements coming from DIC were affected by refraction. Using the RBM measurements by the laser displacement measurer as reference, a scaling factor was applied to DIC results at each time step. Due to the scaling, the uncertainty of DIC results, which initial was of the order of  $1\mu m$ , is expected to increase. However, the effect of scaling on the measurement error was not quantified. Another observation that is worthwhile to be mentioned, was that mode shapes other than the fundamental were captured by DIC, even though the oscillation frequencies were relatively low. This can partly explained by the fact that the imposed oscillation included, also, higher harmonics, as it was later proved. Additionally, the sloshing modes inside that plunger and the vortices coming from its outer edges induce non-uniformly distributed loads to the flexible plate that may cause higher vibrational mode shapes to appear. Nevertheless, both the inner sloshing modes and the vortices induced by RBM could nt be measured and, therefore, the aforementioned assumption can not be proven.

### LDV results

Analysing the output of LDV, it was noticed that the linear motor used produced significant amount of noise that distorted the measurements. After having the measured response transformed to frequency domain, sharp peaks at integer multiples of the oscillation frequency were detected at all investigated cases. Then, a series of additional tests that included "dry" tests, tests with rigid bottom plate and different PID controller settings was conducted. The results led to the conclusion that the higher harmonics were induced by the linear motor. Therefore, these higher harmonics of smaller amplitude need to be added to the imposed oscillation in the forthcoming numerical experiments. In addition, comparing the results from "dry" and "wet" experiments, the amplitude of response was noticeably higher for the latter within the whole range of frequencies. This indicates that at least one-way coupling was achieved.

### Filtering and cross-checking

The procedure of identifying the noise included, also, free vibration tests. The comparison between responses with the oscillator switched on and off, revealed that noise is not restricted within a specific bandwidth of frequencies. In the response without the effect of noise, significant peaks occurred up to the value of  $80\text{ Hz}$ . Using these remarks, two different low-pass filters were applied to the measurements. Then, both signals were integrated to obtain displacement in order to be compared with DIC results. The measurements filtered with cut-off frequency of  $12\text{ Hz}$  showed worse agreement than the one filtered with cut-off frequency of  $85\text{ Hz}$ . Specifically, for the first case the error with respect to total displacements (including RBM) varied from 9.63 to 22.78% while for the second filter varied from 9.52 to 22.5% (Table 6.5). The overall error increased with the oscillation frequency and, therefore, Case Nr.1 and Nr.2 are the most reliable cases to be used for validation at this stage. However, even for these cases, the values of calculated error with respect to deflections (RBM removed) are considered very high (65.96 and 69.44%). This is attributed to the distortions of the measurements for frequencies within the passband region, caused by noise.

## 7.2 Recommendations for future research

The problems faced, related to the operation of the electromagnetic linear motor and their consequences, create the need to continue the experimental work in order to create data as reliable as possible. The following points refer to improvements that are based to the obtained experience and to additional tasks that were omitted from the current study.

- The overall shape of the experimental arrangement can be kept as it is. But, the possibility of measuring a quantity related to water flow around the flexible plate needs to be investigated. The measurements may give an indication whether plate's deflections distort water's velocity and pressure field (two-way coupling).
- A market survey for an oscillator of different working principle needs to be conducted. The smoothness of imposed motion should be its key feature.



- It would be wiser to design a separate support structure for the oscillator. On one hand, this eliminates the possibility for any mechanical instabilities to distort the measurements of optical instruments. On the other hand, this would make the process of aligning the oscillator with the rest of the arrangement, much more challenging.
- The magnification of error for DIC results due to the required scaling has to be quantified. The possibility of using only a scanning LDV instead of DIC along with single-point LDV needs to be investigated.
- The determination of mechanical properties for the used material (i.e. PTFE) requires more meticulous testing. The mechanical properties of PTFE can vary significantly for different stress rates, humidity levels, temperature and, of course, production processes that affect the crystalline structure. Before proceeding to the experiments it must be ensured, that for the expected conditions, neither creep nor plastic deformations are to occur.
- Once the actual mechanical properties are defined, free vibration tests in air should be conducted. Comparing the prevailing frequency components in the response (i.e. natural frequencies) with the calculated natural frequencies using analytical expression found in literature, would determine whether the fixed boundary condition is applied successfully.
- Finally, it was established that even for the lowest amplitude of oscillation the plate's response was significant (Table 6.2). Therefore, imposed oscillations of lower amplitude would give the possibility to test higher oscillation frequencies that may approach at least the first natural frequency. Also, maximum deflections would be comparable to RBM and so would be the respective induced distortions in the fluid field.



# Bibliography

- Aarsnes, J.V. (1994). *An experimental investigation of the effect of structural elasticity on slamming loads and structural response. Texhcnical Report*. MARINTEK A/S, Trondheim, Norway.
- Amabili M., Dalpiaz G. (1998). “Vibrations of Base Plates in Annular Cylinder Tanks: Theory and Experiments”. In: *Journal of Sound and Vibration* 210, pp. 329–350. DOI: [10.1006/jsvi.1997.1280](https://doi.org/10.1006/jsvi.1997.1280).
- Askari E. Jeong K.H., Amabili M. (2013). “Hydroelastic vibration of circular plates immersed in a liquid-filled container with free surface”. In: *Journal of Sound and Vibration* 332, pp. 3064–3085.
- Bereznitski A., Kaminski M.L. (2002). “Practical Implications of Hydroelasticity in Ship Design”. In: *ISOPE Conference, Kitakyushu, Japan*.
- Berkovic, G. and E. Shafir (2012). “Optical methods for distance and displacement measurements”. In: *Advances in Optics and Photonics* 4 (4), pp. 441–471. DOI: [10.1364/AOP.4.000441](https://doi.org/10.1364/AOP.4.000441).
- Bredmose, H. et al. (2013). “Dynamic Excitation of Monopiles by Steep and Breaking Waves. Experimental and Numerical Study”. In: *32nd International Conference on Ocean, Offshore and Arctic Engineering, ASME*. URL: <http://proceedings.asmedigitalcollection.asme.org/ConferenceProceedings.aspx>.
- Brugo T. Panciroli R., Minak G. (2012). *Study of the Dynamic Behavior of Plates Immersed in a Fluid*. IMEKO TC15 - Experimental Mechanics - Proceedings of the 11th Youth Symposium on Experimental Solid Mechanics, Brasov, Romania.
- Chaplin, J. R., R. C. T. Rainey, and R. W. Yemm (1997). “Ringing of a vertical cylinder in waves”. In: *Journal of Fluid Mechanics* 350, pp. 119–147. ISSN: 1469-7645. DOI: [10.1017/S002211209700699X](https://doi.org/10.1017/S002211209700699X).
- Chen, F., M. Brown, and M. Song (2000). “Overview of Three-Dimensional Shape Measurement Using Optical Methods”. In: *Optical Engineering* 39 (1), pp. 10–22. DOI: [10.1117/1.60438](https://doi.org/10.1117/1.60438).
- Chiba, M (1992). “Nonlinear Hydroelastic Vibration of a Cylindrical Tank With an Elastic Bottom, Containing Liquid. Part I: Experiment”. In: *Journal of Fluids and Structures* 6, pp. 181–206.
- Faltinsen, O. M. (1999). “Ringing Loads on a Slender Vertical Cylinder of General Cross- Section”. In: *Journal of Engineering Mathematics* 35, pp. 199–217. ISSN: 1573-2703. DOI: [10.1023/A:1004362827262](https://doi.org/10.1023/A:1004362827262).
- Faltinsen, O. M., J. N. Newman, and T. Vinje (1995). “Nonlinear wave loads on a slender vertical cylinder”. In: *Journal of Fluid Mechanics* 289, pp. 179–198. ISSN: 1469-7645. DOI: [10.1017/S0022112095001297](https://doi.org/10.1017/S0022112095001297).
- Faltinsen, O.M. (1997). “The effect of Hydroelasticity on Ship Slamming”. In: *Philosophical Transactions: Mathematical, Physical and Engineering Sciences* 355.1724, pp. 575–591. URL: <http://www.jstor.org/stable/54676>.
- Faltinsen, O.M., M. Greco, and Landrini M. (2002). “Green Mater Loading on a FPSO”. In: *Journal of Offshore Mechanics and Arctic Engineering* 124.2, pp. 97–103. DOI: [10.1115/1.1464128](https://doi.org/10.1115/1.1464128).
- Frei S. Richter T., Wick T. (2015). *Numerical Mathematica and Advanced Applications - ENUMATH 2013*. ISBN 978-3-319-10705-9: Springer, pp. 745–753.

- Gatzhammer, B. (2008). *A Partitioned Approach for Fluid-Structure Interaction on Cartesian Grids*. Technische Universitat Munchen.
- Gene H. Wang J., Layton A. (2012). "Numerical Methods for Fluid-Structure Interaction- A Review". In: *Global-Science Press* 12, pp. 337–377. DOI: [10.4208/cicp.291210.290411s](https://doi.org/10.4208/cicp.291210.290411s). URL: <http://www.global-sci.com>.
- Haddara M.R., Cao S. (1996). "A Study of the Dynamic Response of Submerged Rectangular Flat Plates". In: *Marine Structures* 9, pp. 913–933.
- Helfrick, M. N. et al. (2011). "3D Digital Image Correlation Methods for Full-Field Vibration Measurement". In: *Mechanical Systems and Signal Processing* 25 (3), pp. 917–927. DOI: [10.1016/j.ymssp.2010.08.013](https://doi.org/10.1016/j.ymssp.2010.08.013).
- Herbst, C. and K. Splitthof. *Basics of 3D Digital Image Correlation*. Dantec Dynamics GmbH.
- Hirdaris S.E., Ge C. (2005). *Review and Introduction to Hydroelasticity of Ships*. Lloyd's Register Technical association, Paper No.8.
- Koo W., Kim J.D. (2015). "Simplified formulas of heave added mass coefficients at high frequency for various two-dimensional bodies in finite water depth". In: *Int J. Nav. Archit. Ocean Eng.* 7, pp. 115–127. ISSN: 2092-6782. DOI: <http://dx.doi.org/10.1515/ijnaoe-2015-0009>.
- Leissa, A.W. (1969). *Vibration of Plates*. SP-160: NASA.
- Michler C. Hulshoff S.J., Brummelen E.H. van Borst R. de (2003). *A monolithic approach to fluid-structure interaction*. Faculty of Aerospace Engineering, Delft University of Technology, The Netherlands.
- PolytecGmbH (2003). *Vibrometer Single Point Sensor Head OFV-505/-503, User Manual*.
- Richter, T. (2010). *Numerical Methods for Fluid-Structure Interaction Problems*. Heidelberg.
- Rizos (2016). *Numerical Modelling of an Experimental Set Up Proposed for the Study of the Fluid - Structure Interaction Problem Using foam-extend-3.1*. Research Exercise, TU Delft.
- Rodriguez, C.G. et al. (2010). *Experimental Modal Analysis in Submerged Cantilever Plates with Nearby Rigid Wall*. International Conference on Noise and Vibration Engineering.
- Ryzhakov P.B. Rossi R., Idelsohn S.R. Ofiate E. (2010). "A monolithic Lagrangian approach for fluid-structure interaction problems". In: 46, pp. 883–899. DOI: [10.1007/s00466-010-522-0](https://doi.org/10.1007/s00466-010-522-0).
- Timoshenko S., Woinowsky-Krieger S. (1989). *Theory of Plates and Shells*. ISBN 0-07-064779-8: McGraw-Hill.
- Tromans, P., C. Swan, and S. Masterton (2006). *Nonlinear potential flow forcing: the ringing of concrete gravity based structures*. Ocean Wave Engineering Ltd, Health and Safety Executive UK. URL: <http://www.hse.gov.uk/research/rrhtm/rr468.htm>.
- Tuitman, J.T. (2010). *Hydro-elastic Response of Ship Structures to Slamming Induced Whipping*. Den Haag.
- Vu V.H. Thomas M., Lakis A.A. Marcouiller L. (2007). *Effect of Added Mass on Submerged Vibrated Plates*. Department of Mechanical Engineering, École de Technologie Supérieure, Montréal, Canada.
- Westergaard H.M., Slater W.A. (1921). *Moments And Stresses In Slabs*. Washington, D.C.: National research council.
- Yigit S. Stenel D.C., Schäfer M. (2007). "Efficiency of fluid-structure interaction simulations with adaptive underrelaxation and multigrid acceleration". In: *The International Journal of Multiphysics* 1.1, pp. 85–99. DOI: [10.1260/175095407780130535](https://doi.org/10.1260/175095407780130535).

## Appendix A

# Pre-estimation of required oscillating force

Due to the wide range of available oscillators and load cells, preliminary calculations of the expected oscillating force were required. This way, the selection of equipment with unnecessarily high capacity, that would lead to lower accuracy, could be avoided.

To estimate the required force, the oscillated plunger was modelled as a totally rigid cylinder imposed to forced heave motion. The equation of motion for this system is the following:

$$(m + a_{33}(\omega)) \cdot \ddot{z}(\omega, t) + b_{33}(\omega) \cdot \dot{z}(\omega, t) + c_{33} \cdot z(\omega, t) + W - B = f_{osc}(\omega, t) \quad (\text{A.1})$$

Where,

- $m$  is the structural mass of the plunger including the water inside
- $a_{33}(\omega)$  is the added mass coefficient for the heave motion
- $b_{33}(\omega)$  is the damping coefficient for the heave motion
- $c_{33}$  is the restoring coefficient for the heave motion
- $z(\omega, t) = Z \cos(\omega t)$  is the imposed vertical motion
- $W$  is the plunger's weight
- $B$  is buoyancy at initial position
- $f_{osc}(\omega, t) = F \cos(\omega t + \phi_{fz})$  is the imposed oscillating force with  $\phi_{fz}$  to be the phase angle between force and displacement.

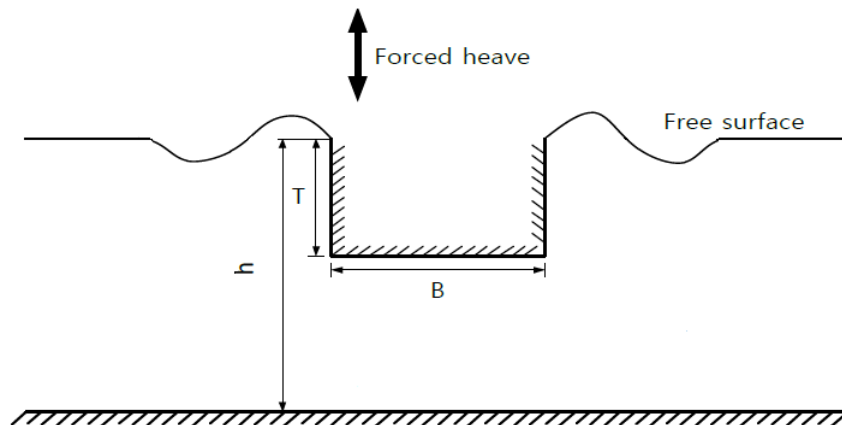


FIGURE A.1: Presentation of plunger's section geometry (reproduced from Koo W. (2015))

Having its expression formulated, the calculation of the force relies on the definition of added mass, damping and restoring coefficients. Beginning with the easiest

one, the restoring coefficient in heave depends, only, on the water-plane area of the structure:  $c_{33} = \rho g A_{WL}$ .

On the contrary, the estimation of added mass and damping coefficients need more complex treatment. The process involved the discretization of the cylinder to rectangle cross sections of infinitely small thickness and variable width. First, the dimensionless coefficients were calculated for each section, taking into account the ration of depth over draught ( $h/T$ ) (Fig. A.1) and, then, by integration the added mass and damping of the whole structure was approximated.

The basis for the calculation of dimensionless coefficients was obtained by results presented by Koo W. (2015). With respect to damping, results were obtained by extrapolating and interpolating the values shown in Figure A.2 for  $h/T = 6$  ("Shallow" case) and  $h/T = 2$  ("Deep" case) respectively.

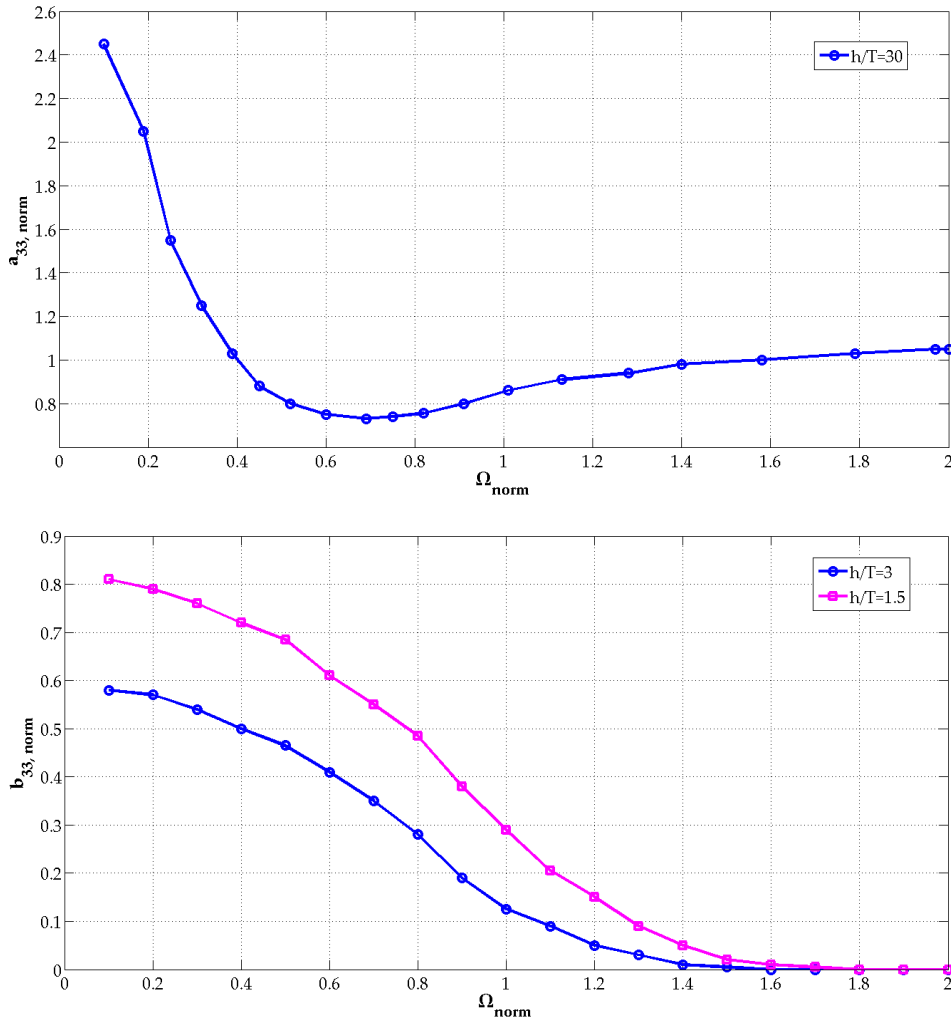


FIGURE A.2: Dimensionless coefficients for added mass and damping

For added mass, the values that correspond to deep water situation ( $h/T = 30$ ) presented in Figure A.2, were scaled by a factor that depends on the ratios:  $\xi = h/T$ , and  $\psi = B/T$ . The scaling factor  $SF$  is given by the following formula.

$$SF = C_1 + C_2\psi + C_3\xi + C_4\psi\xi + C_5\xi^2 + C_6\psi\xi^2 + C_7\xi^3 + C_8\psi\xi^3 + C_9\xi^4 + C_{10}\psi\xi^4 + C_{11}\xi^5$$

Where,

$C_1$	$C_2$	$C_3$	$C_4$	$C_5$	$C_6$	$C_7$	$C_8$	$C_9$	$C_{10}$	$C_{11}$
5.373	1.711	-7.022	-1.399	4.015	0.4303	-1.052	0.0578	0.1287	0.00284	-0.00595

The aforementioned process is described in detail by Koo W. (2015). Once the coefficients of added mass and damping for all cross sections was calculated, the total values were obtained applying numerical integration. The resulting values were plunged in equation of motion. The results are summarized in the following figures.

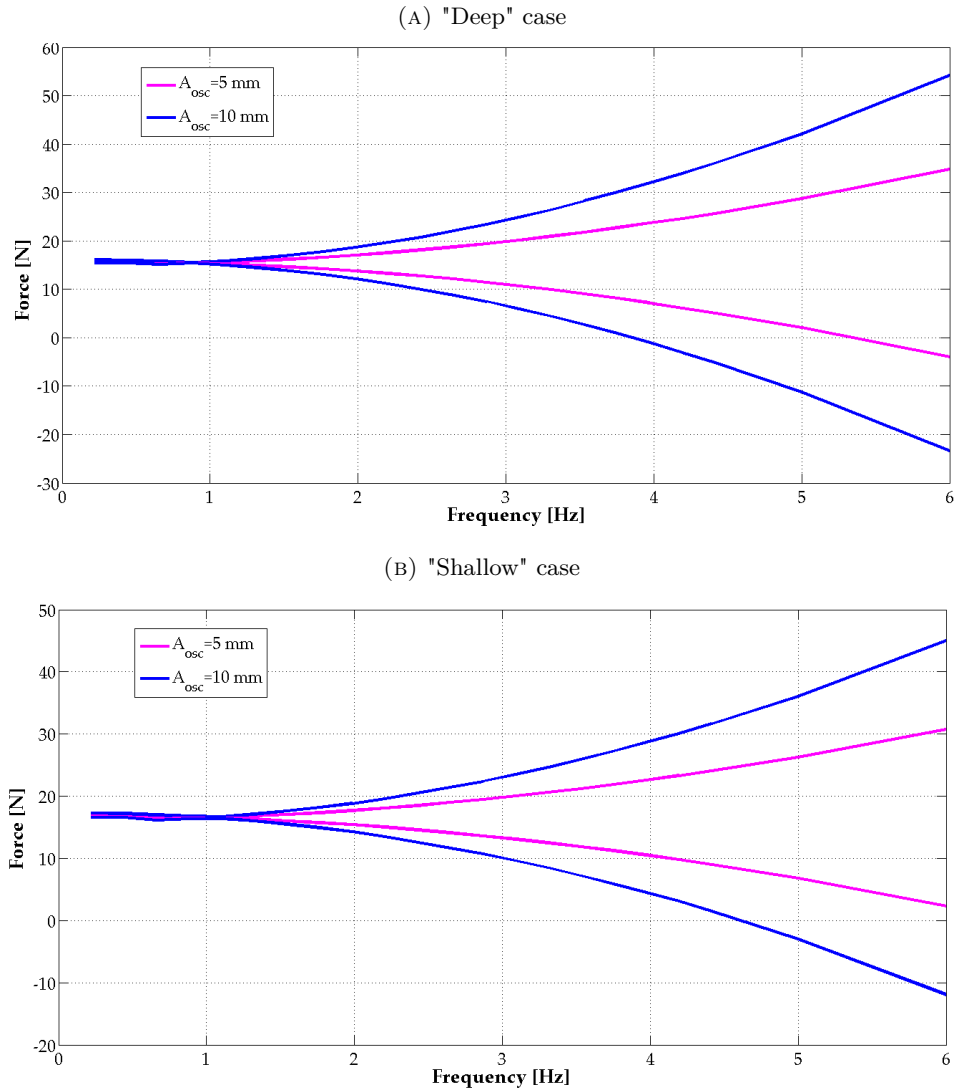


FIGURE A.3: Envelopes of required oscillation force





## Appendix B

# Definition of material properties

In order to reproduce the experiments in a FSI numerical simulator, the mechanical properties of the flexible structure need to be imported. Available handbooks indicate a range of values for the density and Young's modulus of PTFE. The actual values of properties for the used material need to be determined experimentally.

With respect to density, a piece of PTFE plate of measured dimensions was weighed. The results are summarised at Table B.1.

Property	Value	Uncertainty	Unit
Length	938.5	$\pm 0.500$	mm
Width	705.0	$\pm 0.500$	mm
Thickness	0.500	$\pm 0.050$	mm
Mass	0.780	$\pm 0.005$	kg
Density	2359	$\pm 28.08$	$kg/m^3$

TABLE B.1: Properties of specimen used to determine the density

For the definition of Young's Modulus cyclic tensile tests of PTFE specimens were conducted. In order to approximate the actual conditions as possible, the specimens were painted and kept in water before tested.



FIGURE B.1: PTFE specimen clamped with a digital extensometer attached

The imposed strain ranged from 0.2% to 0.4% with rate of 1  $mm/s$ . To avoid buckling, the specimens were preloaded with 10 N of tensile load.

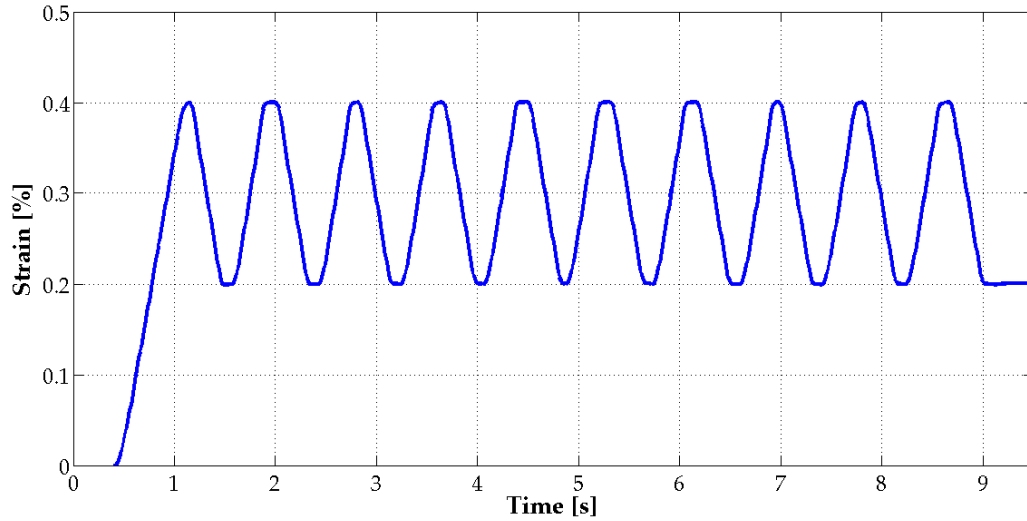


FIGURE B.2: Time series of strain during cyclic loading tests

Using the obtained measurements of stresses and strains for three tested specimens, values of the Young's Modulus per cycle were calculated.

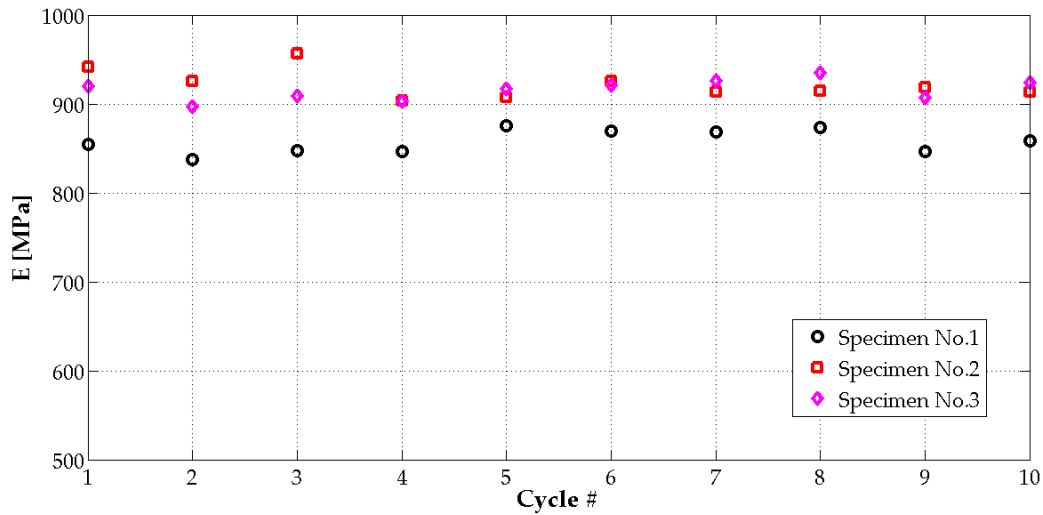


FIGURE B.3: Calculated Young's Modulus for three specimens per load cycle

Using the results presented in Figure B.3, the plate's Young's Modulus is approximated with the following values.

$$E[MPa] = 884.91 \pm 50.35$$

## Appendix C

# Calculation of dry natural frequencies

Once the mechanical properties of the PTFE plate used were approximated experimentally, the dry natural frequencies of specimens for fully clamped boundary conditions were calculated.

The decrease of natural frequencies due to added mass effects is expected to be different for each mode shape but was not pre-estimated for the current study. Askari et al. (2013) has investigated the impact of added mass to the natural frequencies of fully submerged circular plates. The decrease varied from 28% to 55%. However, the geometry of the experimental arrangement in the study of Askari et al. differs compared the one of the current study. Therefore, the results could not be applied directly, but they just gave an indication of values expected for "wet" natural frequencies.

The analytical formula used for the calculation of "dry" natural frequencies (Leissa, 1969).

$$f_n = \frac{\lambda_{kn}^2}{2\pi R^2} \sqrt{\frac{Et^3}{12(1-\nu^2)\rho_s t}} \quad (\text{C.1})$$

$\lambda_{nk}$  are the dimensionless natural frequencies. Their values for n (angular nodes) and k (radial nodes) are given in Table C.1. For fixed boundaries,  $\lambda_{kn}$  is not dependent to the Poisson's ratio.

<b>k</b>	<b>n = 0</b>	<b>n = 1</b>	<b>n = 2</b>	<b>n = 3</b>
<b>1</b>	10.2158	21.2609	34.8770	51.0334
<b>2</b>	39.7711	60.8287	84.5837	111.0214
<b>3</b>	89.1041	120.0792	153.8151	190.3038
<b>4</b>	158.1842	199.0534	242.7285	28901799

TABLE C.1: Values of  $\lambda_{kn}^2$  for different modes (Leissa, 1969)

The results are summarized in the following table.

<b>thickness [mm]</b>	<b>Mode Shapes</b>							
	<b>(0,1)</b>	<b>(1,1)</b>	<b>(1,2)</b>	<b>(0,2)</b>	<b>(1,3)</b>	<b>(2,1)</b>	<b>(3,1)</b>	<b>(3,0)</b>
<b>0, 50</b>	101	210	345	394	505	602	838	883
<b>0, 25</b>	50	105	173	197	253	301	419	441

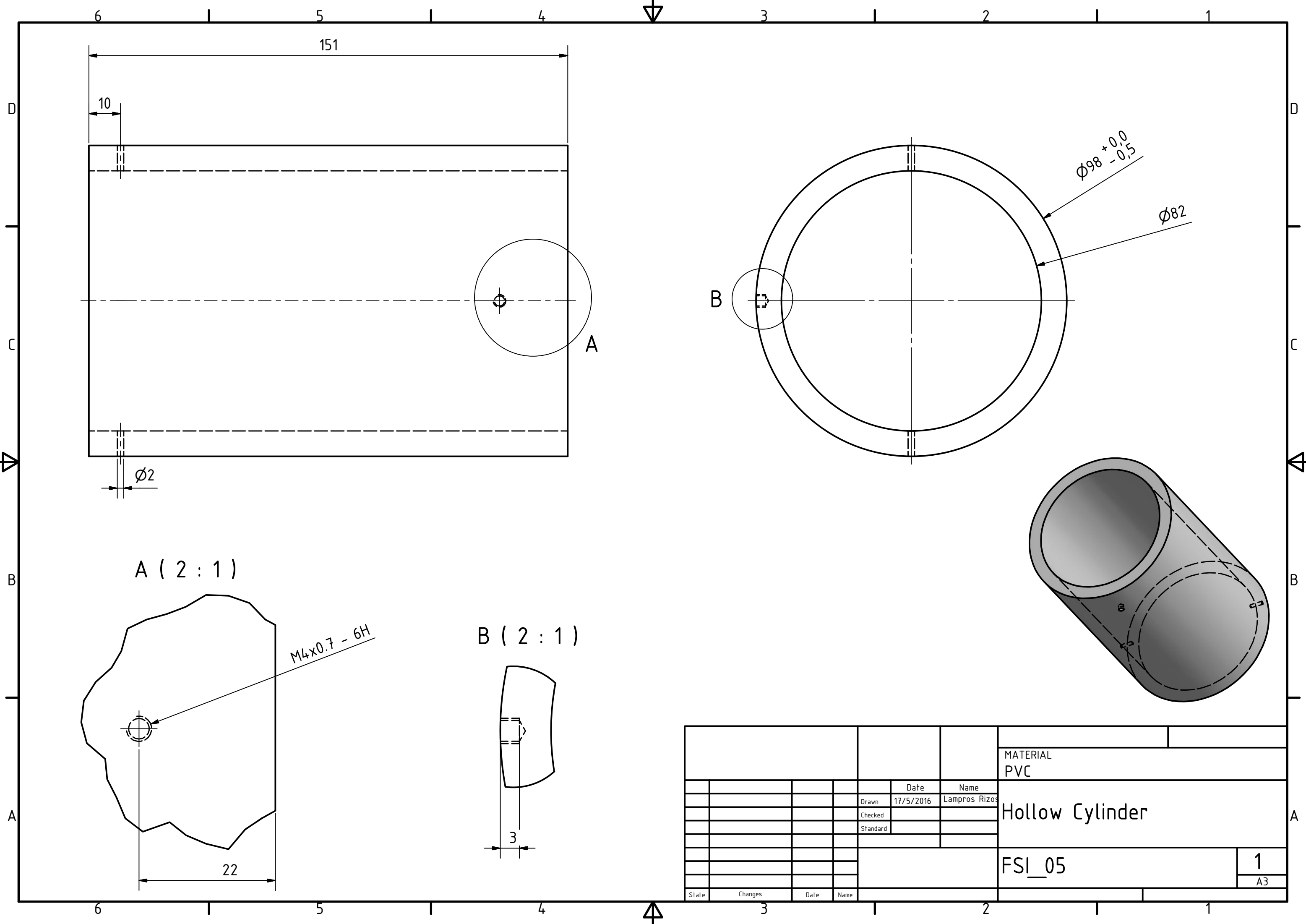
TABLE C.2: Dry natural frequencies fully clamped PTFE plates

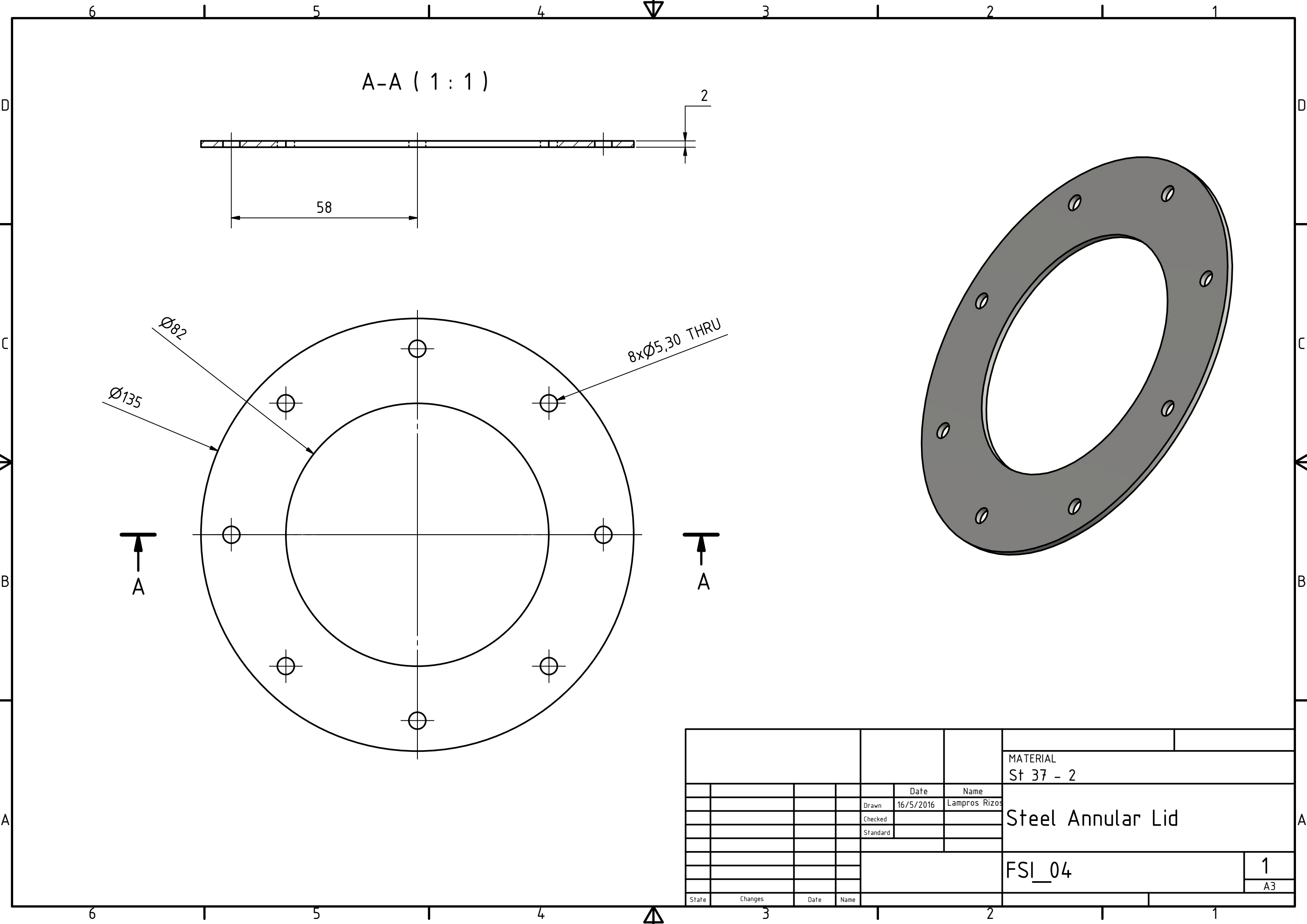


## Appendix D

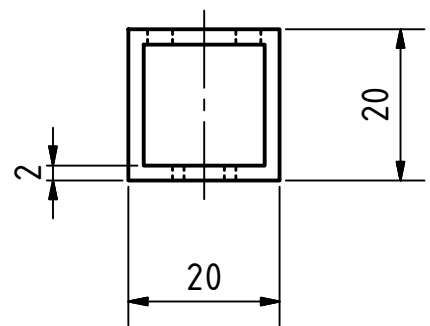
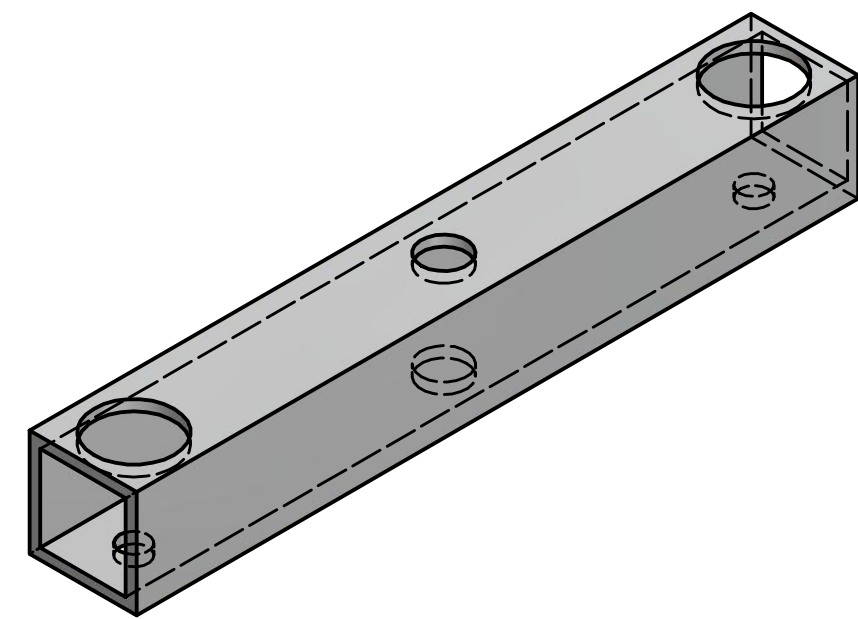
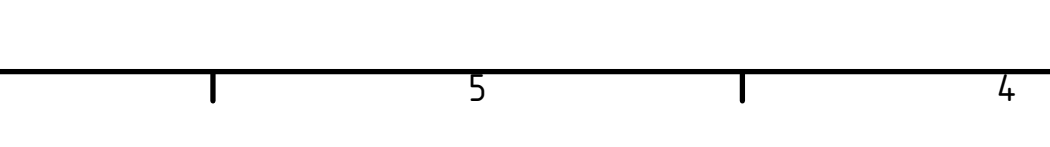
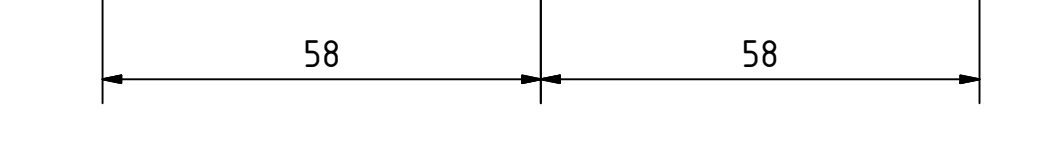
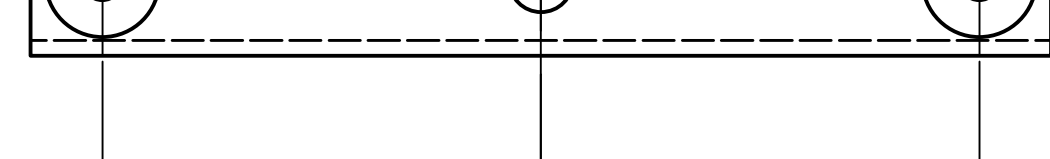
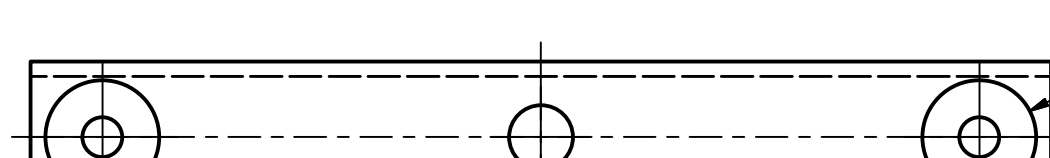
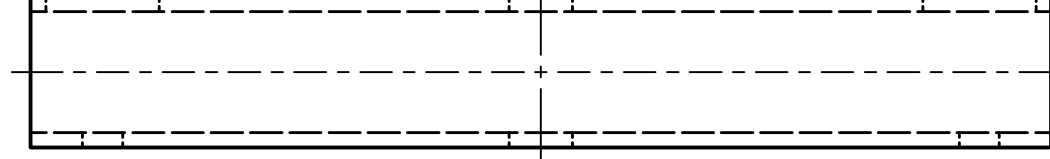
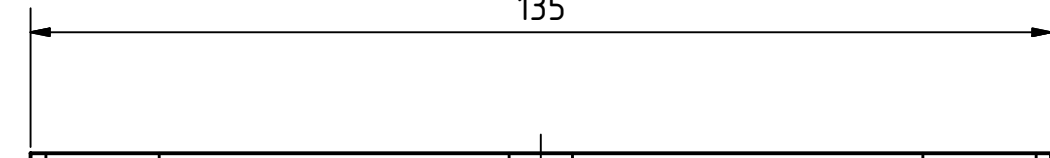
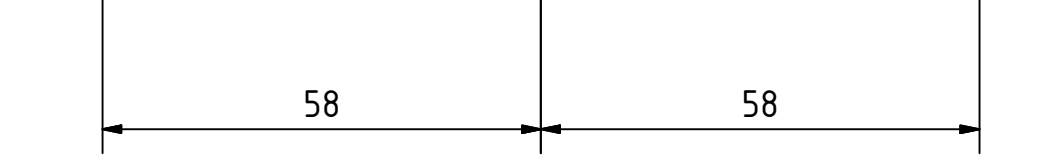
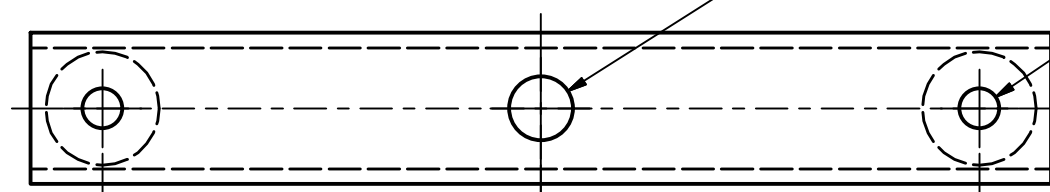
# Detailed designs of fabricated structures



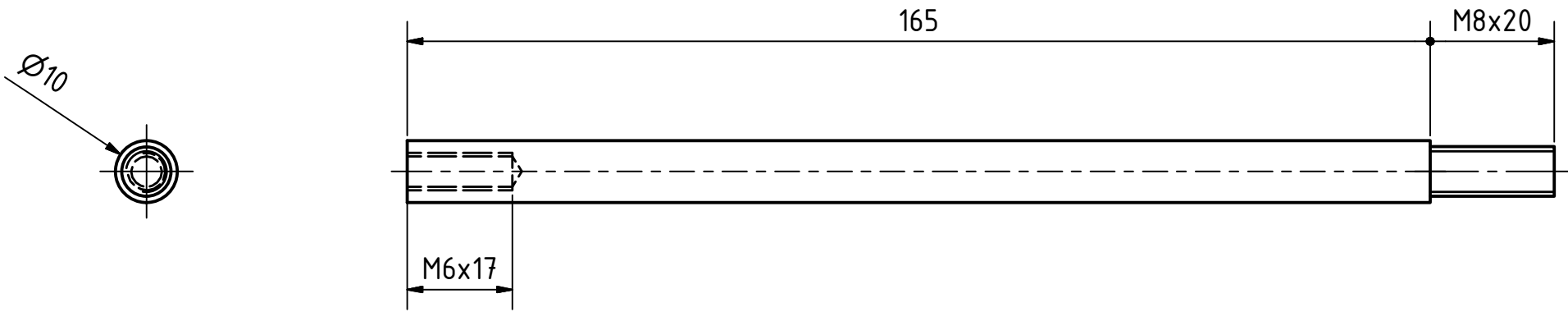
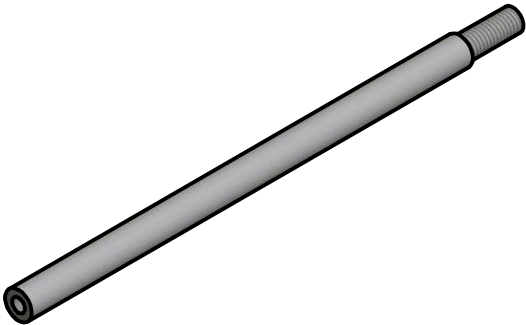




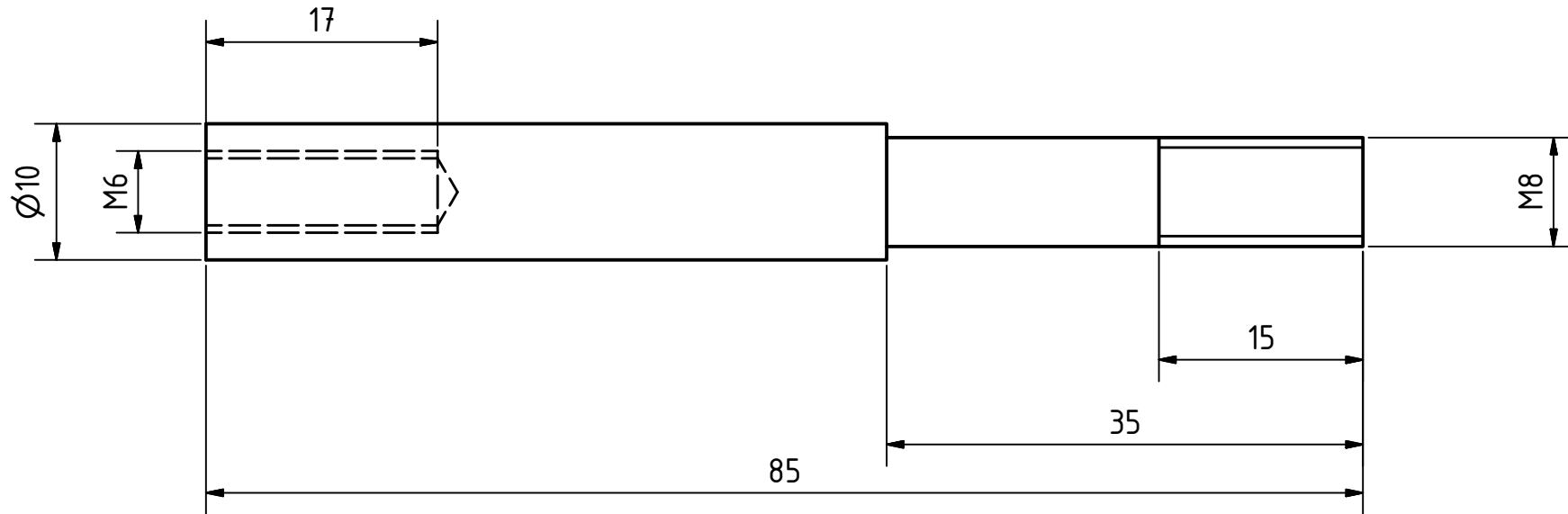
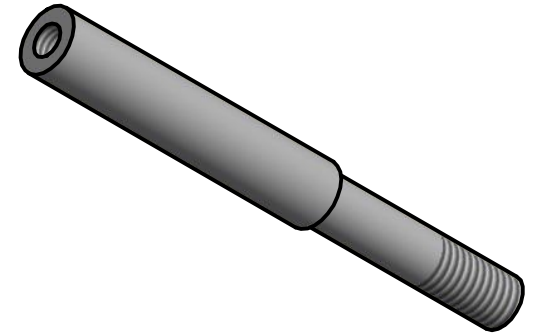




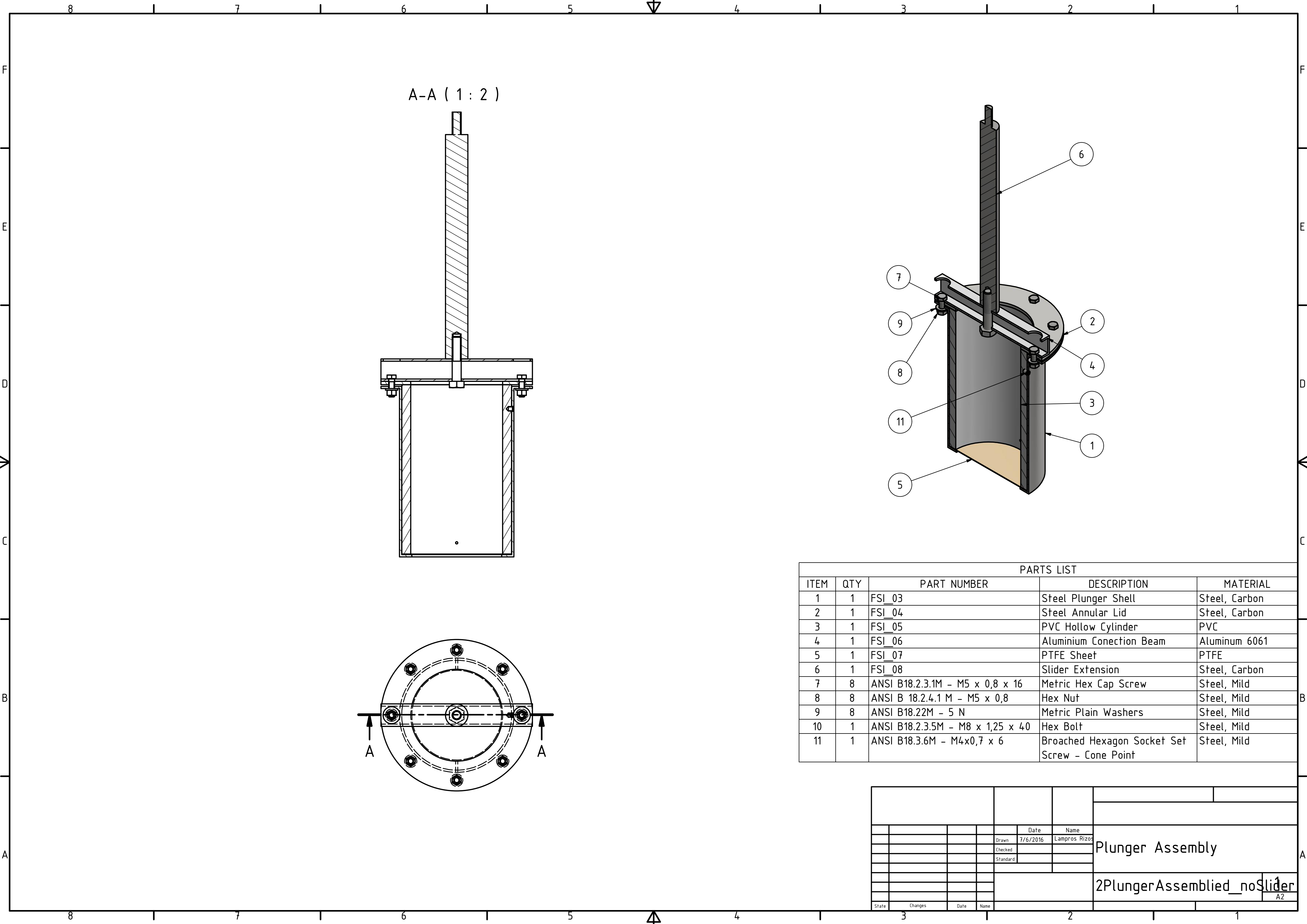
								MATERIAL Aluminium			
					Date	Name	Connection beam				
				Drawn	7/6/2016	Lampros Rizos					
				Checked							
				Standard							
							FSI_06				1
											A3
State	Changes			Date	Name						



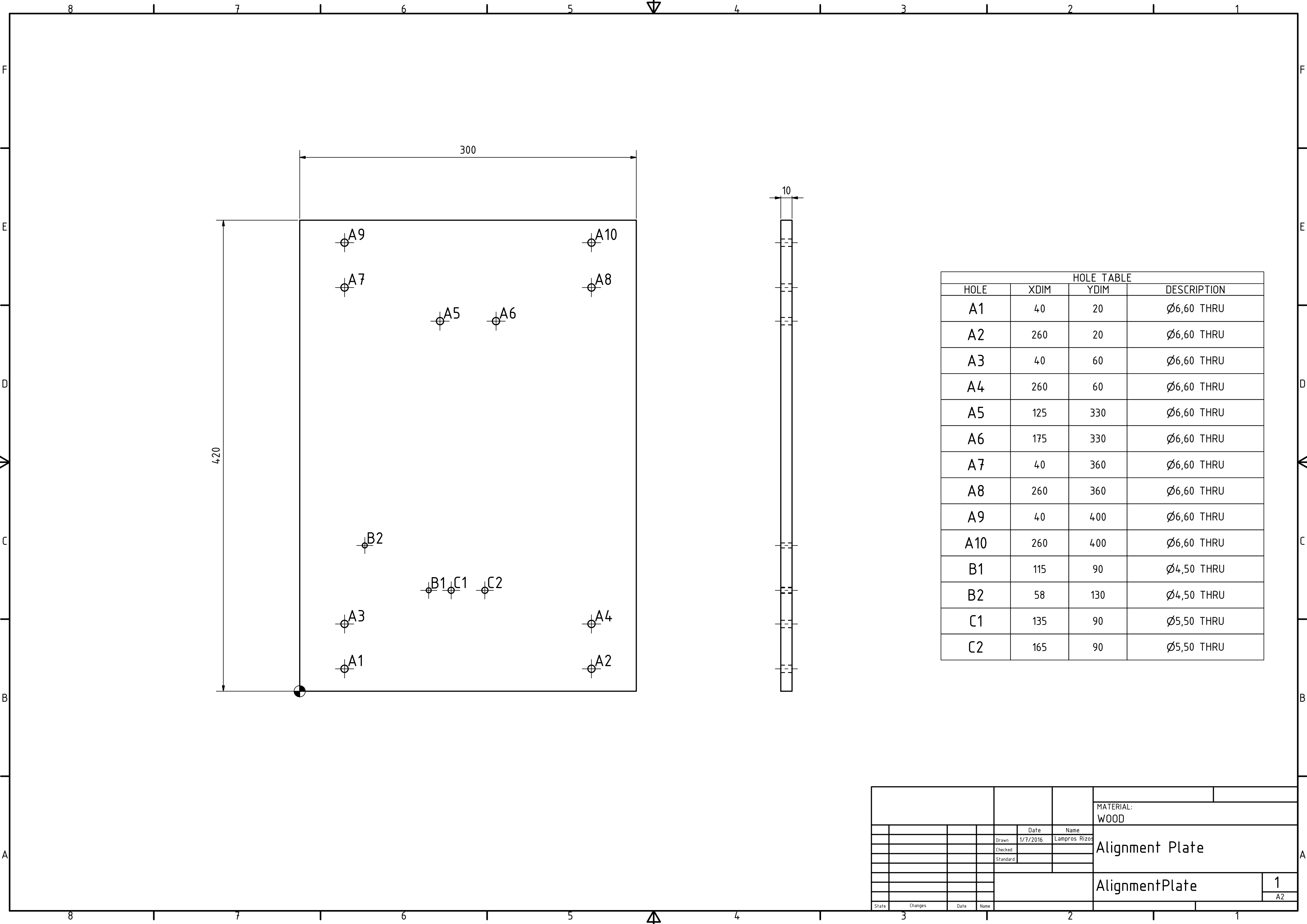
								MATERIAL	
								St. 37	
					Date	Name		Extension Rod	
				Drawn	1/7/2016	Lampros Rizos			
				Checked					
				Standard					
								extensionRod	
State	Changes		Date	Name					



								MATERIAL: St. 37-2		
				Date	Name	Load Cell Adapter				
				Drawn	30/6/2016					Lampros Rizos
				Checked						
				Standard						
							LoadCellAdapter		1	
							A4			
State	Changes	Date	Name							

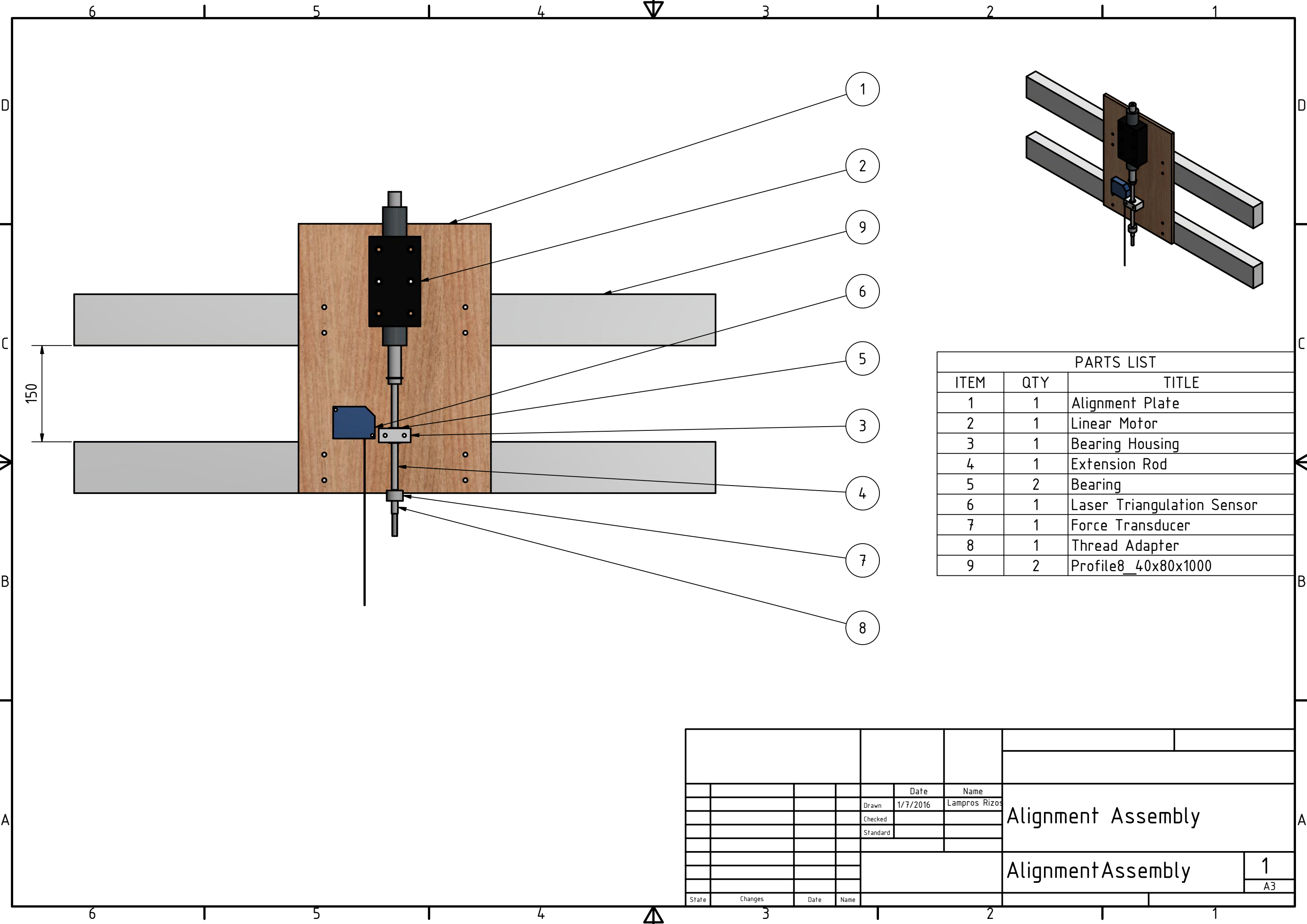


					Date	Name	Plunger Assembly				
				Drawn	7/6/2016	Lampros Rizos					
				Checked							
				Standard							
							2PlungerAssembled_noSlider				
State	Changes	Date	Name				A2				



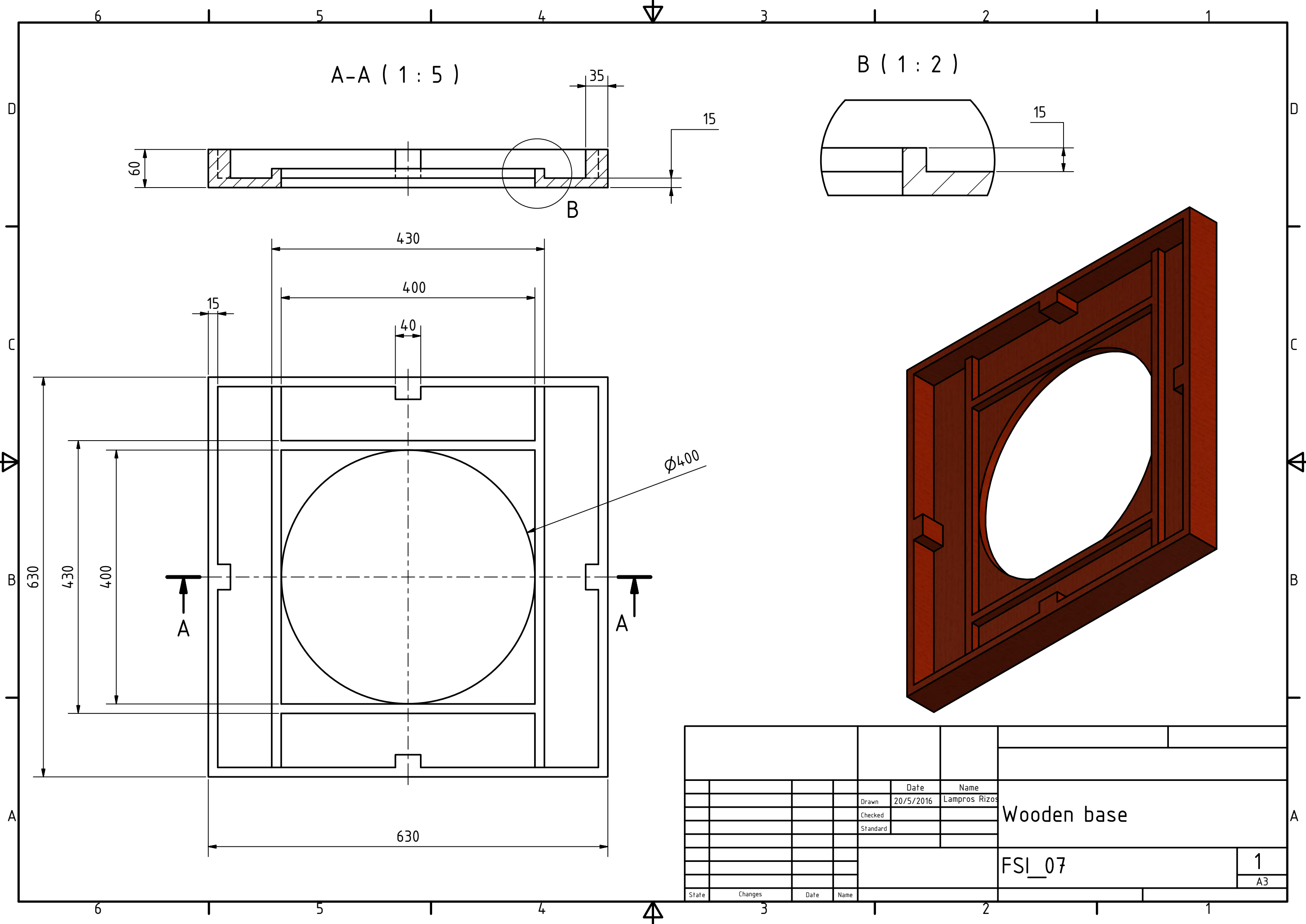
HOLE TABLE			
HOLE	XDIM	YDIM	DESCRIPTION
A1	40	20	Ø6,60 THRU
A2	260	20	Ø6,60 THRU
A3	40	60	Ø6,60 THRU
A4	260	60	Ø6,60 THRU
A5	125	330	Ø6,60 THRU
A6	175	330	Ø6,60 THRU
A7	40	360	Ø6,60 THRU
A8	260	360	Ø6,60 THRU
A9	40	400	Ø6,60 THRU
A10	260	400	Ø6,60 THRU
B1	115	90	Ø4,50 THRU
B2	58	130	Ø4,50 THRU
C1	135	90	Ø5,50 THRU
C2	165	90	Ø5,50 THRU

								MATERIAL: WOOD			
					Date		Name	Alignment Plate			
				Drawn	1/7/2016		Lampros Rizos				
				Checked							
				Standard							
								AlignmentPlate		1	A2
State	Changes	Date	Name								

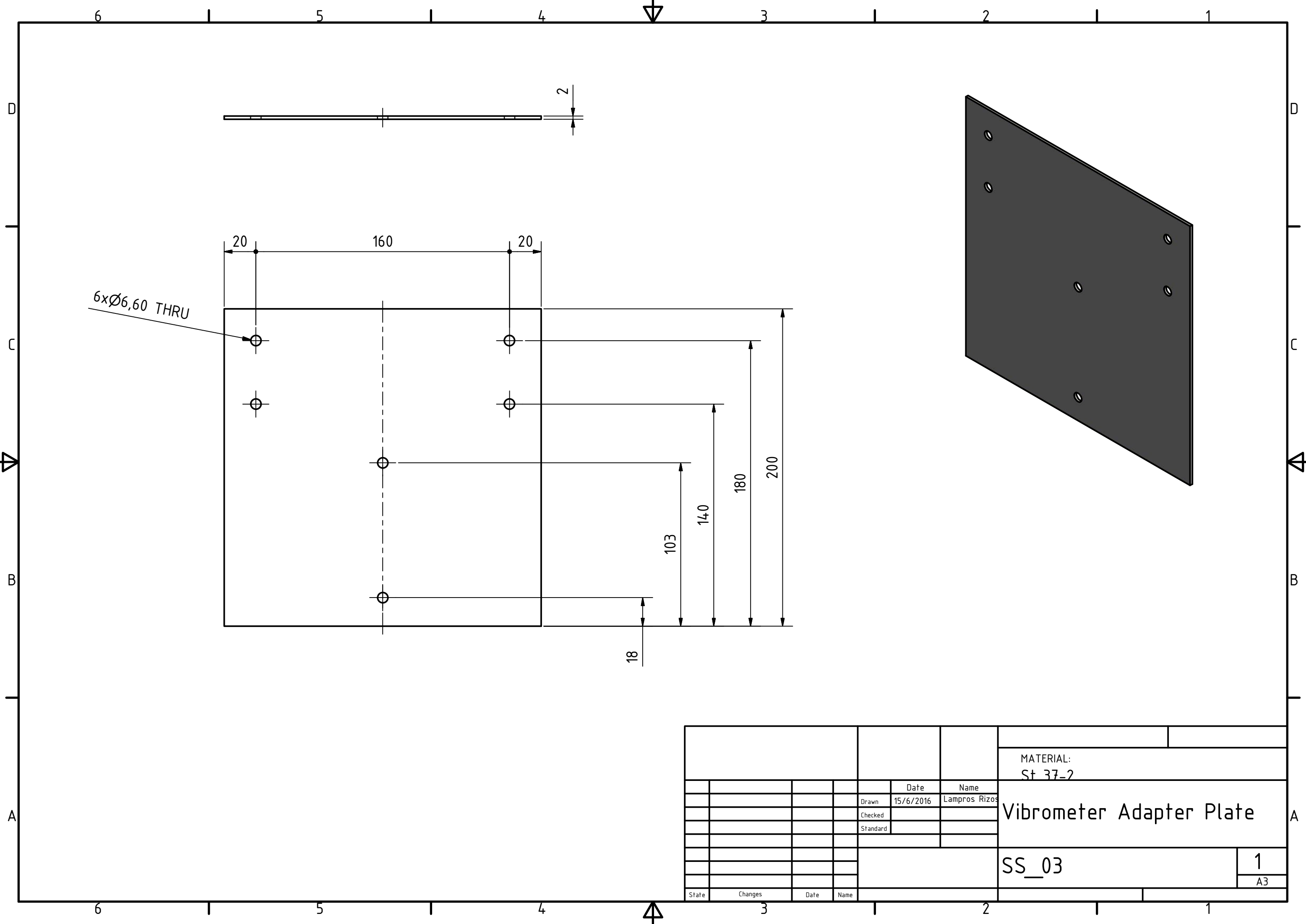


PARTS LIST		
ITEM	QTY	TITLE
1	1	Alignment Plate
2	1	Linear Motor
3	1	Bearing Housing
4	1	Extension Rod
5	2	Bearing
6	1	Laser Triangulation Sensor
7	1	Force Transducer
8	1	Thread Adapter
9	2	Profile8_40x80x1000

								Alignment Assembly	
				Drawn	1/7/2016	Lampros Rizos			
				Checked					
				Standard					
						Alignment Assembly		1	
								A3	
State	Changes	Date	Name						



					Date	Name	Wooden base			
				Drawn	20/5/2016	Lampros Rizos				
				Checked						
				Standard						
							FSI_07			
							1			
							A3			
State	Changes	Date	Name							



								MATERIAL:	
								St 37-2	
					Date	Name		Vibrometer Adapter Plate	
				Drawn	15/6/2016	Lampros Rizos			
				Checked					
				Standard					
								</	